

Copyright
by
Badr Elmaanaoui
2010

**The Dissertation Committee for Badr Elmaanaoui Certifies that this is the approved
version of the following dissertation:**

**Swept Source Polarization Sensitive Optical Coherence Tomography
for Retinal Imaging at 1 Micron**

Committee:

Thomas E. Milner, Supervisor

Henry G. Rylander III, Co-Supervisor

Michael F. Becker

Andrew K. Dunn

D. M. Snodderly

**Swept Source Polarization Sensitive Optical Coherence Tomography
for Retinal Imaging at 1 Micron**

by

Badr Elmaanaoui, B.E., M.E.

Dissertation

Presented to the Faculty of the Graduate School of

The University of Texas at Austin

in Partial Fulfillment

of the Requirements

for the Degree of

Doctor of Philosophy

The University of Texas at Austin

May 2010

Dedication

To my beloved Mother, Brother, and late Father who believed in me

and

To my precious wife and kids who kept up with me.

Acknowledgements

I am greatly indebted to the unrivaled team of advisors Drs. Thomas E. Milner and H. Grady Rylander III. Under their tutelage I was able to hone my technical skills and earn philosophy

A special thanks to Vicki Stratton and Melanie Gulick who made navigating the bureaucracy a breeze. Without their assistance my graduate career would not have been as productive.

Thanks to my friends, colleagues, and predecessors at the biomedical laser lab. Especially Jordan Dwelle, Austin McElroy, Bingqin Wang, Shuang Liu, Jinze Qiu, Biwei Yin, Nate Kemp, and Jesung Park for their assistance in technical and recreational fields.

Finally, I gratefully acknowledge financial support from the National Eye Institute (R01 EY016462-01A1), The University of Texas at Austin, and the taxpayer for financial support of the research presented in this dissertation

Swept Source Polarization Sensitive Optical Coherent Tomography for Retinal Imaging at 1 Micron

Publication No. _____

Badr Elmaanaoui, Ph.D.

The University of Texas at Austin, 2010

Co-supervisor: Thomas E. Milner

Co-supervisor: Henry G. Rylander III

Glaucoma is the second leading cause of blindness in the world. The disease is characterized by irreversible damage to retinal ganglion cells. Once glaucoma is detected, further vision loss can be prevented by pharmacological or surgical treatment. However, current diagnostic methods lack the necessary sensitivity and up to 40% of vision may be irreversibly lost before detection occurs.

A Swept Source Polarization-Sensitive Optical Coherence Tomography (SS-PSOCT) instrument for high sensitivity cross-sectional imaging of optical anisotropy in turbid media has been designed, constructed, and verified. A multiple-state nonlinear fitting algorithm was used to measure birefringence of the retinal nerve fiber layer with less than $\pm 1\%$ average uncertainty.

To perform eye imaging efficiently a slit-lamp based interface for the SS-PSOCT instrument with a Line Scanning Laser Ophthalmoscope (LSLO) was used. This interface allowed for repeatable, stable, and registered measurements of the retina. A

fixation target was used to stabilize the volunteer's eye and image desired areas of the retina. The LSLO allowed for an optimization of the location of OCT scans on the retina and provided a fundus blood vessel signature for registration between different imaging sessions.

The SS-PSOCT system was used to measure depth-resolved thickness, birefringence, phase retardation and optic axis orientation of the retinal nerve fiber layer in normal volunteers. The peripapillary area around the optic nerve head (ONH) is most sensitive to glaucoma changes and hence data was acquired as concentric ring scans about the ONH with increasing diameters from 2mm to 5mm. Imaging of normal patients showed that higher values of phase retardation occurred superior and inferior to the optic nerve head especially next to blood vessels and thicker parts of the retinal nerve fiber layer.

Table of Contents

List of Figures	xii
List of Tables	xviii
List of Symbols.....	xix
List of Symbols.....	xix
Chapter 1: Introduction and Background.....	1
1.1 Organization of the Dissertation	1
1.2 Optical Coherence Tomography	2
1.2.1 Time Domain OCT	6
1.2.2 Fourier Domain OCT.....	8
1.2.2.1 Spectral Domain OCT.....	9
1.2.2.2 Swept Source OCT	10
1.3 Light Polarization.....	12
1.3.1 Polarization of Monochromatic Plane Waves.....	13
1.3.2 Mathematical Representations of Light	15
1.3.2.1 Stokes Vector	15
1.3.2.2 Jones Formalism	17
1.3.2.3 Complex Polarization Ratio	18
1.3.3 Polarization Properties of Materials.....	19
1.3.3.1 Intrinsic Birefringence	19
1.3.3.2 Form Birefringence.....	23
1.4 Physiology of the Retina and Glaucoma.....	24
1.4.1 Anatomy of the Eye	24
1.4.2 Pathophysiology of Glaucoma.....	26
1.4.3 Clinical Treatment of Glaucoma.....	28
1.4.3.1 Current Diagnostic Methods.....	28
1.4.3.2 Objective Examination Methods.....	28
1.4.3.3 Treatment Options	30

1.4.3.4	RNFL Birefringence	31
Chapter 2:	Swept Source Polarization Sensitive Optical Coherence Tomography Instrumentation	32
2.1	Background.....	32
2.2	Optical Configuration	35
2.2.1	Source Path	37
2.2.2	Reference Path	39
2.2.3	Clock/Trigger Path.....	41
2.2.4	Sample Path	42
2.2.5	Detection Path.....	42
2.3	Electro Optic Phase Modulator.....	43
2.3.1	Phase Modulator Alignment	43
2.3.2	Phase Modulator Calibration	45
2.3.3	Precise Electro Optic Modulation.....	46
2.3.4	Long-Crystal Phase Modulator	52
2.4	Polarimetric Detection and Data Acquisition	54
2.4.1	Signal Acquisition.....	54
2.4.1.1	Hardware Description	54
2.4.1.2	Software Description	57
2.4.2	External clocking	59
2.4.2.1	Reproduced K-space Clock.....	61
2.4.2.2	Analog K-space Clock	62
2.4.2.3	Different Clock Schemes Performance Evaluation:	64
2.4.3	Operation of the SS-PS-OCT System	67
Chapter 3:	Slit-lamp Based OCT and LSLO Retinal Imaging	70
3.1	Introduction.....	70
3.2	LSLO/OCT Patient Interface	70
3.2.1	Hazard Analysis	73
3.2.2	Eye Fixation.....	75
3.3	Hardware Dispersion Balancing	77

3.3.1 Simulation	78
3.3.2 Design	80
3.3.3 Experimental Verification.....	82
3.4 Axial Resolution and Sensitivity Measurements	83
3.4.1 Axial Resolution	83
3.4.2 SNR and Sensitivity.....	86
Chapter 4: Polarimetric Data Processing	87
4.1 Introduction.....	87
4.2 Theory	88
4.2.1 Poincare Sphere Representation of Noise-Free Data.....	89
4.2.2 Estimation of RNFL Parameters	90
4.2.3 Nonlinear Fitting Uncertainty	91
4.2.4 Polarimetric Signal to Noise Ratio	92
4.3 Results.....	97
4.4 Conclusion	99
Chapter 5: Patient Measurements	100
5.1 Blood Vessel Detection and Image Registration	100
5.2 Clustered Thickness, Birefringence, and Phase retardation maps	104
5.2.1 Clustered Ring Scan and Clustered Maps.....	104
5.2.2 RNFL Boundary Detection	105
5.2.3 Optimized Clustered Scan Parameters.....	110
5.2.4 TSNIT Analysis for Clustered Thickness, Birefringence and Phase	114
5.4 Uncertainty in Measured Birefringence.....	118
5.3 Optical Axis Maps	121
5.3.1 Overview	121
5.3.2 Euler's Rotation Theorem.....	124
5.3.3 Offset Compensation in Optical Axis Maps	125
5.3.4 Optical Axis Map with Overlaid Blood Vessels.....	127
5.4 Conclusion, and Outlook	128

Appendices.....	132
Appendix A Polarization Mode Dispersion.....	132
Appendix B: Effect of H and V Balancing on Polarimetric Measurements	140
Appendix C Digitizer Phase Errors	142
Appendix D Relative Intensity Noise.....	143
References.....	145
Vita	150

List of Figures

Figure 1.1:	Schematic of a basic bulk-optics time domain OCT instrumentation. Light backscattered from the sample interferes with light reflected from the reference mirror only when the optical path lengths of sample and reference paths are matched to within the coherence length of source light. NPBS: Non-polarizing beam splitter.....	7
Figure 1.2:	Schematic of a fiber-based spectral domain OCT system. C: collimator, TG: transmission grating, ASL: three element air-spaced lens, LSC: line scan camera. A-scan information is obtained by Fourier transforming the interference spectrum acquired with the spectrometer.	10
Figure 1.3:	Schematic of a basic fiber-based swept source OCT system. C: collimator. The A-scan is obtained by Fourier transforming the detected beat signal of the whole sweep acquired at with the photodetector.....	12
Figure 1.4:	Form-birefringence (Δn) origin in fibrous structures. Electric field perpendicular component (E_{\perp}) produces a surface charge density with an induced field (E_0). This changes dielectric susceptibility and gives higher refractive index (n_s) relative to the one experienced by (E_{\parallel}) [17].....	24
Figure 1.5:	Lateral section of adult human eye. Light passes through the cornea and is focused by the lens onto the retina. RGC axons converge into the optic nerve...	25
Figure 1.6:	Diagram of aqueous humor flow pathway. The ciliary processes excrete aqueous humor. The aqueous humor flows between the iris and lens into the anterior chamber, and the majority of the fluid outflows through the trabecular outflow pathway marked by arrows.....	26
Figure 2.1:	SS-PSOCT system schematic with fiber length dimension in brown. PC: polarization controller, P: polarizer, AM: broadband amplitude modulator, C: collimator, CCM: corner cube mirror, PBS: polarizing beam splitter. S: solenoid, VDL: variable delay line, DC: dispersion compensation glass rod, M: silver coated mirror	36
Figure 2.2:	A healthy individual's retina with a bright line artifact corrupting the image and greatly limiting image field of view	47
Figure 2.3:	Matlab® simulation of the etalon effect caused by the angular misalignment between the two crystals. Ghost lines can be seen at 1.7 mm and at 3.4 mm single pass in air. Intensity of the peaks is in arbitrary units in logarithmic scale	48
Figure 2.4:	Modified modulator tilt mount for precise crystal alignment. Independent cantilevers allow relative rotation of crystals. The original mount (in gold) was divided at the middle and attached to the cantilever mount, maintaining gold electrodes epoxied to the original mount.....	49

Figure 2.5:	Exploded view of the modified polarization modulator showing the crystals on the modified mount, modulator box and SMA connector.	49
Figure 2.6:	FFT of interference signal from modulator before modulator modification. A significant ghost line appears at about 8.5 MHz. The ghost line is due to the angular misalignment between the two crystals.....	50
Figure 2.7:	FFT of interference signal from modulator after fine angular adjustment of the two crystals. Amplitude of the 8.5MHz line appears significantly reduced..	51
Figure 2.8:	A polarization diverse intensity image of a circular retinal scan about the ONH of a healthy volunteer’s retina.....	51
Figure 2.9:	Long-Crystal modulator tilt mount with cantilever for precise crystal angular alignment. Two screws provide a push pull mechanism for crystals relative rotation. One screw is threaded to the cantilever mount; the second screw is threaded to the base of the mount.	53
Figure 2.10:	Laser sweep, acquisition trigger timing diagram, EOM drive waveform and slow and fast galvanometer signals.....	56
Figure 2.11:	Electronic instrumentation diagram for acquiring SS-PSOCT interference fringe intensities and LSLO images.....	57
Figure 2.12:	Plot of time variation in clock frequency due to non-linear laser output in k-space. Non-linearity gives rise to degradation in image quality when using a linear acquisition clock.	60
Figure 2.13:	Block diagram of the analog quadrupled k-space clock [55].	64
Figure 2.14:	A ring scan image of a healthy volunteer acquired about the optic nerve head with a 50 MHz time uniform clock.	65
Figure 2.15:	A ring scan image of the same healthy volunteer acquired about the optic nerve head with software quadrupled reproduced k-space clock.	66
Figure 2.16:	A ring scan image of the same healthy volunteer acquired about the optic nerve head with analog quadrupled k-space clock	66
Figure 2.17:	Three laser sweeps corresponding to the three polarization states for both arms. The white curve is for the horizontal channel, the red curve is for the vertical channel and the green is the ratio of V over H. (a) Good detection arm (arm 1). (b) Bad detection arm (arm 2). As can be seen the V over H ratio for the good arm is almost one for the whole spectrum for all three states, whereas for the bad arm state 0 is very far from a ratio of one and varies substantially across the spectrum.	69
Figure 3.1:	ZEMAX model of the optical patient interface module. Model shows propagation of LSLO light from input to the retina and back to the CCD line camera	72
Figure 3.2:	(a) The LSLO and the SS-PSOCT system on a cart with the patient interface module placed on a slit lamp. (b): Optics and electronics tray.....	73
Figure 3.3:	Screenshot of the acquisition software showing the monitor voltage....	75
Figure 3.4:	Polynomial fit to dispersion imbalance between reference and sample arms over the source spectrum.....	78

Figure 3.5:	Phase delay vs. optical frequency for three model eyes. Addition of water in the cuvette did not significantly alter the dispersion profile which is consistent with 1060nm being a water dispersion minimum.....	80
Figure 3.6:	Dispersion profiles of Zemax simulated glass rod (Blue) and model eye (Green).	81
Figure 3.7:	OCT image of infrared sensor card. (a) Without dispersion balancing. (b)With dispersion balancing.....	82
Figure 3.8:	Optical spectrum of swept laser source. Blue curve: optical power (mW) as a function of time. Yellow trace: trigger voltage (V). Magenta curve: wavelength versus time.....	83
Figure 3.9:	Optical power spectrum profile of the swept laser source as a function of optical frequency.....	84
Figure 3.10:	(a) Swept laser source PSF. (b) A zoomed in view of the PSF near the center. Amplitude is in arbitrary units	85
Figure 4.1:	Trajectories from the specimen surface to depth z of noise-free propagation of backscattered light in anisotropic media represented on the Poincare Sphere. (a). Arc due to double pass retardation, $2\delta(z)$, about $\hat{\beta}$ only. (b). Same circular arc converging toward $\hat{\beta}$ in the presence of double pass diattenuation, $2\varepsilon(z)$, results in a three-dimensional spiral [62].....	90
Figure 4.2:	Arcs and fits recorded from the left eye of a healthy patient. Top row is from a thick cluster in the inferior quadrant. Bottom row is from a thin cluster in the nasal quadrant. (a): 100 A-scans per cluster, PSNR = 32.58 dB. (b) 36 A-scans per cluster, PSNR = 26.90 dB. (c) 16 A-scans per cluster, PSNR = 11.71 dB. (d) 100 A-scans per cluster, PSNR = 21.99 dB. (e) 36 A-scans per cluster, PSNR = 18.35 dB. (f) 16 A-scans per cluster, PSNR = 13.82 dB. For thick clusters 36 A-scans per clusters are sufficient to accurately estimate birefringence and eigen-axis $\hat{\beta}$, whereas for thin clusters 36 A-scans per cluster introduce an error in birefringence and eigen-axis $\hat{\beta}$ estimation and 81 A-scans per cluster are needed for the accurate estimation of birefringence and eigen-axis $\hat{\beta}$	96
Figure 4.3:	Ensemble averaging of N_A uncorrelated fields increases PSNR by a factor of $N_A^{1/2}$. Data was acquired from the RNFL of a healthy individual's left eye.	97
Figure 4.4:	Data from the weakly turbid birefringent film showing (a) polarimetric speckle corrupted arcs, $S_m(z)$ and their noise-free fits, $P_m(z)$ such that $m = 0$ (red), 1(orange), and 2(blue). All three states on the Poincare sphere fit to the same eigen-axis, $\hat{\beta}$. Evolution of the polarimetric speckle noise corrupted normalized Stokes parameters (Q_n , U_n , and V_n) for the three incident polarization states (b): $S_0 = -120^\circ$, (c): $S_1 = 0^\circ$, and (d): $S_2 = +120^\circ$ (solid lines), as well as the noise-free model fits (dotted lines).....	99

Figure 5.1:	Steps to reconstruct blood vessel map from OCT raster scans. (a) B-scan images from different locations in the retina. Green dotted line represents anterior RNFL boundary; blue line represents the offset from which intensity is averaged; fluorescent green line represents the boundary at which averaging is stopped. Average signal intensity is displayed below each B-scan. (b) Averaged signals from each B-scan are plotted as a line representing the location of the B-scan acquisition until the whole fundus-like image is reconstructed. (c) Map of blood vessel edges reconstructed from the fundus-like image in (b).....	102
Figure 5.2:	Fundus-like images reconstructed from (a) raster scan and (b) continuous ring scan (c) LSLO image. All maps are from the same imaging session.	103
Figure 5.3:	Blood vessel edges obtained from (a) raster scan, (b) continuous ring scan, and (c) LSLO images.	103
Figure 5.4:	Scanning pattern of clustered ring scan overlaid on the LSLO fundus image. Scanning pattern of each cluster is shown in the inset in the upper-left corner. Each circle in the inset represents A-scan. The area covered by the cluster is $66\mu\text{m} \times 42\mu\text{m}$ for inner ring and $66\mu\text{m} \times 130\mu\text{m}$ for outer ring.	105
Figure 5.5:	Flow chart for calculating clustered birefringence maps using a three-step approach.	108
Figure 5.6:	Comparison of clustered birefringence maps using different RNFL boundary detection strategies. Left: automatic boundary detection. Middle: auto/manual boundary detection. Right: manual boundary detection.	109
Figure 5.7:	Comparison of averaged uncertainty during Stokes fitting using automatic boundary, automatic/manual boundary, and manual boundary detections. Spread bars represent the spread in uncertainty value from all clusters in the map	110
Figure 5.8:	Influence of B-scan number. (a) thickness map (10 B-scans); (b) birefringence map (10 B-scans); (c) phase retardation map (10 B-scans); (d) thickness map (15 B-scans); (e) birefringence map (15 B-scans); (f) phase retardation map (15 B-scans). Cluster number = 36 and Cluster size = 100 for all maps. All maps are acquired about the ONH with 2 mm inner ring diameter and 5 mm outer ring diameter.....	111
Figure 5.9:	Influence of Cluster number. (a) thickness map (36 clusters per B-scan); (b) birefringence map (36 clusters per B-scan); (c) phase retardation map (36 clusters per B-scan); (d) thickness map (72 clusters per B-scan); (e) birefringence map (72 clusters per B-scan); (f) phase retardation map (72 clusters per B-scan). B-scan number = 10 and Cluster size = 100 for all maps. All maps are acquired about the ONH with 2 mm inner ring diameter and 5 mm outer ring diameter.	112
Figure 5.10:	Influence of Cluster size. (a) thickness map (100 A-scans in each cluster); (b) birefringence map (100 A-scans in each cluster); (c) phase retardation map (100 A-scans in each cluster); (d) thickness map (50 A-scans in each cluster); (e) birefringence map (50 A-scans in each cluster); (f) phase retardation map (50 A-scans in each cluster). B-scan number = 20 and Cluster number = 80 for all maps.	

All maps are acquired about the ONH with 2 mm inner ring diameter and 5 mm outer ring diameter.	113
Figure 5.11: RNFL thickness (μm) in different retinal regions of a healthy patient's left eye (OS). Curve shows the relationship between averaged thickness and angular position starting at the temporal region and rotating in a counter-clockwise fashion. Spread bars represent the thickness spread across the ten rings at the same angle.	115
Figure 5.12: Clustered thickness maps with superimposed blood vessels detected from raster scans. Left: right eye (OD) (colorbar: $0\mu\text{m} - 180\mu\text{m}$). Right: left eye (OS) (colorbar: $0\mu\text{m} - 180\mu\text{m}$). In superior and inferior regions, RNFL is thicker and blood vessels are denser.	116
Figure 5.13: Birefringence ($^{\circ}/\mu\text{m}$) in different retinal regions. Curve shows the relationship between single pass phase retardation per unit depth and angular position. Spread bars represent the birefringence spread across the ten rings at the same angle.	117
Figure 5.14: Phase retardation ($^{\circ}$) in different retinal regions. Curve shows the relationship between single pass phase retardation and angular position. Spread bars represent phase retardation spread across the ten rings at the same angle.	118
Figure 5.15: Uncertainty maps with blood vessels for both eyes. Left: OD (right eye). Right: OS (left eye).	119
Figure 5.16: Poincare sphere model of (a) $44\mu\text{m}$ thin RNFL cluster ($\pm 1.57\%$ birefringence uncertainty) and (b) $138\mu\text{m}$ thick RNFL cluster ($\pm 0.24\%$ birefringence uncertainty).	120
Figure 5.17: Comparison of absolute uncertainty in different regions in retina. Lower values are for average uncertainty per quadrants in degrees per 100 microns. Upper values are average percentage error in birefringence measurement. Spread bars represent uncertainty spread in different clusters per quadrant.	121
Figure 5.18: Finding optical axis position in a Poincare sphere. (a) The optical axes of 36 clusters per B-scan plotted as points on the Poincare sphere surface. (b) Plane fit to the 36 clusters by a multiple linear regression model. (c) The fitted plane rotated to the QU plane using Euler's rotation theorem. (d) For each point, the azimuthal angle divided by two so that the optical axes forms one ring in the QU plane. The position of the optical axis in the retina can be calculated from the azimuthal angle of points on the QU plane.	123
Figure 5.19: Optical axis maps. (a) Before offset rotation. (b) After offset rotation of each ring. (c) After offset rotation of the whole map.	126
Figure 5.20: Optical axis map with blood vessels shows that the directions of optical axes are pointing to the center of the optic cup, which is indicated by the blue regions. Left: OD (right eye); Right: OS (left eye).	128
Figure 5.21: Noisy RNFL $S(z)$ arcs and their fits $P(z)$ for (a) 3 input polarization states, (b) 2 input polarization states. Results demonstrate that for high PSNR two states are sufficient even when the two chosen states provide less than optimal separation between $P(0)$ and eigen axis $\hat{\beta}$	130

Figure 5.22: Proposed detection arm setup. P: sheet polarizer, BS: 50/50 bulk beam splitter, C: collimator, PC: polarization controller, PBS: polarization beam splitter. ..	131
Figure A.1: PSF showing no delay between horizontal and vertical polarization detection channels. Amplitude is in dB logarithmic scale.	133
Figure A.2: Nonlinearity curve using 4m HI1060 FLEX with the Polarite polarization controller.....	136
Figure A.3: Nonlinearity curve using 4m HI1060 FLEX with the large paddles type polarization controller.....	136
Figure A.4: Nonlinearity curve using 4m HI1060 FLEX with the small paddles type polarization controller.....	137
Figure A.5: Nonlinearity curve using 4m HI1060 FLEX with the large paddles type polarization controller.....	137
Figure A.6: Nonlinearity curve using 25m HI1060 FLEX with the large paddles type polarization controller.....	138
Figure A.7: Nonlinearity curve using 4m HI1060 FLEX with the large paddles type polarization controller.....	138
Figure A.8: Nonlinearity curve using 4m HI1060 with the large paddles type polarization controller.....	139
Figure B.1: Arcs and their fits for the same birefringent film and with all parameters kept the same except for the V/H ratio. (a) V/H ratio optimized and fits appear accurate. (b) V/H uniform but not unity and the fits look somewhat inaccurate. (c) V/H not uniform and not unity and the fits look inaccurate.	141
Figure D.1: Average background in the laser before the upgrade and after the upgrade. The laser upgrade has an average 6dB more noise than the laser before the upgrade at the same reference power.....	143
Figure D.2: Arcs and fits recorded from the left eye (OS) of a healthy patient. (a) Thick cluster from inferior quadrant. 100 A-scans per cluster, PSNR = 22.12 dB. (b) Thin cluster from nasal quadrant. 100 A-scans per cluster, PSNR = 12.76 dB. Using the laser prior to the upgrade on the same volunteer and at about the same location in the eye resulted in a 10 dB higher PSNR.....	144

List of Tables

Table 1.1:	ROC curve areas and sensitivities at fixed specificities for discriminating between glaucomatous and healthy eyes [18].....	30
Table 2.1:	SNR and PSF comparison at various depths between analog quadrupled and software quadrupled clocks.....	67
Table 3.1:	Total phase variation across the spectrum calculated from the three model eyes. Cuvettes model eyes with and without water in the OPL show that there is no significantly added dispersion due to water.	79
Table A.1:	Non-linearity RMS value for all tested setups.....	135

List of Symbols

Fiber axis orientation	θ
Depth (axial) dimension	z
Lateral dimensions	x, y
Horizontal and vertical electric field amplitudes	$E_h(z), E_v(z)$
Accumulated phase retardation	δ
Impedance of the medium	η
Magnetic permeability of dielectric medium	μ
Electric permittivity of dielectric medium	ϵ
Stokes vector (Stokes parameters combined into a vector)	$\vec{S}(z)$
Power in the wave	I
Complex polarization ratio	χ
Birefringence or form-birefringence	Δn
Electric flux density along the i^{th} coordinate direction	D
Horizontal and vertical interference fringe intensities	$\Gamma_h(z), \Gamma_v(z)$
Average polychromatic phase error	$\Delta\Phi$
Signal to noise ratio	SNR
Depth-resolved polarization data	$S(z)$
Noise free model polarization arc	$P(z)$
Eigenpolarization axis (eigen-axis) Stokes vector	$\hat{\beta}$
Standard deviation of polarimetric speckle noise	σ_{speckle}
Arc length of noise free model polarization arc	l_{arc}
Number of uncorrelated speckle fields	N_A
Separation angle	γ
Single-state residual function	R_o
Multi-state residual function	R_M
Number of incident polarization states	M

Chapter 1: Introduction and Background

1.1 ORGANIZATION OF THE DISSERTATION

Chapter 1 gives an introduction to optical coherence tomography (OCT), the basis of the technology needed to understand and appreciate the instrumentation described in this dissertation. A brief introduction to the polarization properties of light is presented to establish the theory behind the technique for recording measurements described in later chapters. Physiology of the retina is discussed since the retinal nerve fiber layer (RNFL) is the biological sample that is the object of study in this dissertation. Polarimetric properties of the RNFL are also discussed.

Chapter 2 provides an introduction to swept source polarization sensitive optical coherence tomography (SS-PS-OCT). A schematic of the SS-PS-OCT system is presented alongside a description of all major optical and electrical system components. Detailed software and hardware description of detection and data acquisition is presented.

In Chapter 3, the optical interface between the eye and the OCT/LSLO system is presented. The optical interface offers instrumentation to simultaneously record high quality wide field lateral scanning laser ophthalmoscope (LSLO) and OCT images with eye fixation to reduce motion artifact. The optical interface introduces dispersive elements to the sample arm and requires dispersion compensation. A method for hardware dispersion compensation was devised, simulated, and implemented. The method was successful in balancing dispersion in the system and transform-limited longitudinal spatial resolution was obtained. Hazard analysis and system sensitivity are also presented.

Chapter 4 deals with polarimetric modeling of the RNFL, display of RNFL polarimetric data using the Poincare sphere representation, and estimation of polarimetric properties using Stokes parameters and a nonlinear fitting algorithm. Uncertainty in measured birefringence is described and polarimetric signal-to-noise ratio improvement as a function of number of A-scans per cluster is discussed. Measurement results of a calibration birefringent film are presented and compared to previously published results.

Chapter 5 describes a comprehensive study to record spatially-resolved maps of healthy human RNFL thickness, birefringence, phase retardation, and optic axis orientation in normal subjects. Phase retardation uncertainty maps are also computed. To provide an approach for registration of recorded OCT images, the blood vessel signature of the retina was extracted from one of three methods; OCT raster scans, OCT continuous ring scans, and LSLO images. Blood vessel traces were overlaid on the spatially resolved maps of RNFL thickness, birefringence and phase retardation and their location investigated. Different scan patterns and boundary detection schemes for birefringence measurements are described. A summary of presented work with an outlook of future system upgrades is discussed.

Appendices at the end of the dissertation cover the major engineering challenges faced and overcome by the SS-PS-OCT system.

1.2 OPTICAL COHERENCE TOMOGRAPHY

Since its first demonstration in 1991 [1], optical coherence tomography (OCT) has evolved into a non-invasive high resolution cross-sectional structural imaging modality that acquires depth-resolved two- and three-dimensional images of biological tissue with few micrometers axial resolution [2]. Although histology and biopsy remain

the gold standard in many disease diagnostics, they do not provide real-time feedback for the clinician, are highly invasive, and can suffer from sampling errors. The last decades saw a revolution in noninvasive or minimally invasive imaging modalities such as X-ray computed tomography (CT), positron emission tomography (PET), magnetic resonance imaging (MRI), functional MRI (fMRI), and ultrasound (US). Each of these imaging modalities provides three dimensional visualization of biological tissue with significant penetration into the tissue and has contributed significantly to the understanding of disease pathogenesis; however, each of these modalities is limited to tens of microns to several millimeters in axial resolution. Other non-invasive optical based microscopy modalities such as confocal, fluorescence, and multi-photon imaging can offer sub-micrometer axial resolution but exhibit limited penetration depth of less than a few hundred micrometers in biological tissue. Most of the above mentioned modalities are unsuitable for retinal imaging.

OCT image contrast originates from optical scattering, and in highly scattering biological tissues OCT can image 1 to 3 mm deep. Using light sources in the near infrared makes OCT ideal for imaging skin, epithelial/endothelial linings of internal luminal organs, gastrointestinal tract, oral cavity, and interior and posterior layers of the eye. OCT has been shown to be a powerful tool for in-vivo real-time medical imaging, diagnosis, measurement, repeated monitoring of treatment, and precision guidance of surgical interventions. In the coming years, OCT is expected to continue to grow in many medical fields, particularly ophthalmology and cardiology. Functional extensions of OCT including phase, Doppler, speckle, and polarization promise to provide better image contrast as well as functional imaging of tissue microstructures.

Signal-to-noise ratio (SNR), axial and transverse resolution, as well as penetration depth are some factors that contribute to OCT image quality. Transverse resolution in

OCT, like in conventional microscopy, is dependent on the imaging optics. For Gaussian beams, transverse resolution, Δx , is equal to $2\omega_0$, where $2\omega_0$ is the $1/e^2$ beam spot size and is given by the equation:

$$\Delta x = 2\omega_0 = \frac{4\lambda_0}{\pi} \cdot \frac{f}{d_{beam}} = \frac{4\lambda_0}{\pi} \cdot \frac{1}{NA} \quad (1.1)$$

where f is the focusing system focal length; λ_0 is the center wavelength of the light source; d_{beam} is the spot size of the beam at the focusing element; NA is numerical aperture. By increasing numerical aperture of the objective lens, one can achieve better transverse resolution.

In retinal imaging, cornea and lens dictate the system focal length, and hence increasing incident beam diameter should theoretically increase numerical aperture and therefore decrease transverse resolution. Though beam diameter at the cornea can be increased to several millimeters by dilating the pupil, aberrations (primarily spherical) also increase with increasing beam diameter. For many human eyes, a beam size of 1.5-2 mm at the pupil yields the smallest spot size (20 μ m - 30 μ m) at the retina when adaptive optics is not used [3, 4]. Adaptive optics systems tend to be bulky, complex and have reduced acquisition speeds. In general, increasing NA decreases transverse resolution and also reduces depth of field (confocal parameter) which is equal to $2z_R$, or twice the Rayleigh range:

$$2z_R = \pi \cdot \frac{\Delta x^2}{\lambda} \quad (1.2)$$

Unlike standard microscopy, axial resolution in OCT is completely decoupled from transverse resolution and only depends on light source spectral properties and system transfer function. For a source with a Gaussian spectrum, the full-width-at-half-maximum (FWHM) of the autocorrelation function, or axial resolution, Δz , is given by:

$$\Delta z = \frac{2 \ln 2}{\pi} \cdot \frac{\lambda^2}{\Delta \lambda} \quad (1.3)$$

where $\Delta \lambda$ is the FWHM of the source power spectrum, also referred to as the source bandwidth [5]. Traditionally, OCT has been used at three central wavelengths, namely 830, 1060, and 1310 nm. To achieve an axial resolution of 2 μm at these wavelengths, one requires a source bandwidth of about 150, 250, and 380 nm respectively. However, no ophthalmologic imaging system has been demonstrated at this resolution to date due wavelength dependent absorption of water, axial length of the human eye, and power limitations for ophthalmologic imaging that affect the source spectrum available for imaging [6].

Since longer wavelength sources in the near infrared are more suitable for imaging in highly scattering tissue, 1310 nm sources have been most widely used in OCT. Many biological tissues (skin, dentin, cartilage, arteries, etc) can handle several tens of milliwatts of continuous power without sustaining damage. 1310 nm sources can be used to image the anterior parts of the eye including the cornea and trabecular meshwork. For the retina, however, imaging with a 1310nm source is not possible because less than 1% of the light is transmitted through 46 mm of water corresponding to double passage of light through the average human eye. Since water absorption in retinal imaging is a concern, sources centered at about 830nm, where water absorption is minimal, were developed and became most common for OCT retinal imaging. Recently, sources centered at 1060nm have been developed. Although water absorption is higher at 1060 nm and about half the light is attenuated in double pass transmission to and from the retina, the maximum permissible exposure (MPE) at 1060 nm is much higher than MPE at 830 nm [7]. Use of a 1060 nm wavelength source, where scattering is lower, allows for deeper light penetration well into the choroid and even the sclera [8, 9]. Penetration

of 830nm light is limited by absorption and scattering of the retinal pigment epithelium (RPE) and low MPE. 1060 nm happens to be at a water dispersion minimum and hence provides an additional advantage for retinal imaging since dispersion is always a concern in interferometric imaging modalities (e.g., OCT) [10].

OCT systems can be classified into two categories referred to as time domain (TD-) and frequency domain (FD-) OCT. TD-OCT represents the first generation of OCT systems whereas FD-OCT represents the more recent generation of OCT systems. The latter is subdivided into swept-source (SS-) OCT and spectral-domain (SD-) OCT. A brief overview of various OCT systems, techniques and advantages is presented.

1.2.1 Time Domain OCT

Time-domain OCT instrumentation consists of a two-beam interferometer (usually a Michelson configuration) with source, reference, sample, and detection paths. A continuous-wave broadband and low temporal coherence light source comprises the main component of the source arm. A non-polarizing beam splitter splits source light into reference and sample paths. A primary component of the reference arm is usually a mirror, a corner-cube or combination mirror mounted such that the reference arm optical path length can be rapidly modulated. The sample arm includes an optical interface that allows light delivery to the sample and beam scanning. Light returning from the sample and reference paths recombines and interferes in the non-polarizing beam splitter and is redirected to the detection path (Figure 1.1). Constructive interference only occurs when the optical path lengths of light in sample and reference arms match within the coherence length of source light. An optical point photo-detector in the detection arm registers the interfering optical signal. The signal is amplified and digitized at the computer for

analysis. By varying the optical path length of light in the reference path, a depth scan (A-line) is acquired. By scanning the beam laterally in the sample path along one or two axes, one can respectively record two-dimensional (B-scan) or three-dimensional (volume) tomograms of the sample.

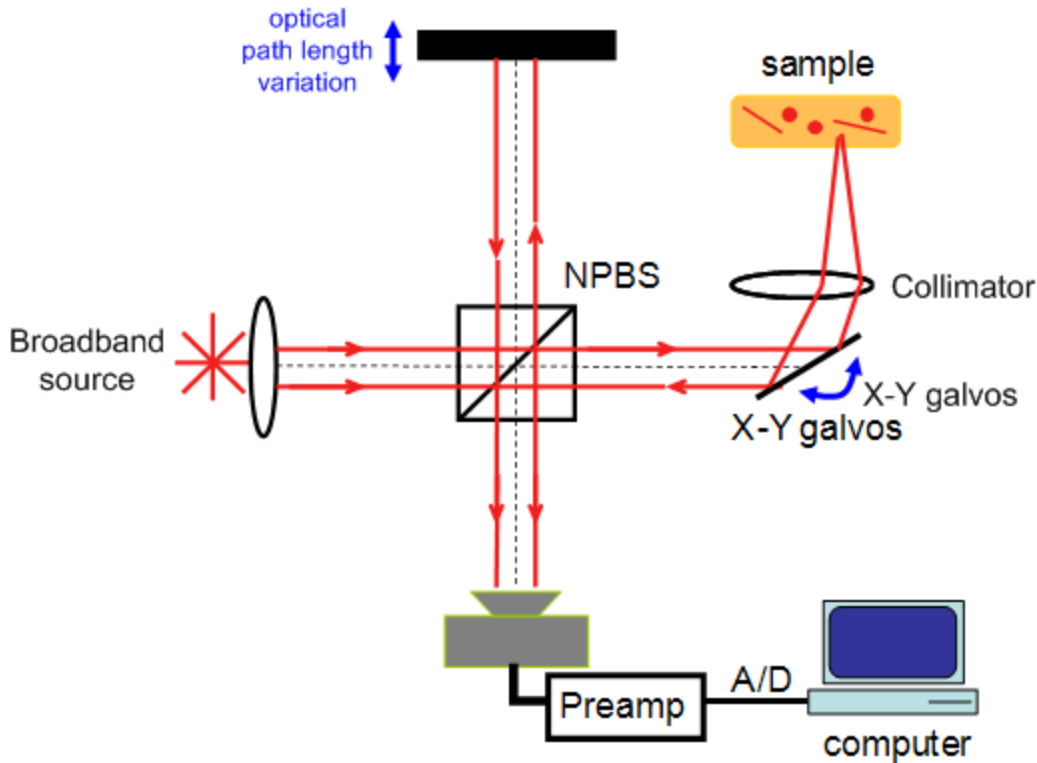


Figure 1.1: Schematic of a basic bulk-optics time domain OCT instrumentation. Light backscattered from the sample interferes with light reflected from the reference mirror only when the optical path lengths of sample and reference paths are matched to within the coherence length of source light. NPBS: Non-polarizing beam splitter.

Up to five-ten years ago, most OCT systems utilized a time-domain detection scheme (TD-OCT) requiring a moving component in the reference path to coherently gate back-reflected light from different depths in the sample. Optical pathlength in the reference arm is mechanically scanned, which can result in a complex optical and

mechanical design since the reference arm would need to be scanned for a few millimeters at several kilohertz rates to achieve real time imaging. Another limitation of TD-OCT is the fact that the signal is generated serially by scanning the reference arm and acquiring the fringe data at a point photo-detector, which typically reduces efficiency by a factor of about 10^2 to 10^3 , approximately corresponding to the ratio of the scan depth to the axial point spread function.

1.2.2 Fourier Domain OCT

Fercher et al., as early as 1995 [11], demonstrated that it is possible to perform OCT detection in Fourier domain (FD) by measuring the interference spectrum. However, FD-OCT techniques did not gain in popularity until 2003 when it was shown that FD-OCT holds several advantages over TD-OCT in terms of sensitivity and acquisition speed. Using FD-OCT, the entire sample depth-resolved information is encoded in the detected spectral interference signal. A-scan information is recovered using the inverse Fast Fourier transform (IFFT). After the recent advances in laser and line scan camera technologies, high speed and high resolution 2-, 3-D imaging became possible [12, 13]. Two distinct methods that employ spectral measurements have been developed. One technique is spectral domain OCT (SD-OCT), which uses a broadband light source and achieves spectral discrimination with a dispersive spectrometer in the detection arm (Figure 1.2). The other technique is swept source OCT (SS-OCT), which achieves spectral discrimination through time-encoding of optical wavenumber (inverse wavelength) by rapidly tuning a narrowband source over a broad optical bandwidth in the source arm and using a point-detector in the detection arm (Figure 1.3). Both techniques acquire the interferometric fringe signal generated by mixing sample with reference light

at a fixed group delay as a function of optical wavenumber, and both do not require a scanning optical path length delay line in the reference arm. Since the reference arm does not require modulation and remains static, FD-OCT exhibits superior acquisition speeds making real-time display and data acquisition of volumes in seconds possible, whereas time domain techniques required minutes. FD-OCT substantially minimizes motion artifacts and significantly advances imaging possibilities. At the same acquisition speeds, Fourier domain techniques exhibit a sensitivity advantage over TD-OCT of 20-30 dB since all light backscattered from the sample contributes to the detected signal.

1.2.2.1 Spectral Domain OCT

The basic setup of a spectral domain OCT system (also known as spatially encoded Fourier domain OCT) is similar to time domain systems as far as the interferometer and light sources are concerned. Unlike TD-OCT, reference arm reflector in SD-OCT instrumentation is static, and detection arm is comprised of a spectrometer and a high speed line camera (figure 1.2). Signal and reference beams have a relative time delay determined by path length difference between the fixed length reference arm and different path lengths in the sample arm. Different path lengths in the sample arm originate from the scattering centers being at different depths in the sample. Interference of the two beams exhibits a spectral modulation as a function of optical frequency. Periodicity of spectral modulation is inversely related to the echo time delay between reference and sample paths. Different echo delays will produce different frequency modulations. Depth profile (A-line) information is obtained by detecting the whole spectrum using the spectrometer and line camera then computing the Fourier transform.

2-D and 3-D images can be obtained by scanning the sample arm in a manner similar to TD-OCT.

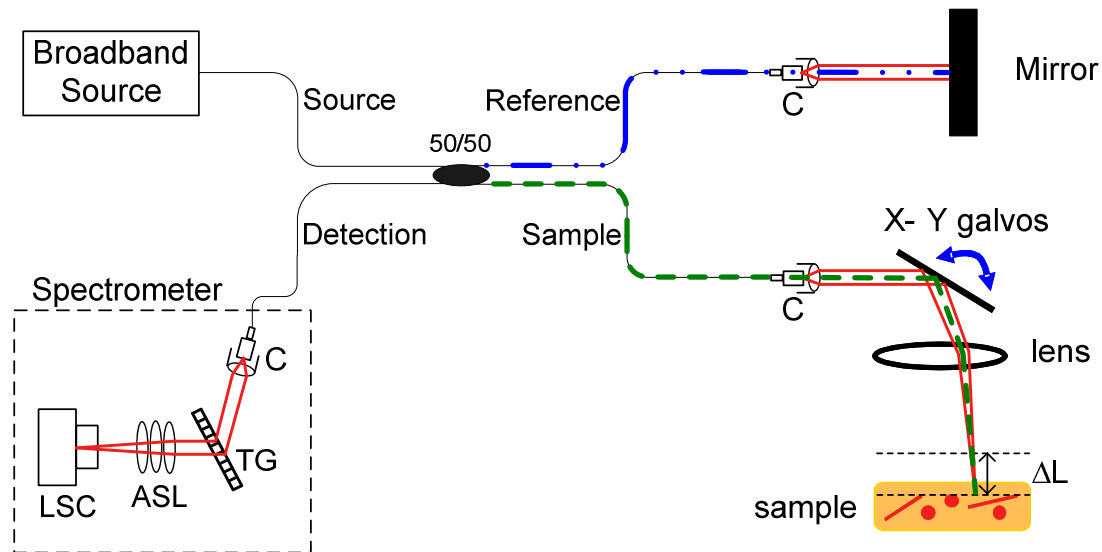


Figure 1.2: Schematic of a fiber-based spectral domain OCT system. C: collimator, TG: transmission grating, ASL: three element air-spaced lens, LSC: line scan camera. A-scan information is obtained by Fourier transforming the interference spectrum acquired with the spectrometer.

1.2.2.2 Swept Source OCT

Swept source OCT (also known as optical frequency domain imaging (OFDI) or time encoded frequency domain OCT) achieves spectral discrimination through time-encoding of wavenumber by rapidly sweeping a narrowband light source over a broad optical bandwidth and computing the Fourier transform of the fringe signal detected using a single photo-receiver (figure 1.3). Backscattered light from different depths at the sample has different time delays relative to light returning from the fixed pathlength reference arm. Since light source frequency is swept in time, light echoes exhibit a fringe

modulation with a frequency proportional to the pathlength offset between sample and reference arms. Interfering light has an intensity modulation at a frequency proportional to the offset between optical pathlength in sample and reference arms. Different echo delays (depths) produce different frequency modulations. Fourier transform of detected interference signal in each laser sweep results in the axial depth profile (A-line). 2-D and 3-D images can be obtained by scanning light laterally in the sample arm in a similar manner to TD and SD-OCT.

Although SS-OCT requires a swept source laser in the source arm compared to a simple broadband light source used in SD-OCT, one can argue that SS-OCT has an advantage over SD-OCT because only a single photodetector is required in the detection arm instead of a spectrometer with a multi-element array. Since SS-OCT does not require a spectrometer, the approach is commonly employed in the 1060 and the 1310nm spectral regimes where silicon line-scan cameras are insensitive.

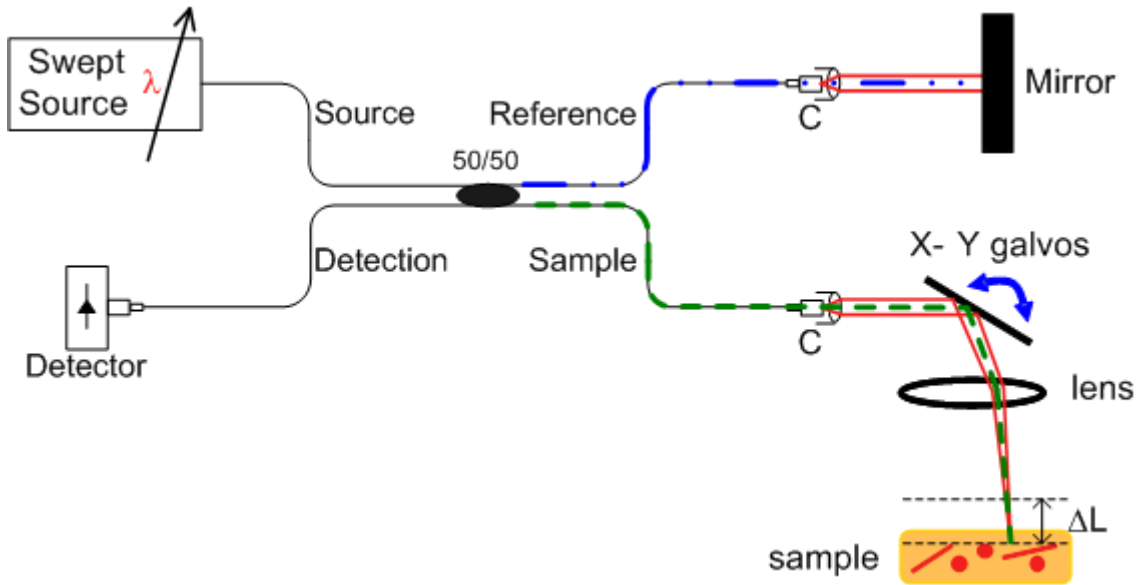


Figure 1.3: Schematic of a basic fiber-based swept source OCT system. C: collimator. The A-scan is obtained by Fourier transforming the detected beat signal of the whole sweep acquired at with the photodetector.

1.3 LIGHT POLARIZATION

Light, being an electromagnetic wave could be described by any of its four basic field vectors. The four field vectors are: the electric-field strength E , the electric-displacement D , the magnetic-field strength H , and the magnetic-flux density B . To define the state of polarization any field could have been chosen, however, historically and for practicality matters, the electric-field strength E has been chosen. The practical choice is based on the fact that when light interacts with matter, the force exerted on the electrons by the electric field is much stronger than that exerted by the magnetic field. Based on Maxwell's field equations and knowledge of the material dispersion relations it is sufficient to determine the polarization of E to deduce the polarization of the other field vectors, D , H , and B [14].

1.3.1 Polarization of Monochromatic Plane Waves

Polarization state of a light wave at a fixed point in space, \mathbf{r} , at time t is given by the electric field vector, $\mathbf{E}(\mathbf{r}, t)$. For the case of a monochromatic wave, time variation of the electric field vector is sinusoidal. Spatial dependence of the time-harmonic optical field must satisfy Maxwell's equations and can be decomposed into three independent linear harmonic vibrations along mutually orthogonal directions x , y , and z with unit vectors \hat{x} , \hat{y} , and \hat{z} respectively, such that:

$$\begin{aligned}\mathbf{E} &= \mathbf{E}_x \hat{x} + \mathbf{E}_y \hat{y} + \mathbf{E}_z \hat{z} \\ \mathbf{E}_i &= \widehat{E}_i \cos(\omega t + \delta_i), \quad i = x, y, z\end{aligned}\tag{1.4}$$

ω represents angular frequency; \widehat{E}_i and δ_i respectively represent amplitude and phase of linear vibrations along the i^{th} coordinate direction.

In this dissertation I will discuss a special case of wave propagation called paraxial optics, where light propagates along directions that lie within a narrow cone centered about the optical axis (z -axis for example). Light can then be treated as a uniform transverse-electric (TE) travelling plane wave with electric field vector lying in the x - y plane.

The electric field vector of equation 1.4 can be simplified to:

$$\mathbf{E}(z, t) = \text{Re} \left\{ \widetilde{E} \exp \left[j 2 \pi f \left(t - \frac{z}{c} \right) \right] \right\}\tag{1.5}$$

$$\widetilde{E} = \widetilde{E}_x \hat{x} + \widetilde{E}_y \hat{y}\tag{1.6}$$

where \widetilde{E} is a complex envelope with complex components \widetilde{E}_x and \widetilde{E}_y such that:

$$\widetilde{E}_x = E_x \exp(j\delta_x) \text{ and } \widetilde{E}_y = E_y \exp(j\delta_y)$$

The electric field is same at constant z because the wave is uniform and since the wave is transverse-electric there is no field component along the direction of propagation (z). Using the phasor (complex) notation, $\mathbf{E}(z, t)$ can be written as:

$$\mathbf{E}(z, t) = \left[E_x \cos\left(\omega t - \frac{2\pi}{\lambda} z + \delta_x\right) \right] \hat{x} + \left[E_y \cos\left(\omega t - \frac{2\pi}{\lambda} z + \delta_y\right) \right] \hat{y} \quad (1.7)$$

E_x and E_y represent amplitudes of the linear harmonic oscillations of electric-field components along x and y directions. δ_x and δ_y represent phases of the electric-field oscillations. X and y components of $\mathbf{E}(z, t)$ can be written as:

$$\begin{aligned} \xi_x &= E_x \cos\left[2\pi f\left(t - \frac{z}{c}\right) + \delta_x\right] \\ \xi_y &= E_y \cos\left[2\pi f\left(t - \frac{z}{c}\right) + \delta_y\right] \end{aligned} \quad (1.8)$$

ξ_x and ξ_y are periodic functions of $t - z/c$ oscillating at frequency f. The equations in eq.1.8 are the parametric equations of an ellipse given by:

$$\frac{\xi_x^2}{E_x^2} + \frac{\xi_y^2}{E_y^2} - 2 \cos \delta \frac{\xi_x \xi_y}{E_x E_y} = \sin^2 \delta \quad (1.9)$$

where $\delta = \delta_y - \delta_x$ is the phase difference. At each position \mathbf{z} , the endpoint of the vector $\mathbf{E}(z, t)$ rotates periodically in the x-y plane and traces out an ellipse. At a fixed time t, the locus of the tip of $\mathbf{E}(z, t)$ vector follows a helical trajectory in space lying on the surface of a cylinder with an elliptical cross section. In general, the electric-field vector propagation is periodic with a period equal to the wavelength of light $\lambda = \frac{c}{n \cdot f}$. The

shape of the ellipse determines polarization state of the wave and is dependent on two parameters, the ratio of the magnitudes E_y/E_x and the phase difference given by $\delta_y - \delta_x$.

The wave intensity is determined from size of the ellipse and η , medium impedance, such that:

$$I = (E_x^2 + E_y^2)/2\eta \quad (1.10)$$

where

$$\eta = \sqrt{\frac{\mu}{\epsilon}}$$

μ is magnetic permeability, and ϵ electric permittivity of the dielectric medium. If one of the components equals zero, for example $E_x = 0$, light is linearly polarized in the y direction. If $\delta = \frac{\pi}{2}$ or $-\frac{\pi}{2}$ and $E_x = E_y = E_0$, then equation (1.9) becomes $\xi_x^2 + \xi_y^2 = E_0^2$, which is the equation of a circle. The wave is said to be right circularly polarized ($\delta = +\frac{\pi}{2}$), or left circularly polarized ($\delta = -\frac{\pi}{2}$) [14, 15].

1.3.2 Mathematical Representations of Light

Since full expression of the wave given in eq.1.7 above may be cumbersome, a concise notation is desired that fully describes the wave especially when considering wave propagation in different materials. We briefly describe some mathematical representations for the polarization of light, namely Stokes vectors, Jones formalism, and the complex polarization ratio. Polarization of light is inherently a statistical phenomenon. Jones formalism and complex polarization ratio representation do not include the statistical properties of light whereas Stokes parameter description does.

1.3.2.1 Stokes Vector

Stokes parameters provide a useful description of the polarization state of electromagnetic waves. Stokes parameters are scalar indicators of radiation polarization states and are subsequently sometimes called headless vectors. Stokes parameters are often combined into a vector, known as the Stokes vector:

$$\vec{S} \equiv \begin{bmatrix} S_0 \\ S_1 \\ S_2 \\ S_3 \end{bmatrix} \equiv \begin{bmatrix} I \\ Q \\ U \\ V \end{bmatrix} \quad (1.11)$$

The parameter I is a measure of total power in the wave, Q and U represent the linearly polarized components, and V represents the circularly polarized component. Usually, to measure Stokes parameters of light, six measurements are needed. The four linear measurements, I_0 , I_{45} , I_{90} , I_{-45} , are obtained after light passes through an analyzer oriented at 0° , 45° , 90° , and -45° respectively. To calculate the two circular components, I_{RHC} , and I_{LHC} , of Stokes parameter, measurements are obtained after light passes through a quarter wave plate oriented at 45 degrees and the analyzer at 0° , and 90° respectively. The Stokes parameters are also related to the amplitudes of the components of the electric field, E_x and E_y , resolved in two perpendicular directions normal to the direction of propagation, $E_x = E_{x0}(t)\cos(\omega t + \delta_x)$ and $E_y = E_{y0}(t)\cos(\omega t + \delta_y)$. Measurement of the amplitudes, $|E_{x0}(t)|$ and $|E_{y0}(t)|$, and the phase difference, $\delta_x - \delta_y$ is sufficient to determine the pure polarization state,

$$\begin{aligned}
I &= I(0) + I(90) = \langle |E_{x0}(t)|^2 \rangle + \langle |E_{y0}(t)|^2 \rangle \\
Q &= I(0) - I(90) = \langle |E_{x0}(t)|^2 \rangle - \langle |E_{y0}(t)|^2 \rangle \\
U &= I(45) - I(-45) = \text{Re} \langle E_{x0}(t) E_{y0}(t) \rangle = 2 \langle E_{x0}(t) E_{y0}(t) \cos(\delta_x - \delta_y) \rangle \\
V &= I_{RHC} - I_{LHC} = \text{Im} \langle E_{x0}(t) E_{y0}(t) \rangle = 2 \langle E_{x0}(t) E_{y0}(t) \sin(\delta_x - \delta_y) \rangle
\end{aligned} \tag{1.12}$$

where, $I(\varphi)$ is the intensity of light polarized in direction φ from the x axis, and the angle brackets, $\langle \dots \rangle$, denote a time average.

Physically, there are only three parameters: the phase difference and semi-major and semi-minor axes. Therefore, for purely polarized monochromatic light, there is an equation connecting the four parameters, $I^2 = Q^2 + U^2 + V^2$. In general, light may be partially polarized and the degree of polarization (DOP) is less than unity and defined as:

$$DOP = \frac{\sqrt{Q^2 + U^2 + V^2}}{I} \tag{1.13}$$

Knowing the DOP and normalized Stokes parameters is sufficient to determine the polarization state of light. Normalized Stokes parameters are defined as:

$$S_n \equiv \begin{bmatrix} Q_n \\ U_n \\ V_n \end{bmatrix} \equiv \begin{bmatrix} Q/I \\ U/I \\ V/I \end{bmatrix} \quad (1.14)$$

The degree of polarization in this case is:

$$DOP = \Pi = \sqrt{Q_n^2 + U_n^2 + V_n^2} \quad (1.15)$$

Stokes vectors can describe quantitatively unpolarized, partially polarized, and polarized light. Stokes parameters have dimension of flux density and can be measured or calculated, hence we primarily chose them to describe light polarization in the analysis of polarimetric measurements.

1.3.2.2 Jones Formalism

We can write the scalar components of $\mathbf{E}(z,t)$ in the form of a 2x1 column vector after dropping explicit reference to \hat{x} and \hat{y} unit vectors:

$$\mathbf{E}(z,t) = \begin{bmatrix} E_x \cos\left(\omega t - \frac{2\pi}{\lambda} z + \delta_x\right) \\ E_y \cos\left(\omega t - \frac{2\pi}{\lambda} z + \delta_y\right) \end{bmatrix} \quad (1.16)$$

Since the time oscillation of the field is known and is the same for both field components, eq. (1.16) can be further simplified to:

$$\mathbf{E}(z) = e^{-j2\pi z/\lambda} \begin{bmatrix} E_x e^{j\delta_x} \\ E_y e^{j\delta_y} \end{bmatrix} \quad (1.17)$$

The wave representation of eq. (1.17) can be simplified even further by dropping the harmonic spatial variation in the leading exponent. By choosing for example $z = 0$ plane we come up with the Jones vector description:

$$\mathbf{E}(0) = \begin{bmatrix} E_x e^{j\delta_x} \\ E_y e^{j\delta_y} \end{bmatrix} \quad (1.18)$$

Time and space dependence of the entire wave can be reconstructed by a simple operation on the Jones vector as follows

$$\mathbf{E}(z, t) = \text{Re} \left[\mathbf{E}(0) e^{j(\omega t - 2\pi z/\lambda)} \right] \quad (1.19)$$

For further simplification, the Jones vector can be written as:

$$\mathbf{E} = \begin{bmatrix} \widetilde{E}_x \\ \widetilde{E}_y \end{bmatrix} \quad (1.20)$$

Where

$$\widetilde{E}_x = E_x e^{j\delta_x}, \quad \widetilde{E}_y = E_y e^{j\delta_y} \quad (1.21)$$

The wave intensity can be simply expressed as the sum of the squared amplitudes of the components along the orthogonal directions

$$I = \left| \widetilde{E}_x \right|^2 + \left| \widetilde{E}_y \right|^2 = E_x^* E_x + E_y^* E_y = \mathbf{E}^H \mathbf{E} \quad (1.22)$$

The hermitian adjoint \mathbf{E}^H is defined as the complex conjugate of the transpose of the matrix (vector) and is given by:

$$\mathbf{E}^H = \left[\widetilde{E}_x^* \quad \widetilde{E}_y^* \right] \quad (1.23)$$

The Jones vector does not completely describe partial or random polarization states.

1.3.2.3 Complex Polarization Ratio

Jones vector representation offers a concise description of the polarization state of polarized light. In fact, the complete polarization information of the wave is contained in the complex amplitude \widetilde{E} . When only the azimuth, θ , and ellipticity angle, ε , of the elliptic vibration of the electric vector are considered (i.e., the size of the ellipse or

intensity of light is not considered), one can further simplify the Jones vector representation to a single complex number. The complex number is obtained from the Jones vector of eq. (1.20) by taking the ratio of the two complex elements of the Jones vector, such that:

$$\chi = \widetilde{E}_y / \widetilde{E}_x \quad (1.24)$$

When \widetilde{E}_x and \widetilde{E}_y are expressed in terms of their magnitude and angle, the complex polarization ratio χ is given by:

$$\chi = \frac{E_y}{E_x} e^{j(\delta_y - \delta_x)} \quad (1.25)$$

The magnitude and phase of the complex polarization ratio are given by:

$$|\chi| = \frac{E_y}{E_x}, \arg(\chi) = \delta_y - \delta_x \quad (1.26)$$

1.3.3 Polarization Properties of Materials

One motivation to study light polarization is the fact that many biological tissues are anisotropic. A dielectric medium is anisotropic if its macroscopic optical properties or dielectric constant depend on direction of the electric field oscillation. The macroscopic properties are governed by properties such as the shape orientation and organization in space of the individual molecules.

1.3.3.1 Intrinsic Birefringence

In the case of crystals, birefringence arises from anisotropic polarizability of molecules and is referred to as intrinsic birefringence. In an anisotropic dielectric medium, the relationship between the vectors D , electric flux density, and E , electric field, depends on the direction of the vector E , and these two vectors are not necessarily

parallel. If the medium is linear, nondispersive, and homogeneous, each component of D is a linear combination of the three components of the electric field vector E .

$$D_i = \sum_j \epsilon_{ij} E_j \quad (1.27)$$

Where the indices $i, j = 1, 2, 3$ denote the $x, y,$ and z components. The dielectric properties of the medium are described by the electric permittivity second-rank tensor $\{\epsilon_{ij}\}$. The electric permittivity tensor is symmetrical, $\epsilon_{ij} = \epsilon_{ji}$, therefore it is characterized by six independent numbers. Usually, even fewer coefficients are necessary due to other symmetries. If we assume that the 1, 2, 3 coordinate system lies along the crystal's principal axes, the coordinate system for which the off-diagonal elements of ϵ_{ij} vanish so that E and D are parallel, then the permittivities $\epsilon_1 = \epsilon_{11}, \epsilon_2 = \epsilon_{22}$, and $\epsilon_3 = \epsilon_{33}$ correspond to refractive indices $n_1, n_2,$ and n_3 given by:

$$n_1 = \left(\frac{\epsilon_1}{\epsilon_0} \right)^{1/2}, \quad n_2 = \left(\frac{\epsilon_2}{\epsilon_0} \right)^{1/2}, \quad n_3 = \left(\frac{\epsilon_3}{\epsilon_0} \right)^{1/2} \quad (1.28)$$

and are known as the principal refractive indices where ϵ_0 is the electric permittivity of free space. For a certain class of crystals, called uniaxial crystals, $n_1 = n_2 = n_o$ and $n_3 = n_e$. n_o and n_e are called the ordinary and the extraordinary indices, respectively. The crystal is called positive uniaxial for $n_e > n_o$, and negative uniaxial for $n_e < n_o$. The z axis of a uniaxial crystal is called the optic axis. A symmetrical second-rank tensor is geometrically represented by a quadratic surface (an ellipsoid) defined by the quadric representation

$$\sum_{ij} \epsilon_{ij} x_i x_j = 1 \quad (1.29)$$

which is invariant to the choice of coordinate system. Because of the diagonality of ϵ_{ij} in the principal coordinate system, the index ellipsoid takes the particularly simple form:

$$\epsilon_1 x_1^2 + \epsilon_2 x_2^2 + \epsilon_3 x_3^2 = 1 \quad (1.30)$$

From the quadric representation of the electric impermeability tensor $\eta = \varepsilon_0 \varepsilon^{-1}$, $\sum_{ij} \eta_{ij} x_i x_j = 1$, the index ellipsoid using the principal axes as a coordinate system takes

the form:

$$\frac{x_1^2}{n_1^2} + \frac{x_2^2}{n_2^2} + \frac{x_3^2}{n_3^2} = 1, \quad (1.31)$$

where $1/n_1^2$, $1/n_2^2$, and $1/n_3^2$ are the principal values of η .

In an electro-optic medium η_{ij} is a slowly varying function of the steady electric field, E with components (E_1, E_2, E_3) . As a result, the index ellipsoid is modified. η_{ij} is now a function of E and when represented through a Taylor's series expansion about $E=0$ yields:

$$\eta_{ij}(E) = \eta_{ij} + \sum_k r_{ijk} E_k + \sum_{kl} s_{ijkl} E_k E_l + \dots, \quad i, j, l, k = 1, 2, 3 \quad (1.32)$$

where $\eta_{ij} = \eta_{ij}(0)$, $r_{ijk} = (\partial \eta_{ij} / \partial E_k) |_{E=0}$, and $s_{ijkl} = \frac{1}{2} (\partial^2 \eta_{ij} / \partial E_k \partial E_l) |_{E=0}$

If the change of the refractive index is proportional to the applied electric field then the effect is known as the linear electro-optic effect or the Pockels effect. When refractive index change is proportional to the square of the applied electric field then the effect is known as the quadratic electro-optic effect or the Kerr effect. The $3^3 = 27$ coefficients are known as the linear electro-optic coefficients or the Pockels coefficients and form a third-rank tensor, while the $3^4 = 81$ coefficients are known as the quadratic electro-optic coefficients or the Kerr coefficients and form a fourth-rank tensor. The value of the coefficients r and s depends on the direction of applied electric field and incident light polarization. In many materials the third term is negligible and the medium is then called a Pockel's medium or cell.

$$\eta_{ij}(E) = \eta_{ij} + \sum_k r_{ijk} E_k, \quad i, j, k = 1, 2, 3 \quad (1.33)$$

Some common Pockels cells include $\text{NH}_4\text{H}_2\text{PO}_4$ (ADP), KH_2PO_4 (KDP), LiNbO_3 , LiTaO_3 , and CdTe . The mismatch between the ordinary and extraordinary refractive indices in an anisotropic medium exhibiting the Pockels effect produces a cumulative fixed optical retardance, i.e. phase difference induced between two orthogonally polarized light beams after traversing a given material thickness (L), proportional to the birefringence $\Delta n = n_e - n_o$. However, if a voltage V is applied across two faces of the cell separated by a distance d , then the phase change will include a variable component proportional to V in addition to the fixed phase component, therefore making the medium act as a dynamic wave retarder. The phase shift takes the form $\varphi = n(E)k_0L = 2\pi n(E)L/\lambda_0$. When a light beam travels through a Pockel's cell of length L to which an electric field $E = V/d$ is applied it undergoes a phase change $\varphi = \varphi_0 - \pi \frac{V}{V_\pi}$, where V is the applied voltage and $V_\pi = \frac{d \lambda_0}{L r n^3}$. The parameter V_π is known as the half-wave voltage and is the voltage at which the phase shifts by π . For lithium niobate, a uniaxial crystal, the index ellipsoid or, the optical indicatrix, is given by $\frac{x^2}{n_o^2} + \frac{y^2}{n_o^2} + \frac{z^2}{n_e^2} = 1$. Lithium niobate has 3m crystal symmetry and its electro-optic

coefficients are as follows:

$$\begin{pmatrix} 0 & -r_{22} & r_{13} \\ 0 & r_{22} & r_{13} \\ 0 & 0 & r_{33} \\ 0 & r_{51} & 0 \\ r_{51} & 0 & 0 \\ -r_{22} & 0 & 0 \end{pmatrix} \quad (1.34)$$

For an anisotropic medium exhibiting the Pockel's effect, the two normal modes propagate with different velocities. The cumulative optical retardance δ , i.e. phase difference between two orthogonally polarized light beams after traversing a given

thickness of material is determined by the degree of birefringence $\Delta n = n_e - n_o$, where n_e and n_o are the refractive indices experienced by light linearly polarized along the fast and slow axes of the birefringent medium, respectively [13]. The relationship:

$$\delta(z) = (2\pi / \lambda_0) \cdot \Delta n(\lambda) \cdot z \quad (1.35)$$

relates the cumulative retardance, $\delta(z)$, experienced after traversing a distance z to birefringence $\Delta n(\lambda)$, vacuum wavelength λ_0 , and z [16].

1.3.3.2 Form Birefringence

In 1912, O. Wiener published a general theory of dielectric constant of mixed systems; he obtained expressions for the birefringence of lamellar sheets and suspensions of parallel cylinders. Oldenbourg et al. translated Wiener's work and calculated birefringence of the rod shaped Tobacco Mosaic Virus and DNA and found excellent agreement with experimental values. Form-birefringence is an optical property that arises from ordered arrays of anisotropic light scatterers which are larger than single molecules but smaller than wavelength of light surrounded by media with different refractive index.

Incident light electric field can be decomposed into its two orthogonal components, (E_{\perp}) and (E_{\parallel}) . (E_{\perp}) induces surface charges that induce an electric field (E_0) and hence anisotropically modify phase and amplitude of (E_{\perp}) relative to (E_{\parallel}) . This modification leads to a larger refractive index (n_s) experienced by (E_{\perp}) compared to that (n_f) experienced by (E_{\parallel}) . Accumulated phase retardation, δ in radians, after propagating a distance Δz is given by:

$$\delta = \left(\frac{2\pi \cdot \Delta n(\lambda)}{\lambda_0} \right) \cdot \Delta z \quad (1.36)$$

where $\Delta n(\lambda) = n_f(\lambda) - n_s(\lambda)$, and λ_0 is the center wavelength.

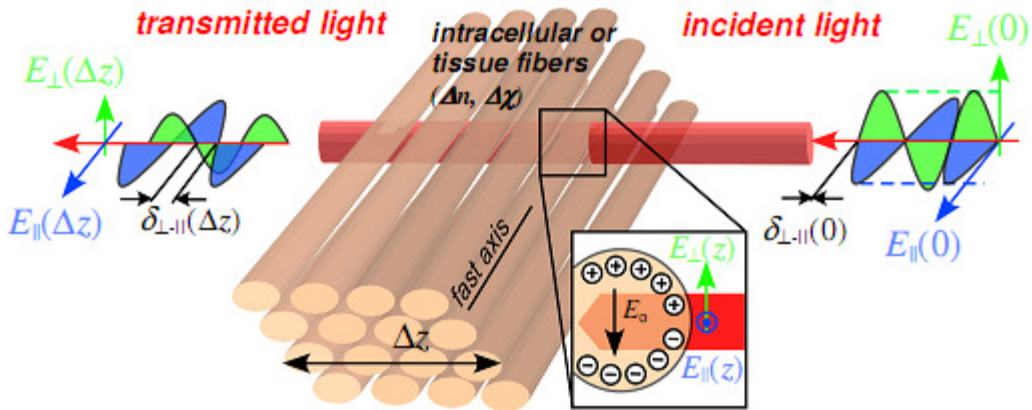


Figure 1.4: Form-birefringence (Δn) origin in fibrous structures. Electric field perpendicular component (E_{\perp}) produces a surface charge density with an induced field (E_0). This changes dielectric susceptibility and gives higher refractive index (n_s) relative to the one experienced by (E_{\parallel}) [17].

1.4 PHYSIOLOGY OF THE RETINA AND GLAUCOMA

1.4.1 Anatomy of the Eye

Light enters the eye through the pupil and is focused by the cornea and lens onto the retina (Figure 1.5). The retina is composed of light sensitive cells lining the back of the globe. These cells, commonly classified as either rods (responsible for low-light, peripheral vision) or cones (responsible for high-resolution, color vision), react to the incoming light and produce an electrical signal. The signal propagates through the retinal ganglion cells (RGCs), travels down the RGC axons in the retinal nerve fiber layer (RNFL), and converges at the optic nerve as shown in Figure 1.5.

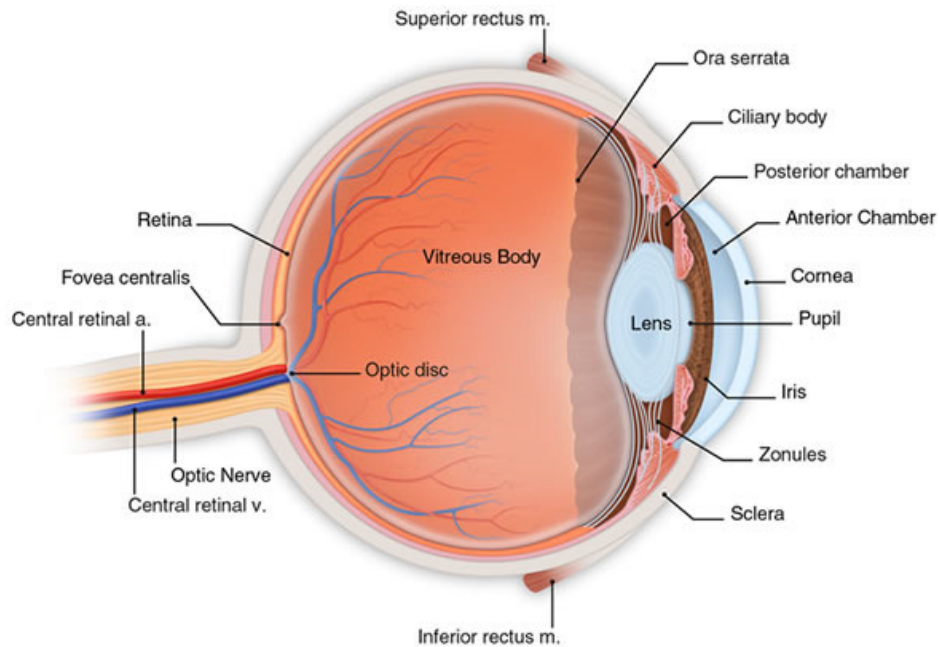


Figure 1.5: Lateral section of adult human eye. Light passes through the cornea and is focused by the lens onto the retina. RGC axons converge into the optic nerve.

Rather than being nourished by opaque blood vessels that would block the path of light to the retina, the cornea and lens are nourished by a transparent fluid called the aqueous humor. This fluid is produced by the ciliary body, and is secreted by the ciliary processes into the posterior chamber. Some of this fluid flows between the lens and the iris into the anterior chamber. The majority of fluid outflow occurs via the trabecular outflow marked by the arrows in Figure 1.6. The aqueous humor drains through the trabecular meshwork, through Schlemm's canal, and finally into collector channels that absorb it into systemic circulation [18].

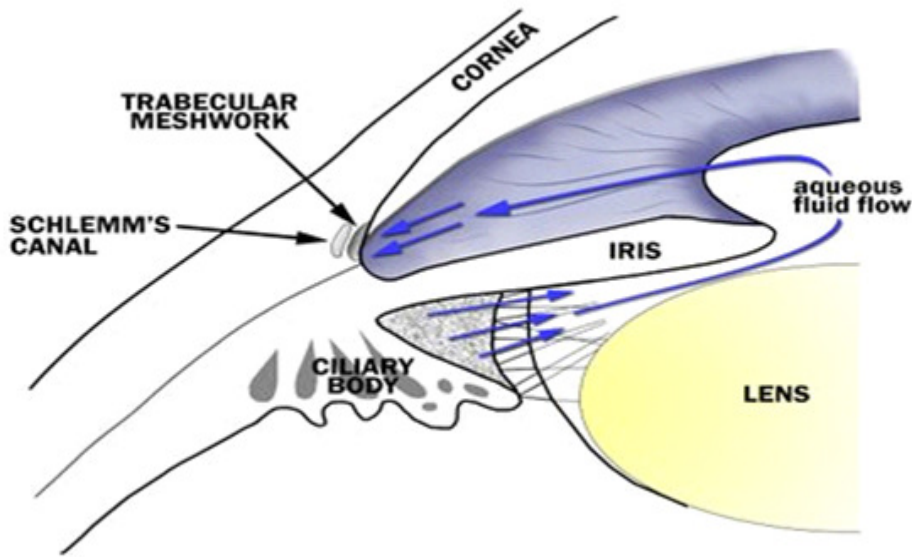


Figure 1.6: Diagram of aqueous humor flow pathway. The ciliary processes excrete aqueous humor. The aqueous humor flows between the iris and lens into the anterior chamber, and the majority of the fluid outflows through the trabecular outflow pathway marked by arrows

1.4.2 Pathophysiology of Glaucoma

Glaucoma is not a single disease, but rather a group of diseases with some common characteristics. Thus, glaucoma can be classified by various categories such as mechanism, age of onset, intraocular pressure, and stage of disease. Ultimately, glaucoma is characterized by a progressive, irreversible RGC degeneration that leads to partial or complete visual function loss. The mechanisms of glaucoma are not completely understood; however, several risk factors such as age, race, and most importantly intraocular pressure (IOP) have been identified. IOP is determined by the rate of aqueous humor production compared to the rate of aqueous humor drainage. Most often,

increased IOP is due to high resistance to drainage, as aqueous humor must traverse three layers of trabecular meshwork and the Schlemm's canal in order to exit the eye.

Even though risk factors have been identified, a common underlying cause of glaucoma is not known as many glaucoma patients have normal IOP levels. One theory is that increased IOP induces mechanical stress on the RGC axons at the level of the lamina cribrosa, which disrupts axoplasmic flow causing eventual nerve fiber death. Another hypothesis is that the death of RGCs is due to an insufficient blood supply to the optic nerve head, which could be the result of abnormal circulation at a number of potential locations. Also, many molecular and cellular aberrations in glaucomatous nerve fibers such as abnormal astrocyte deposition of collagen in the lamina cribrosa, changes in the extracellular matrix, and alteration of elastin, fibronectin, or other cellular proteins have been observed. However, this biochemical theory of glaucoma is inconclusive, as some of these changes have been observed in healthy, aging optic nerves. Finally, a neurochemical hypothesis has been proposed as it has been observed that high levels of certain excitotoxins, calcium, nitric oxide, and free radicals are associated with glaucoma [18].

Regardless of the cause, glaucoma patients suffer RGC loss that can result in partial or complete blindness. Currently, no natural or induction mechanism is recognized for repairing or replacing damaged RGCs. However, methods are available for slowing or stopping the progression of RGC loss, making early detection and diagnosis critical for treatment of glaucoma.

1.4.3 Clinical Treatment of Glaucoma

1.4.3.1 Current Diagnostic Methods

Because glaucoma is a progressive disease, systematic examination of the RNFL and optic nerve are necessary in order to detect early, subtle changes indicative of the disease. Several subjective and objective methods have been developed to examine the eye and screen for glaucoma. However, because glaucoma in its early stages shows no obvious symptoms, patients are often left undiagnosed until noticeable vision loss has occurred. Evidence shows that up to 40% of nerve fibers may be irreversibly lost before a diagnostic visual field defect is detected by the ophthalmologist. Current subjective methods include ophthalmoscopy, biomicroscopy, and various vision testing techniques. Ophthalmoscopy and biomicroscopy are tools that clinicians use to examine the eye and detect any observable signs of glaucoma. Of the tests currently employed, the visual field test and its many variations are the most common. The visual field defines all that is visible to one eye at a given time, and the visual field test attempts to compose a map of this field that is compared to standard map values in an attempt to detect abnormalities. While careful observation techniques can be used as a diagnostic tool, variability between observers and patients inevitably exists. A clinical need exists to create a more objective method for glaucoma detection [18].

1.4.3.2 Objective Examination Methods

To fill the need for an objective retinal examination method, many technologies have been developed including confocal scanning laser ophthalmoscopy (CSLO), optical coherence tomography (OCT), and scanning laser polarimetry (SLP). The most recent

CSLO technology available, released in 1999, is the Heidelberg Retinal Tomograph (HRT) II. CSLO utilizes confocal technology to combine multiple shallow-depth-of-field images to create a three dimensional topographic view of the retina, specifically the optic disc. Glaucoma produces changes in the morphology of the optic nerve head that can be observed with a CSLO, and quantification of retinal characteristics such as cup to disc ratio and optic nerve head diameter can provide objective measurements for glaucoma diagnosis. However, CSLO requires subjective input from the operator and provides no quantitative data on the RNFL. Also, because of low numerical aperture of the eye, resolution is limited to 200-300 μ m.

OCT measures RNFL thickness, optic disc tomography, and macular thickness. Carl Zeiss Meditec (Dublin, CA) most recently introduced the Cirrus HD OCT in 2007, which replaces the Stratus OCT that was released in 2002. OCT technology is discussed in much greater depth in section 1.2. Quantitative RNFL thickness measurements are obtained by determining the retinal boundaries (the vitreoretinal interface and the retinal pigment epithelium), which have abrupt changes in reflectivity. Retinal thickness measurements from six radial scans provide optic disc topography. Macular thickness can also be obtained through a second measurement.

SLP uses a polarization sensitive measurement to measure the phase retardation that occurs when the laser is incident on birefringent tissue such as the RNFL. The most recent commercially available SLP instrument is the GDx VCC, released in 2002 by Carl Zeiss Meditec (Dublin, CA). RNFL thickness can be estimated from the phase retardation measurements based on a linear relationship between the two assuming a constant birefringence. If the RNFL thins due to glaucoma, the phase retardation is expected to decrease, and glaucoma can be detected by observing phase retardation trends over time. However, the cornea and lens are also birefringent structures, and their

birefringence varies from person to person, so SLP phase retardation measurements are affected in varying degrees. To compensate for this discrepancy, the GDx VCC uses a variable corneal compensator (VCC) that reduces impact of non-RNFL phase retardation measurement. Table 1 shows statistical data in diagnosing glaucoma for the most recent commercially available system of each technology. As the table demonstrates, despite the promise of these technologies, measured sensitivity is relatively low.

Table 1.1: ROC curve areas and sensitivities at fixed specificities for discriminating between glaucomatous and healthy eyes [18].

Parameter	Area under ROC curve	Sensitivity/specificity (%)
HRT II Vertical cup/disc ratio*	0.83	59/95, 69/80
StratusOCT inferior RNFL thickness	0.92	64/95, 89/80
GDx VCC Nerve Fiber Indicator	0.91	61/97, 87/80

*HRT Moorfields Regression Analysis results performed similarly to vertical cup/disc ratio, but results are not reported because ROC curve areas and sensitivities at fixed specificities cannot be calculated for categorical variables.

1.4.3.3 Treatment Options

Current treatment options focus on the reduction of IOP, which helps slow glaucoma progression. Reduction of IOP can be done either by decreasing aqueous humor production or increasing drainage and can be accomplished by application of several different topical medications. Research is being conducted on medications that offer neuroprotection of the optic nerve that can be used in conjunction with IOP reducers. When patients do not respond to drug therapy, surgical options exist. Trabeculectomy is the most common surgical procedure performed and can be accomplished either conventionally or with laser surgery. In this procedure, a flap is created in the sclera of the eye, and a piece of the trabecular meshwork is removed to

create a hole that allows aqueous humor to drain. Another procedure is laser iridotomy, where a laser is used to create a small hole in the iris, equalizing pressure between the anterior and posterior chambers and correcting angle-closure glaucoma. Finally, aqueous shunts can be implanted in the eye to drain fluid directly, but many possible complications and factors exist that have to be accounted for, so this option is only performed in extreme cases[18].

1.4.3.4 RNFL Birefringence

Huang and Knighton showed that the RNFL is birefringent due to the common orientation of RGC axon neurotubules [19]. As polarized light travels through the RNFL, light polarized perpendicular to axon neurotubules travels slower and is thus phase delayed compared to light polarized parallel. Using TEM cross-sections of toad RNFL, Zhou and Knighton showed that RNFL birefringence is $3.2 \cdot 10^{-4}$ at 560 nm [20]. As RGC axons degenerate, non-birefringent glial cells replace them. Glial content can vary substantially and hence thickness change may not accurately reflect neurotubules loss. Since RNFL birefringence is mainly due to neurotubules, loss of RNFL birefringence should be detected earlier than and at a faster rate than RNFL thickness [21], making birefringence detection a better prognosticator of glaucoma than any of the subjective methods discussed.

Chapter 2: Swept Source Polarization Sensitive Optical Coherence Tomography Instrumentation

2.1 BACKGROUND

Optical Coherence Tomography (OCT) was first developed as a time domain (TD) technique in 1991 by Huang et al. Frequency domain (FD) techniques were later introduced in 1995 [11, 22], and eventually gained in use after 2003 when spectral domain OCT was shown to hold several advantages over time domain OCT in terms of signal-to-noise ratio, sensitivity and acquisition speed [13-15]. With spectral domain OCT, high speed and high resolution 2-, 3-D imaging became possible. [12, 13]

Polarization-sensitive OCT (PS-OCT), being a functional extension of OCT, can measure biological sample birefringence, optic axis orientation, and form-biattenuance [23]. PS-OCT provides additional contrast to standard OCT by measuring fringe intensity and phase of two orthogonal polarization states detected from the sample. The first PS-OCT system reported in the literature was described in 1992 [24], with the first images being presented in 1997 [25]. Early PS-OCT systems utilized bulk optics, but eventually, fiber-based systems were developed and demonstrated. Fiber-based systems are smaller in size and easier to align and handle than free space systems. However, free space systems' polarization state at the reference and sample paths is easier to control and reference to a fixed laboratory frame. Controlling polarization state of light with single mode fiber-based systems is more difficult because of the random changes that occur in single mode optical fiber [26]. To overcome these limitations of fiber based systems, several groups developed different polarization sampling and analysis methods to deduce polarimetric properties of the sample. Saxer (2000) proposed a PS-OCT system that used

Stokes vectors to determine the eigen axis on the Poincare sphere [27]. Roth [28] used an algebraic method and polarization sensitive free space components in the sample arm to measure birefringence. Park [29] developed a Jones matrix approach with sequential polarization modulation in order to measure all four elements of Jones matrix corresponding to the polarimetric properties of a sample. Jiao et al. used two superposed light sources [30] and later developed continuous polarization modulation [31] to measure polarimetric properties. More recently, frequency domain PS-OCT (FD-PS-OCT) rather than TD-PS-OCT was developed to obtain higher sensitivity and speed [32, 33]. Yamanari suggested use of a modulated input polarization state, requiring only one A-scan per probed location to calculate sample retardation at the expense of a reduction in measurement depth by a factor of three [34]. Using additional frequency shifters, Oh et al. was able to develop a system to measure sample birefringence with only one wavelength scan without the measurement depth limitation [35]. Polarization maintaining (PM) fibers offer another design option to address the constraints using standard single mode fiber systems. Using PM fibers, an OCT system capable of characterizing retardance and axis orientation of a birefringent plate with a single A-scan was demonstrated [36-38]. Al-Qaisi was able to create an image of biological tissue free of ghost lines using a PM fiber based TD-PS-OCT system [39]. Gotzinger et al. was able to develop and demonstrate a FD-PS-OCT system using PM fibers to perform retinal scans. This setup was successful with a stationary setup, but applications requiring fiber movement encounter potential problems. Recently, Wang et al. obtained birefringence and relative axis orientation from human finger nails and skin using PM fiber based FD-PS-OCT [40].

Typically, OCT imaging of the retina has been performed using an 800 nm wavelength where infrared water absorption is minimal. However, penetration of light

into the retina at 800 nm is limited due to absorption and scattering by the retinal pigment epithelium (RPE), 1 μm wavelength light is scattered less and penetrates deeper [8, 9]. Numerous groups have demonstrated both SD-OCT and SS-OCT using 1 μm wavelength [32-36]. Yamanari demonstrated retinal imaging using SS-PSOCT at 1 μm wavelength that allowed birefringence visualization of the sclera [34].

One particularly promising application of PSOCT retinal imaging is early detection of glaucoma. Huang and Knighton showed that RGCs are the main contributor to RNFL birefringence [19]. In glaucoma, the degenerated RGC axon neurotubules are replaced by non-birefringent glial cells, so birefringence is believed to decline earlier and at a faster rate than RNFL thickness [21]. Standard OCT systems cannot detect this compositional change in the RNFL as glial content in healthy eyes varies significantly [41]. On the other hand, PS-OCT can be used to determine birefringence in the RNFL [42] and distinguish it from non-birefringent layers, making earlier detection and quantification of the level of RGC degeneration in the RNFL possible [21, 43]. In glaucoma patients, measurements of RNFL birefringence show a reduction compared to normal eyes [44, 45]. If more accurate birefringence measurement is possible, RGC axon degeneration might be detected earlier, and therefore glaucoma can be detected at an earlier stage. Using a TD bulk optics PS-OCT system and a multiple-state non linear fitting algorithm (NLFA), Kemp et al. obtained accurate RNFL birefringence measurements in primate retinas [46].

In this chapter, we present a single mode fiber-based SS-PS-OCT system at 1 micron that requires no calibration or post-conditioning of the acquired spectra to obtain highly accurate birefringence measurements. The system uses hardware dispersion compensation, achieves real time display at 34 frames per second, and utilizes a quadrupled clock to acquire fringe signals in orthogonal polarization channels without the

need for spectral post processing. To obtain accurate birefringence, phase retardation, and optic axis orientation measurements with, as we believe, the least uncertainty to date, we use three different polarization states per probed location on the retina. We completed a preclinical study to measure RNFL birefringence in 10 healthy patients aged 25-61. Three measurements were obtained on both eyes for each patient. A complete dataset from one patient is presented in chapter 5. The fiber based PSOCT system we built was configured in a wheeled cart with a slit-lamp interface similar to that routinely used at ophthalmologists' offices, making the instrument portable and practical for clinical use.

2.2 OPTICAL CONFIGURATION

The SS-PSOCT system (figure 2.1) consists of a swept laser source and a fiber interferometer with source, reference, clock and trigger, sample, and detection paths.

Polarization mode dispersion (PMD) has been investigated widely and in depth in telecommunications [26]. In single-mode fiber (SMF), core ellipticity, noncircular symmetry stresses, and tight bends give rise to random birefringence that varies with wavelength. The two orthogonal polarization states, in the presence of PMD, travel through fiber at different speeds. This differential phase delay and differential group delay cause a broadening of the PSF. Higher orders of PMD can degrade performance of PSOCT systems.

The optical fiber signal interferometer was built with care to minimize PMD. Fiber length in the signal interferometer was kept as short as possible, and the whole fiber system was routed inside a 10 inch diameter polyvinyl chloride (PVC) open-top annulus tubing. Construction and packaging of the PS-OCT interferometer helped minimize

PMD and allowed the acquisition of repeatable and accurate polarization sensitive measurements. Since PMD in the system was sufficiently reduced a calibration method to correct for PMD was not required. HI1060 FLEX fiber further reduces PMD compared to HI1060 fiber used; however, off the shelf optical components using the FLEX fiber were not readily available.

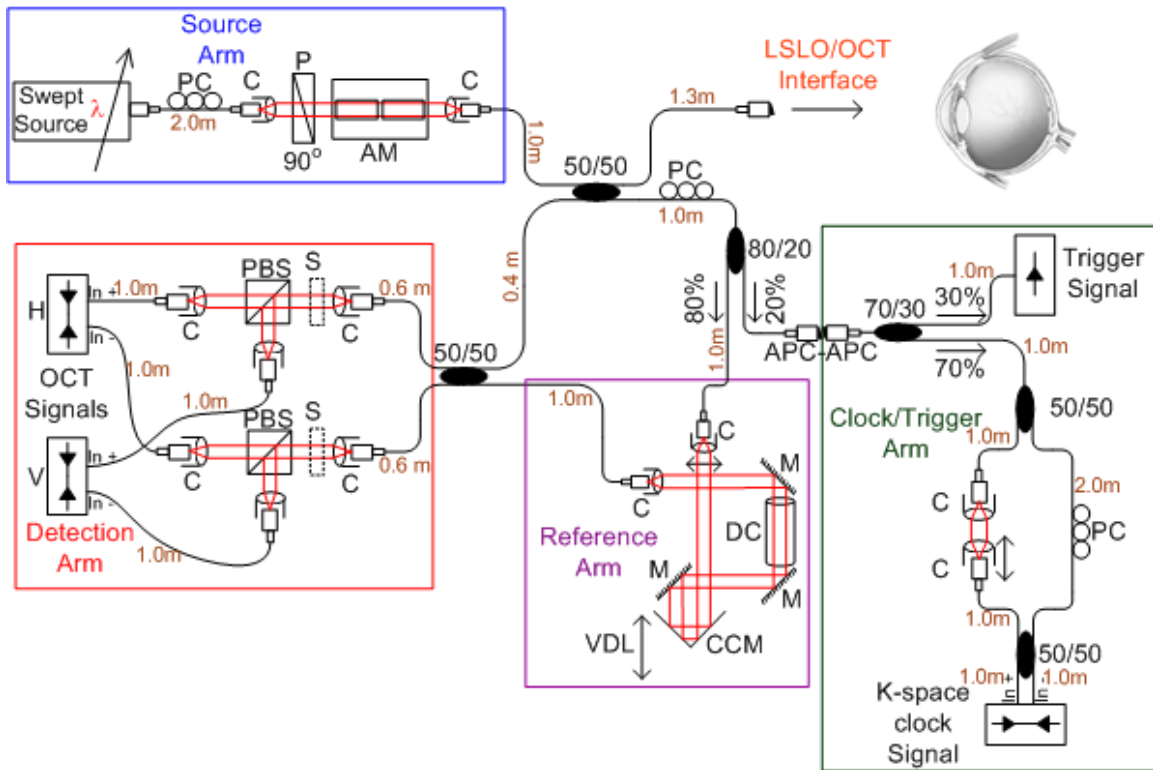


Figure 2.1: SS-PSOCT system schematic with fiber length dimension in brown. PC: polarization controller, P: polarizer, AM: broadband amplitude modulator, C: collimator, CCM: corner cube mirror, PBS: polarizing beam splitter. S: solenoid, VDL: variable delay line, DC: dispersion compensation glass rod, M: silver coated mirror

2.2.1 Source Path

The source path is comprised of a swept laser source (HSL-1000 by Santec Corporation, Komaki, Aichi, Japan) with a sweep repetition rate, f_R , of 34 KHz, a center wavelength, λ_0 , of 1059 nm, a full-width-half-max (FWHM) spectral bandwidth, $\Delta\lambda$, of 58 nm, an average output power of 2.9 mW per cycle, and a duty cycle of 0.64. The swept laser source is fiber terminated to an angle polished FC/APC bulkhead connector in order to minimize back reflection. Light from the laser travels through a single mode fiber (HI1060 by Corning Incorporated, Corning, NY) connected to a manually adjusted fiber polarization controller (FPC560 by Thorlabs, Inc, Newton, NJ). The polarization controller utilizes stress-induced birefringence to create three independent fractional wave plates that transform any arbitrary input polarization state into any desired output polarization state with control over the full Poincare sphere. The polarization controller is configured to transform the source light into vertical linear polarization (0°) state. Light is then collimated into free space through a FiberPort (PAF-X-2-1064 by OFR inc., Caldwell, NJ) and then propagates through a Glan-Thompson linear prism polarizer with a high efficiency antireflection coating at 1000-1600nm (MGT25E8-HEAR1000-1600 by Karl Lambrecht Corp., Chicago, IL) also oriented vertically (0°). The manual polarization controller (PC) ensures that the polarization state of light exiting the fiber segment matches the axis of the polarizer used in the setup to maximize light transmission. Light then enters a modified broadband bulk electro-optic phase modulator (4104 broadband amplitude modulator by NewFocus, Santa Clara, CA) with a 2mm diameter clear aperture. The modulator consists of two matched, 20mm long Magnesium Oxide doped Lithium Niobate (MgO: LiNbO₃) crystals. The two crystals are mounted with their optical axes at 45 degrees to the horizontal in the lab frame so that when input polarization is either horizontally or vertically polarized, a variable phase delay

proportional to applied voltage is introduced between ordinary and extraordinary field components. Applied voltage to the second crystal is equal in magnitude but opposite in polarity to that applied to the first crystal so phase retardation is doubled and effect of intrinsic birefringence is neutralized. If not accurately aligned, however, the MgO doped LiNbO₃ crystals can create undesired image artifacts. Light exiting the modulator is coupled back into single mode optical fiber through an input FiberPort (PAF-X-2-1064). The input and output FiberPorts, the Glan-Thompson polarizer, and the modified modulator are all mounted on an aluminum block to minimize thermal and environmental vibration. Light is equally split in two paths using a 50/50 non-polarizing broadband fiber splitter (WP 10500202B2100 by AC Photonics Inc., Santa Clara, CA). The first path is the sample path, and the second is the reference and clock/trigger paths. An 80/20 broadband fused fiber splitter at the reference and clock/trigger path splits light into reference (80% segment) and clock/trigger path (20% FC/APC terminated segment).

Using a 50/50 splitter means that only 25% of the source power is available for interference since only 50% of the light is sent to the sample arm, and only 50% of that light (assuming a perfect reflector as the sample and no losses due to the sample arm optics) is returned for interference and detection. To obtain better efficiency one can use a circulator in combination with a splitter. A circulator is a nonreciprocal device; therefore, ideally 100% of the light passed through the splitter could be available for interference. Circulators have been extensively used in OCT systems at 1310nm [47]. However, at 1060nm use of circulators is still very limited since they suffer from high insertion loss and polarization mode dispersion (PMD), so usually a coupler such as an 80/20 is used at the source arm to split light between sample arm and reference and clock/trigger arms [34]. Another approach to improve system sensitivity is to use a splitting ratio other than 50/50. For example if the splitting ratio was 20/80 and source

light power was sufficiently high, one can send 20% of light to the sample and have 80% of backreflected photons returning from sample available for interference. When imaging the retina the ANSI [7] standard maximum permissible power incident on the cornea is only 1.7mW for a 1.5mm diameter incident beam at the cornea. A detailed calculation of the MPE is discussed in section 3.2.1. If close to 1.7 mW of power can be delivered to the cornea with a splitting ratio of less than 50%, then more than 50% of the reflected light can be returned for interference and increase system sensitivity. More asymmetric splitting ratios are better as long as the incident power on the cornea is just below but close to the ANSI standard. With a high power swept laser source, one can send 10% of light to the sample arm and collect 90% of light returning from the eye, which would outperform the best 1060 nm circulator currently available since at least 20% insertion loss happens at the circulator [34]. Using a 50/50 splitter and taking into consideration the minimum insertion losses in our source and sample arms, the incident power on the cornea was on average 440 μ W and was 1.15mW at the peak wavelength. With the swept laser available to us, these were found to be the maximum power outputs, and therefore the 50/50 splitter was selected.

2.2.2 Reference Path

Reference light is collimated by a PAF-X-2-1064 FiberPort collimator into free space before being coupled back into fiber using a PAF-X-5-1064 FiberPort collimator. In free space, light is reflected by a corner cube retroreflector (UBBR1-II by Newport) mounted on a software controlled motorized stage (KT-LSR75A by Zaber). Use of the retroreflector in such a way allows the change in the optical pathlength without moving launching and receiving fibers in order to keep polarization state unchanged. Light is

then reflected by a silver-coated mirror (10Z40ER.2 by Newport) oriented at 45 degrees. A second silver mirror at 45 degrees reflects the light again. The light then passes through a specifically designed glass rod that acts to balance dispersion mismatches arising from the sample arm optics and fiber length mismatches between reference and sample arms. Light is again reflected by a third and final 45 degree mirror before being coupled back into fiber using a FiberPort collimator. Although each mirror reflection attenuates the reference light, the three mirrors are used to reduce footprint. Reference arm layout allows packaging the optics tray and electronics in a single layer within the cart while matching optical path length in the sample arm. No attenuators or neutral density filters were used to reduce intensity of reference path light for optimum signal-to-noise ratio [48]. If reference light required attenuation, one of the mirrors was slightly misaligned to vary the intensity of light returning from the reference path. Use of neutral density filters to attenuate light can introduce ghost line artifacts in recorded images if not correctly placed and oriented.

To correct for dispersion mismatch between sample and reference paths, an optical simulation was performed using ZEMAX-EE software (ZEMAX® Development Corporation). The actual dispersion mismatch in the system was quantified, and a glass rod was designed using ZEMAX to balance dispersion in the system. A specified glass rod was ordered from Planar Optics and experimentally confirmed to correct for dispersion imbalance between reference and sample paths. A detailed overview of the glass rod design for dispersion balancing is discussed in chapter 3.3.

2.2.3 Clock/Trigger Path

The clock/trigger path optics consists of a 70/30 non-polarizing broadband fiber splitter. The 30% segment is FC/APC terminated and connected to a 125-MHz balanced fiber-coupled photoreceiver (1811-FC NewFocus), which serves as an intensity-based global trigger for the system. The trigger 1811-FC photoreceiver was used even though its bandwidth is much greater than the minimum required bandwidth because device was readily available and a slower detector was not. The 70% segment is directed to a simple Mach-Zehnder interferometer (MZI), which acts as the non-linear clock signal generator. After the 50/50 splitter, one arm is collimated out of fiber using a graded-index (GRIN) lens (CLS105-HI by Princetel) and coupled back into fiber by an identical GRIN lens placed on a translation stage. Light in the second arm remains in fiber and passes through a polarization controller in order to match the two arms' polarization states and maximize fringe visibility. The fiber lengths between the two arms in the Mach-Zehnder clocking interferometer (MZI) must be carefully matched to ensure that fringe frequency is zero when air space between the two collimators is zero. If unmatched, dispersion would be introduced into the system by the clock. Dispersion originating in the clock could manifest itself as an error in the estimation of laser sweep nonlinearity and cause image degradation by blurring. Increasing the air gap in arm one increases pathlength mismatch and thus clocking frequency. The swept laser source has a limited coherence length of 6 mm. A 6 mm pathlength mismatch in air between the two arms of the MZI corresponds approximately to a 23 MHz clocking frequency. Fiber length in the MZI clock needs to be on the same order as the signal interferometer fiber length. Additionally, if optical delay in the MZI clock is substantially different from the signal interferometer, a sufficient optical delay is introduced when clocking fringe output of the interferometer, causing erroneous sampling of the imaged specimen and worsening

system PSF. Section 2.4.2 details different clocking schemes used to acquire signal fringes and a comparison based on SNR, resolution, and SNR and resolution drop off with depth.

2.2.4 Sample Path

The sample path is composed of a patient interface that combines the scanning mirrors and lenses necessary to deliver OCT light beam to the subject's eye as well as a line scanning laser ophthalmoscope (LSLO). A CCD camera for the LSLO and an LED fixation target are also components of the patient interface. The setup is mounted on a modified slit lamp (SL-130 by Zeiss Meditec). A detailed description of the patient interface is provided in chapter 3.

2.2.5 Detection Path

Light returning from the sample and reference paths recombines and interferes at the 50/50 non-polarizing broadband fused fiber coupler. Light in each arm after the 50/50 non-polarizing splitter is collimated into free space. Polarizing beam splitters reflect vertically polarized light and transmit horizontally polarized light. Horizontally and vertically polarized beams are each coupled back into single mode optical fiber channels by FiberPorts (PAF-X-2-1064). The fibers are connected to two 80-MHz balanced fiber-coupled photoreceivers (1817-FC NewFocus), corresponding to horizontal (H) and vertical (V) channels. Use of balanced photoreceivers can provide several advantages such as reduced relative-intensity noise (RIN) (the dominant noise source in tunable lasers), suppressed self-interference noise, improved dynamic range, and reduced fixed-pattern noise due to reduced reference light background. Despite difficulty with

alignment, fiberports have been used extensively in our instrumentation because they provide good mechanical stability, good coupling efficiency, and tremendous flexibility in coupling both collimated and non-collimated beams in or out of single mode optical fiber.

For the clinical system, two solenoids were placed in the light path between input fiber collimators and polarization beam splitters. When solenoids are in the off state, the beams are unblocked, but when either is powered, the corresponding beam is blocked. Blocking beams remotely allows signal amplitude from one arm to be recorded without balancing since both arms are always connected to the balanced detectors.

2.3 ELECTRO OPTIC PHASE MODULATOR

2.3.1 Phase Modulator Alignment

Using the knife edge method [49], the FiberPort's lens was adjusted relative to the fiber tip until the desired beam profile was obtained. Beam waist was placed between the two crystals, and the Rayleigh range was made equal to the optical pathlength between the two crystals. The phase modulator was positioned in the light path after the first polarizer. A second polarizer was placed as an analyzer after the phase modulator, and a chopper was used to modulate light intensity at 1 KHz before detection using a 5mm diameter Germanium large-area photoreceiver (model 2033 by NewFocus). By positioning the phase modulator between crossed polarizers, alignment of the beam to complete a voltage-to-retardation calibration was possible. Output of the photoreceiver was connected to a lock-in amplifier (Model SR850 DSP). This connection along with the chopper's frequency signal eliminates background noise and provides higher signal-

to-noise ratio. The input polarizer polarizes incoming light at 0° , and light exiting the modulator transmits through the analyzer oriented at 90° . Since each of the two crystals is a Pockel's cell, retardation, $\Gamma(\lambda)$, at any wavelength is linearly dependent on applied voltage, V . Phase retardation for the first crystal is given by:

$$\Gamma = \Gamma_{0,1} - \pi \frac{V}{V_{\pi,1}} \quad (2.1)$$

Since voltage for the second crystal has opposite polarity to voltage for the first crystal, the second crystal's phase retardation is given by:

$$\Gamma = -\left(\Gamma_{0,2} - \pi \frac{-V}{V_{\pi,2}} \right) = -\Gamma_{0,2} - \pi \frac{V}{V_{\pi,2}} \quad (2.2)$$

Assuming identical crystals, then native birefringence is ideally equal for both crystals, i.e.:

$$\Gamma_0 = \Gamma_{01} = \Gamma_{02} = \frac{2\pi}{\lambda_0} (n_1 - n_2) L \quad (2.3)$$

V_π denotes the applied voltage at which the modulator introduces a π phase shift and is the same for the two identical crystals.

$$V_\pi = V_{\pi,1} = V_{\pi,2} \quad (2.4)$$

When the second crystal is oriented 90 degrees relative to the first crystal and applied voltage is of the same magnitude for both crystals and with opposite polarity, then transmittance of the combination of the two crystals is a periodic function of V given by:

$$T(V) = \sin^2 \left(\frac{\pi}{2} \frac{2V}{2V_\pi} \right) = \sin^2 \left(\frac{\pi}{2} \frac{V}{V_\pi} \right) \quad (2.5)$$

With no voltage applied, the phase modulator is designed to provide no retardation and transmittance is equal to zero. With no voltage applied, the modulator is designed to not modify the polarization state of light if the Gaussian beam is tightly

centered about the crystals' optic axis. This condition can be violated if the two crystals are not aligned exactly at 90 degrees with respect to each other, or if the crystals' optical axes are not uniform, or if the two crystal lengths are not matched.

First, the extinction ratio of the crossed polarizer/analyzer setup was maximized in the absence of the modulator. Once the polarizer/analyzer extinction ratio was maximized, the modulator was placed between the polarizers. Then, position, tilt, and rotation were each adjusted until maximum extinction ratio was attained, where extinction ratio is measured as the ratio of detected light intensity with analyzer parallel to polarizer divided by detected light intensity with analyzer oriented perpendicular to polarizer. With proper alignment, measured extinction ratio of the modulator was 117 and throughput 96%.

2.3.2 Phase Modulator Calibration

Applying constant voltage to the modulator results in wavelength dependent phase retardation and spectral variation in output polarization state. Assuming a source with a Gaussian spectrum with full width at half maximum bandwidth $\Delta\lambda$, an average polychromatic phase error, $\Delta\Phi$, given by equation (2.6) would be introduced [50].

$$\Delta\Phi = \frac{\Phi_0 \Delta\lambda}{(\sqrt{8 \ln 2} \lambda_0)} \quad (2.6)$$

where Φ_0 represents phase shift at the center wavelength λ_0 .

In our SS-PSOCT system, the modulator is driven to output three distinct polarization states: -120 degrees, 0 degrees, and +120 degrees. For the $\pm 120^\circ$ polarization states, 2.4 % or 2.9° average polychromatic phase error would be introduced if a constant voltage is applied across the spectrum. Using a swept source system allows correction of the polychromatic phase error, whereas broadband emitting sources do not

allow a similar correction. Using a wavelength dependent voltage drive enables accurate, constant phase retardation across the entire laser sweep.

Without a chopper in the light path, output of the photoreceiver is connected to a digitizer and monitored by a custom-written LabView VI. Drive signal of the high voltage amplifier is carefully calibrated to obtain a constant phase shift across the spectrum. Light passing through the modulator passes through an analyzer oriented parallel to the analyzer and a reference signal, $\text{Ref}(\lambda)$, is acquired. In a second step, the analyzer is oriented perpendicular to the input polarizer and a background signal, $\text{BG}(\lambda)$, is acquired. Theoretical signal, $\text{Th}(\lambda)$, for each of the states, $\Gamma = (-120^\circ)$, 0° , and $(+120^\circ)$ is given by:

$$\text{Th}(\lambda) = [\text{Ref}(\lambda) - \text{BG}(\lambda)] * \sin^2\left(\frac{\Gamma}{2}\right) - \text{BG}(\lambda) \quad (2.7)$$

Finally, with the analyzer oriented perpendicular to the input polarizer, voltage drive signal was applied to the modulator and varied until discrepancies between the experimentally recorded signal and the theoretically expected signal calculated from the laser spectrum was less than 0.1% or about 0.1° at any point in the spectrum for all three polarization states.

2.3.3 Precise Electro Optic Modulation

Figure 2.2 shows a polarization diverse intensity image of a ring scan about the optic nerve head (ONH) acquired using the SS-PS-OCT instrument. The image is recorded from a healthy individual's retina. A bright line artifact, referred to as a 'ghost line,' appears at a depth of about 850 microns, limiting imaging field of view and greatly corrupting the image.

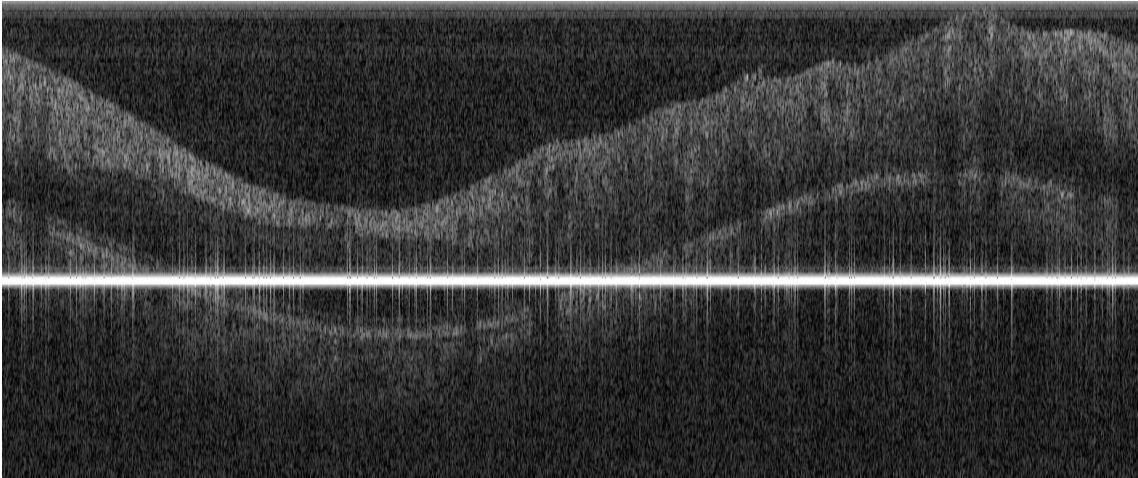


Figure 2.2: A healthy individual's retina with a bright line artifact corrupting the image and greatly limiting image field of view

The ghost line was caused by the two crystals in the electro-optic phase modulator not oriented at 90 degrees relative to each other. A Matlab® simulation using the Jones matrix formalism verified that the ghost line artifact was due to a small angular mismatch between the two crystals comprising the electrooptic phase modulator. The simulation showed that larger angle mismatches caused the ghost line to become larger in amplitude and more obtrusive. The simulation also indicated that longer crystals when angularly misaligned produce a ghost line artifact at higher frequency (a deeper ghost line). Using crystal parameters of the 4104 NewFocus modulator in the simulation, the ghost line appears at about 1.7 mm in air, which is the position observed in recorded images (figure 2.2) (850 microns in double pass through air). Results of the simulation that depicts this etalon effect that gives rise to the ghost line artifact are shown in figure 2.3.

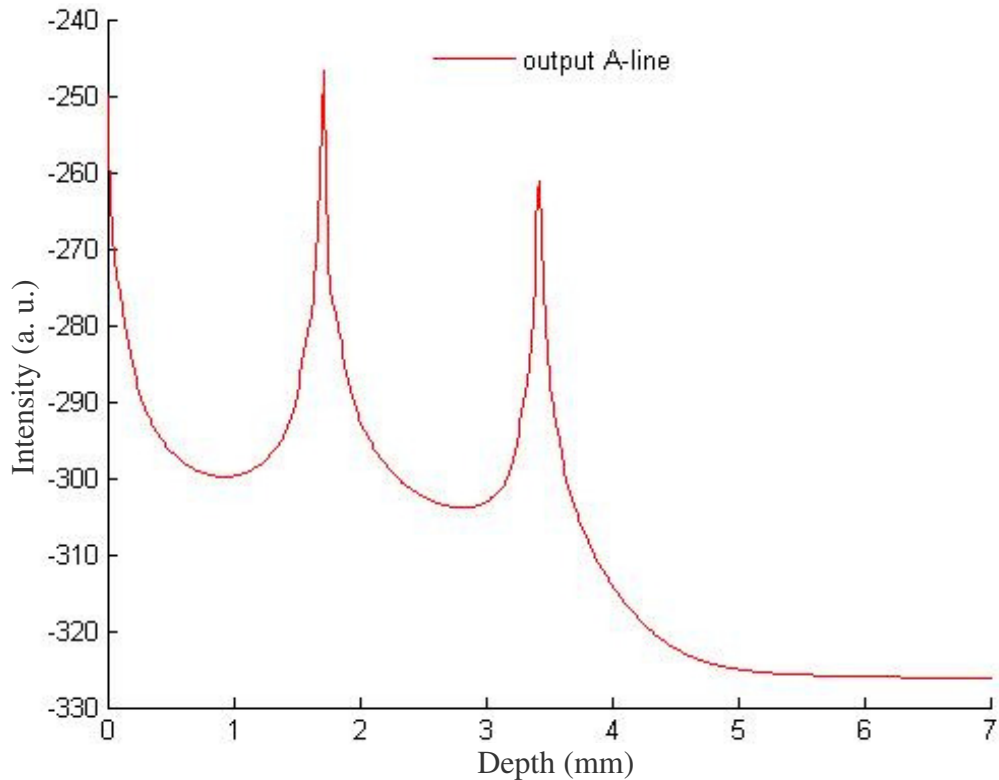


Figure 2.3: Matlab® simulation of the etalon effect caused by the angular misalignment between the two crystals. Ghost lines can be seen at 1.7 mm and at 3.4 mm single pass in air. Intensity of the peaks is in arbitrary units in logarithmic scale

The 4104 NewFocus modulator did not have the means to align the two crystals at exactly 90 degrees, so a mount and adjustment mechanism was designed and constructed. The existing crystal mount was removed and cut in half, and the two parts were then glued to a custom built, stainless steel mount with separate cantilevered tilts. Screws that push against the solid base serve to adjust relative rotation of crystals (figure 2.4). Stainless steel was used for its stiff spring-like metal characteristics and to serve as an electrical ground plane for the crystals. The mount was then glued to the box using conductive epoxy (CW2400, by ITW Chemtronics). Figure 2.5 shows an exploded view of the modulator as a whole.

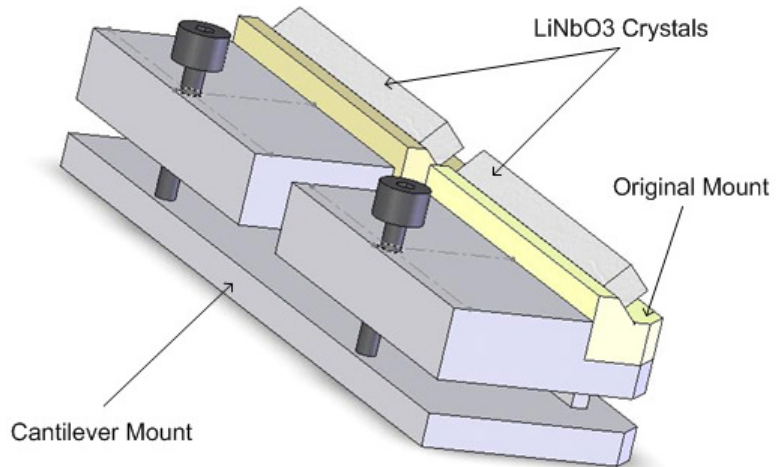


Figure 2.4: Modified modulator tilt mount for precise crystal alignment. Independent cantilevers allow relative rotation of crystals. The original mount (in gold) was divided at the middle and attached to the cantilever mount, maintaining gold electrodes epoxied to the original mount.

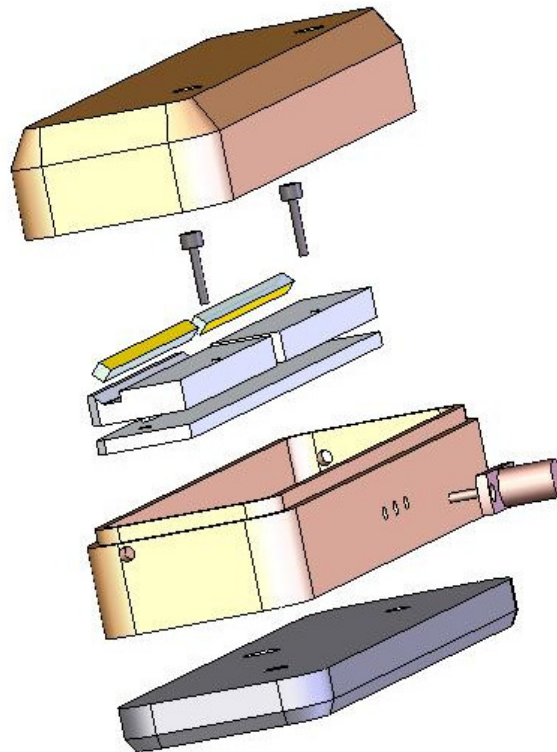


Figure 2.5: Exploded view of the modified polarization modulator showing the crystals on the modified mount, modulator box and SMA connector.

A-line profile was monitored while making angular adjustments to the modulator crystals. The ghost line amplitude could be reduced to the noise floor as one of the crystals was rotated. Figure 2.6 shows a strong peak at about 8.4 MHz before angular adjustment, which corresponds to a double pass depth of 850 μ m or a single pass depth of 1.7mm. The other peaks are due to fixed pattern noise. Figure 2.7 shows that the peak was reduced to the noise floor after optimal angular alignment of the two crystals. However, when the modulator was placed in the SS-PSOCT system, the ghost line peak was not completely removed. A faint ghost line would still be observed in the SS-PS-OCT system, which has a higher measurement sensitivity than the instrumentation used when aligning the modulator.

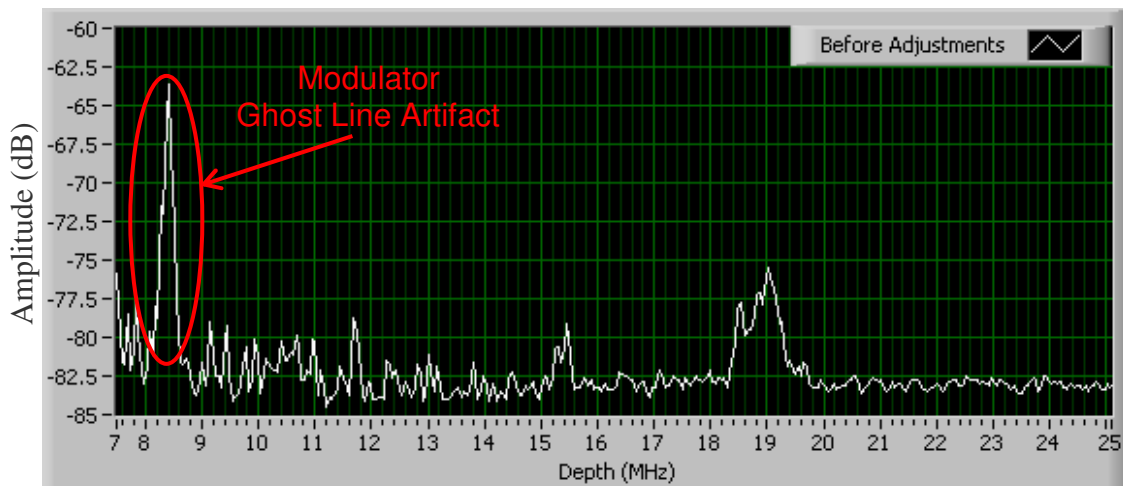


Figure 2.6: FFT of interference signal from modulator before modulator modification. A significant ghost line appears at about 8.5 MHz. The ghost line is due to the angular misalignment between the two crystals.

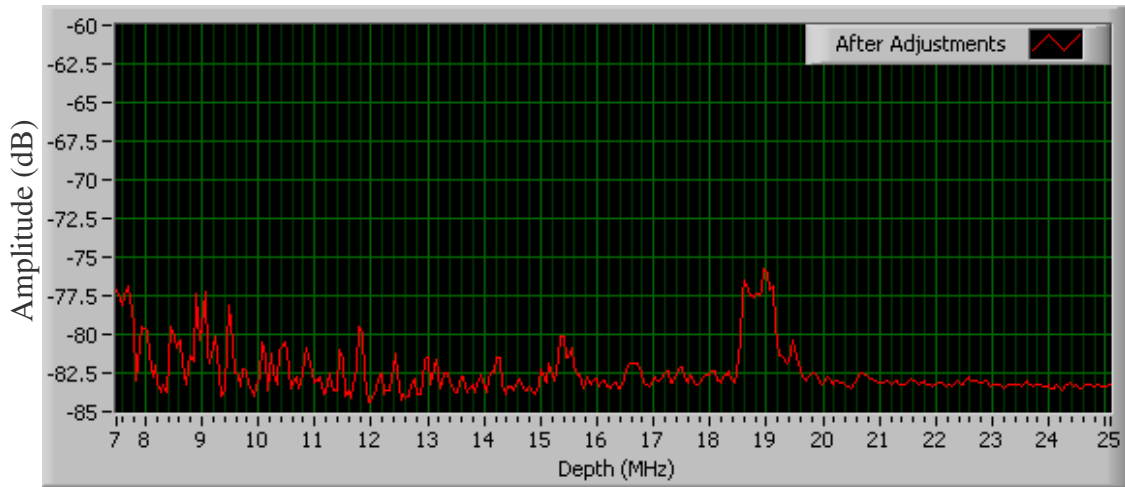


Figure 2.7: FFT of interference signal from modulator after fine angular adjustment of the two crystals. Amplitude of the 8.5MHz line appears significantly reduced.

Figure 2.8 is a polarization diverse intensity image of a healthy volunteer's retina acquired in a circular pattern about the ONH. Recorded image shows high SNR, good resolution, and good penetration depth. The ghost line artifact due to the modulator is extremely faint and no longer visible at the brightness and contrast settings of the image.

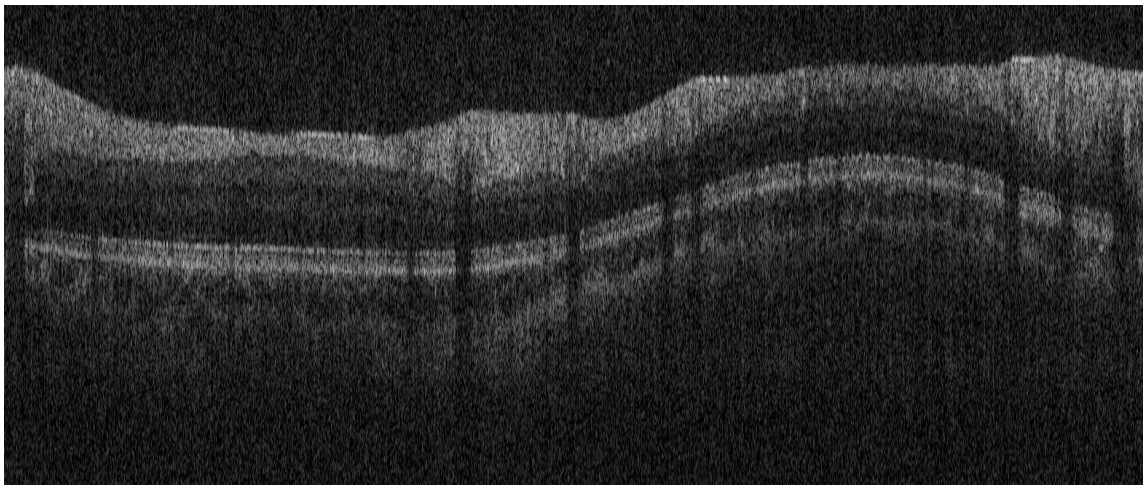


Figure 2.8: A polarization diverse intensity image of a circular retinal scan about the ONH of a healthy volunteer's retina

2.3.4 Long-Crystal Phase Modulator

As discussed in the previous section, optical systems incorporating tunable lasers or broadband light sources can suffer from unwanted interference artifacts produced by the polarization modulator. Eliminating unwanted interference effects is critical to the successful operation of an optical interferometric system because image field of view and SNR may be decreased. Other OCT research groups have tried to correct for the effect of the undesired ghost lines by subtracting these features from images. In these cases, an extra path was added to the interferometer for phase calibration to correctly subtract the ghost line. Though this method can partially reduce the ghost line, lost light is not recovered and residual artifacts can remain. Unlike any commercially available modulator, our modified electro-optic modulator controls phase polarization and the angular alignment of two crystals to minimize unwanted interference effects. All components of this novel modulator are commercially available and the system can be constructed at a reasonable cost.

A second phase modulator was constructed that is similar in design to the one described above with few exceptions. The modulator is described in detail in the provisional patent application entitled “Electro-Optic Modulator for Optical Systems Incorporating Broadband or Tunable Laser Sources” filed on April 2, 2009. The second modulator design had two differences from the first design. The first difference was the use of 50mm long crystals rather than 20mm to effectively remove the ghost line if present to positions 2.5 times deeper than in modulator described above ($2.5 * 0.850 \text{ mm} = 2.125 \text{ mm}$). The modulator can as a consequence provide full 2π modulation for sources at 850nm, 1060nm, and 1310nm with relatively lower voltages unlike the modified modulator of the previous design which can only provide $2\pi/3$ modulation at 1060nm and only $\pi/2$ at 1310nm. The second difference is that the second polarization

modulator design has a superior crystals' mechanical mount for precise angular alignment (figure 2.9). Both modulator designs provide precise alignment control, and minimize interference.

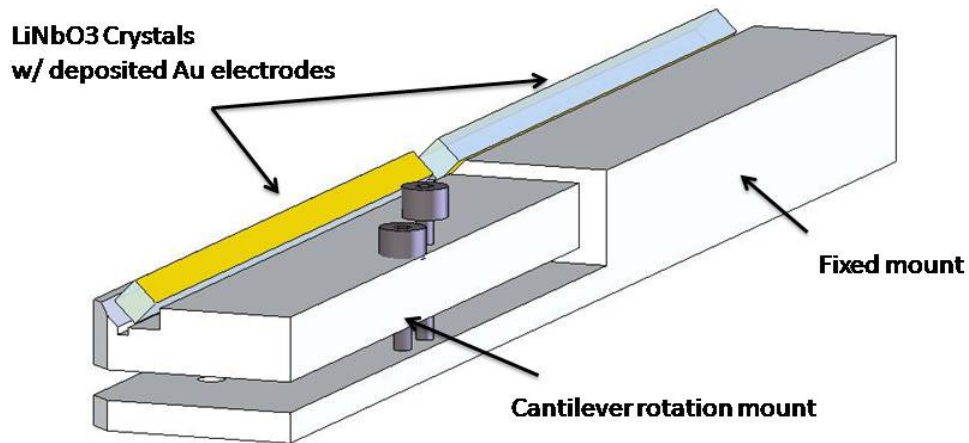


Figure 2.9: Long-Crystal modulator tilt mount with cantilever for precise crystal angular alignment. Two screws provide a push pull mechanism for crystals relative rotation. One screw is threaded to the cantilever mount; the second screw is threaded to the base of the mount.

Measured polarimetric extinction ratio of the second modulator design did not exceed 13, and the throughput was close to 94%. The reason for the relatively low extinction ratio was investigated and it was concluded that the Rayleigh range of the Gaussian beam traversing the modulator should be at least 360 mm for which the beam spot size could not be less than 250 μ m. In the case of the first modulator the beam spot size was less than 180 μ m and the extinction ratio was 117, or 9 times better than the extinction ratio on the second modulator design. Therefore to have high extinction ratio light beam traveling through the modulator needs to have the smallest beam spot size possible. Gaussian beam diameter should be as small as possible to assure light is tightly confined about the optic axis and thus gets the same phase retardation across the spectrum, and for both crystals to eliminate native birefringence. Since a high extinction

ratio is desired to minimize polarization cross talk and record birefringence measurements with low uncertainty this second modulator approach was not used for the patient measurements. The first modulator (using 20 mm long crystals) was able to provide $\pm 2\pi/3$ phase retardation and give maximum separation between the states in a great circle and was therefore used for all measurements reported in chapter 5. 30mm long crystals would be optimal for the electro-optic modulator since achieving the full $\pm 2\pi$ phase retardation is possible and a high extinction ratio can be obtained.

2.4 POLARIMETRIC DETECTION AND DATA ACQUISITION

2.4.1 Signal Acquisition

2.4.1.1 Hardware Description

Instrument timing and triggering are motivated by the repetition rate of the swept laser source. About 2% (after splitting ratios and insertion losses) of the output laser power reaches the trigger photoreceiver. The rising edge of the sweep is detected using a comparator (Intersil ISL84554LPZ). The comparator level is adjustable using a 20 turn trim pot (Bourns 3266). A delay is then generated using a programmable delay counter-timer with oscillator (74HCT5555) to generate the primary trigger pulse that transitions from just after the start of the laser sweep to right before the end. The swept laser source repetition rate is 34 KHz with a duty cycle of 0.64 which corresponds to sweep duration of 18.8 μ sec and the primary pulse trigger is about 17.6 μ sec in duration.

The lateral position of the SS-PSOCT sample beam is controlled by two single-axis galvanometers (Cambridge Technologies, Billerica, MA). A third galvanometer is

used to laterally scan the LSLO beam (LSLO, by PSI Corp.). Voltage waveforms for the three galvanometers' servo drivers are stored a priori in a PCI-e D/A board (NI-6259 by National Instruments, Austin, TX). The A-scan trigger event serves to output desired voltage values to the galvanometers' servo drivers during each trigger event. Galvanometer drivers maintain a closed-loop feedback system which maintains a linear relationship between applied voltage and angular displacement of the mirrors.

A second D/A PCI board (NI-6221) outputs stored voltage waveform to the high voltage amplifier (3211, by NewFocus) that drives the electro optic phase modulator. The phase modulator is controlled using a separate A/D board since the phase modulator requires a different clock rate from that needed for the galvanometers and each board is only able to provide a single clock signal. In response to each trigger event, the D/A board outputs a single voltage value per scanner, whereas for the high voltage amplifier a fixed length train of voltage values is output. The array of voltage values is stored in the D/A card memory and is repeated every three laser sweeps. Figure 2.10 shows the trigger timing diagram and the EOM drive waveform for the three desired polarization states, namely states 0, 1, and 2. State 0 corresponds to $-2\pi/3$ radians (-120°), state 1 corresponds to 0° , and state 2 corresponds to $+2\pi/3$ radians ($+120^\circ$) phase retardation.

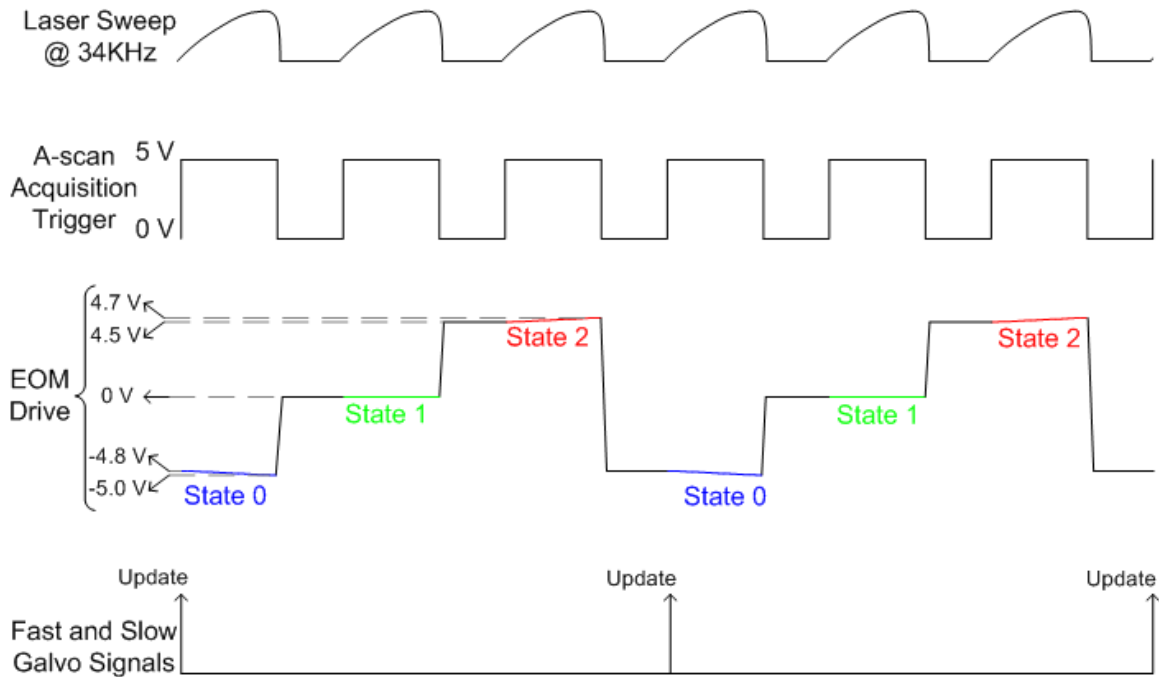


Figure 2.10: Laser sweep, acquisition trigger timing diagram, EOM drive waveform and slow and fast galvanometer signals.

Spectral interference fringes for vertical, $S_V(k)$, and horizontal, $S_H(k)$, polarization channels are detected using two balanced photoreceivers (model 1811 by NewFocus, Chino, CA). One balanced photoreceiver is used for each of the two channels. Acquisition is started using the global trigger as the narrowband swept-laser source is activated [51-54]. The number of samples per sweep is determined by the clock. Interference fringe intensities are uniformly clocked in the k -space domain and digitized with a 16-bit PCI-e A/D converter (ATS9462 by AlazarTech, Toronto, Canada). Acquisition is controlled using National Instruments LabView 8.6 Virtual Instrument (VI) software running on an Intel core2 processor Q9550 (2.83GHz, 1333 FSB) Dell XPS 730 workstation with Quad Core Technology and 12MB cache with 4 GB of RAM. A diagram of electronic instrumentation for acquiring SS-PSOCT and LSLO information is detailed in figure 2.11.

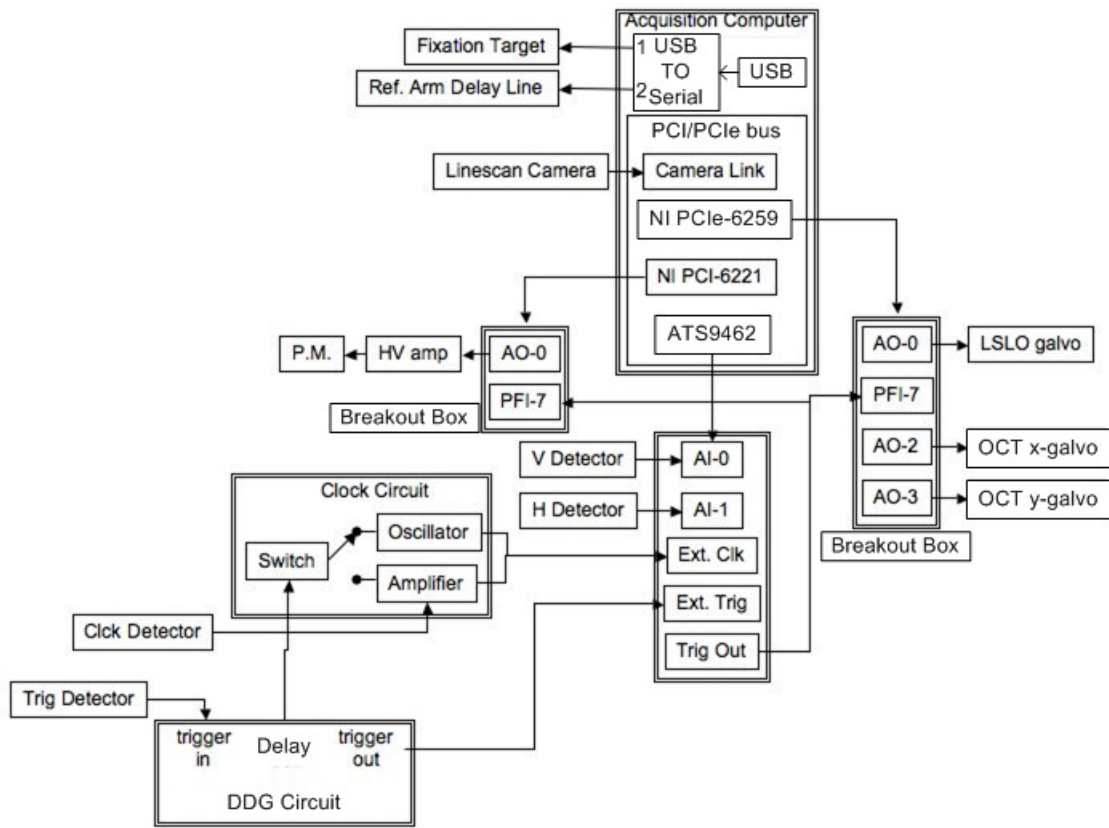


Figure 2.11: Electronic instrumentation diagram for acquiring SS-PSOCT interference fringe intensities and LSLO images

2.4.1.2 Software Description

Acquisition and control software is written primarily using LabView 8.6 (National Instruments, Austin, TX). Software design is that of a client-server approach where three parallel loops are used; one each for acquisition, processing, and display. This multithreading approach is efficient since no independent task is waiting on another task to process and guarantees that all CPU cores are working at any time. Changes to acquisition, scanning, delay line, and modulation are all based on event programming

which allows real-time modification with minor or no interruption to the software's functionality. Raw acquired data is streamed to two first-in first-out (FIFO) buffers (one for horizontal channel and one for vertical channel). In live mode, data is properly segmented, scaled, windowed, and Fast Fourier Transformed (FFT). Scaling, windowing, and FFT are done using IntelC programming primitives (IPP) to insure that these time-intensive tasks are handled efficiently and that the system can achieve real time display of all laser sweeps. Because display of LabView intensity graphs is slow as many graph parameters are rewritten at each refresh of the graph, DirectX was used instead. A separate loop handles LSLO display using National Instruments Vision software. Since the system is polarization sensitive, two OCT channels and the LSLO camera link were handled at the same time and the system was only able to reach a rate of 34 frames per second if every other OCT image was discarded. No data was discarded in acquisition mode since the system memory was large enough (2GB for acquisition software) even though card memory was only 8 MB. Data was sent from the card buffer in 8MB records using asynchronous direct memory access (DMA). The combination of asynchronous DMA access and transfer of large chunks of data (8 MB) kept latency and handshaking time small. Writing of data from memory to hard disk is slow and can constitute a data flow bottleneck so even though we are de-queuing from RAM as we stream to hard disk if acquisition was to proceed continuously the buffers can eventually overflow, however, we have not encountered this problem to date.

To achieve real-time processing, GPU processing was temporarily used for FFT calculations instead of IPP. A test harness showed that for a 1024 point intensity based SS-PSOCT system, real time processing can be achieved at 280 kHz based on an available off-the-shelf and easy to program GPU (NVIDIA GeForce 8800 GT). All results shown in chapter 5 were acquired using FFT from IPP.

2.4.2 External clocking

Images of biological samples are reconstructed by computing an inverse fast Fourier transform. The Fast Fourier Transform (FFT) is used to provide optimal processing speed. Computing the FFT assumes equally-spaced samples in the optical frequency or k-space domain (optical frequency of detected signal in OCT) to accurately represent the OCT signal in time or spatial domains respectively. Non-uniform sampling in k-space distorts and widens the system response function as reconstructed by the FFT, which results in a significant degradation of image resolution with increasing depth.

Sweep non-linearity in our swept laser source can be observed in fringes generated at the clock MZI. We acquired the signal with a uniform clock sampling rate built into the A/D converter then computed the Hilbert transform to extract the analytic phase signal. Derivative of the analytic phase gives the angular frequency of the interference fringes. The linear part of the derivative was subtracted to isolate non-linearity in laser frequency. For a 22MHz center frequency one would observe a 3 MHz variation across the spectrum (Figure 2.12). A 22 MHz fringe frequency corresponds to a pathlength difference of 5.4 mm in air single pass or 2.7 mm double pass which is the desired maximum imaging depth for our system. Since imaging depth scales linearly with frequency, the effect is more dramatic at higher frequencies (deeper depths). At 2.7mm imaging depth the total linewidth is 600 μ m and at 800 μ m depth linewidth is about 175 μ m while the theoretical axial resolution based on the source characteristics should be less than 20 μ m.

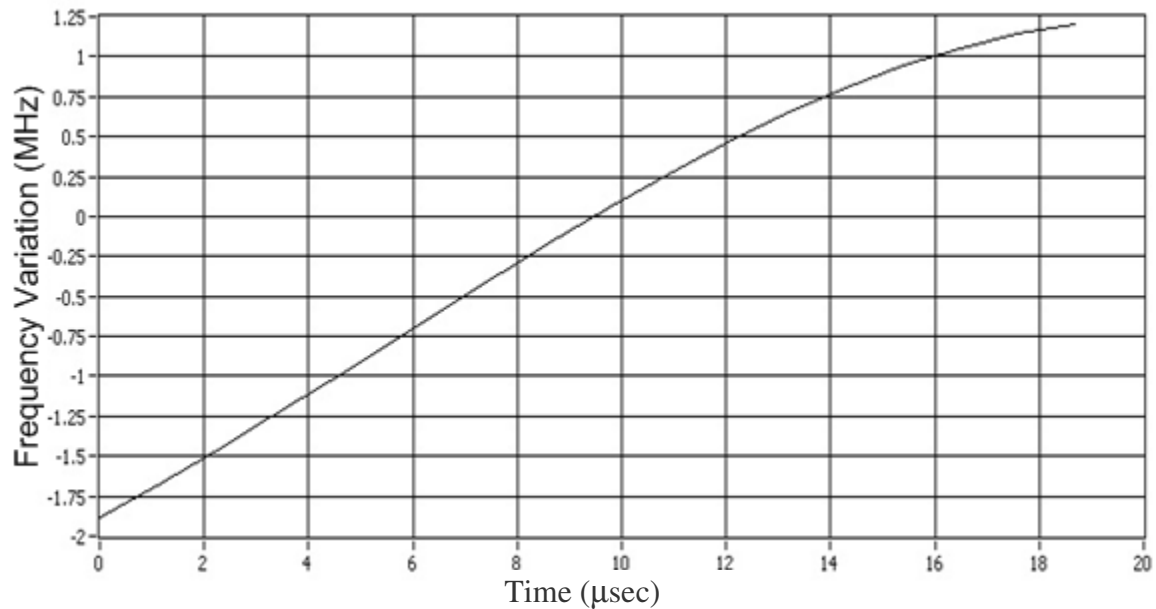


Figure 2.12: Plot of time variation in clock frequency due to non-linear laser output in k-space. Non-linearity gives rise to degradation in image quality when using a linear acquisition clock.

Typical methods to correct for sweep nonlinearity are to either acquire a calibration signal serially or in parallel to use for fringe data re-sampling. Calibration signals may be software or hardware based and can be processed in real-time or after acquisition. All methods aim to correct for the tunable laser non-linear sweep and provide equally spaced samples in optical frequency or k-space domain. Software based methods require post-processing and are unsuitable for clinical imaging since they introduce long time delays and patient data is not directly viewed. Hardware based methods usually require a fiber Bragg grating (FBG), an etalon, or as in our case use of a Mach-Zehnder interferometer (MZI) to provide a uniformly sampled clock in k-space. Using the MZI approach has the advantage and flexibility of choosing the frequency of acquisition since one can easily adjust the MZI pathlength mismatch and hence tune to the desired carrier clock frequency. When using the MZI we were able to demonstrate

two types of real-time k-space clocking approaches. Section 2.2.3 has a complete description of the MZI used in the different clock approaches. One scheme uses a reproduced or ‘cloned’ clock that is acquired serially which we refer to as “Reproduced K-space Clock”. The other clocking scheme uses the real-time clock which we refer to as “Analog K-space Clock”.

2.4.2.1 Reproduced K-space Clock

In this approach we first acquire a reference signal from a single reflection with a fixed optical path length (OPL) mismatch, digitally process the signal, and use an arbitrary function generator (Agilent 33250A) to reproduce the processed clock signal for every laser sweep acquisition. This method worked fine when the system was built on a bench top table since obtaining a reflection from a single surface at the sample arm is straightforward. However, when the system was rebuilt on a cart having a separate real-time clocking interferometer was important and we therefore built a MZI clock. We acquired the MZI signal, then processed in software such that amplitude across the spectrum is uniform with the option of doubling or quadrupling the frequency. We then loaded the modified clock signal to a PCI waveform generator (CG11, by Gage). Using the Gage card allowed us to clock at frequencies up to four times higher than can be provided by the MZI. We were able to clock at 80MHz without a loss in accuracy. This limit was due to the fact that to properly represent a sine wave one would need about 12 samples per cycle, which requires a sampling rate of 960 MS/s, therefore approaching the waveform generator maximum rate of 1 GS/s. To obtain a maximum frequency of 80 MHz one would need to start with a 20MHz clock frequency from the MZI. The lower the MZI frequency the better since the clock fringes’ modulation depth decreases with

increasing frequency. Instantaneous source coherence length is 6 mm and corresponds to decrease of the modulation depth decrease by $1/e$ (about 37%). A 6 mm clock pathlength mismatch corresponds to about 23 MHz clock (slightly less than 1.5 mm imaging field of view). An 80 MHz clock gives an imaging field of view of more than 4mm which is more than necessary for imaging the retina and results in large datasets. A 2-3mm imaging depth is sufficient for retinal imaging and strikes a balance between imaging field of view (FOV) and size of acquired datasets. If a lower frequency clock signal is used (12.5 MHz), and frequency quadrupling is performed resulting in a 50 MHz signal (about 2.6mm imaging depth) then the minimum sampling rate to accurately represent the sine wave is 600 MS/s. The cost of commercially available cards that sample at such fast rates is high. This method still works fine even though it assumes that the source nonlinearity does not vary from scan to scan over extended periods of time. I experimentally confirmed a stable clock operation, by acquiring two clocks three months apart that did not show any difference in measured resolution. Despite utility of this approach, it seems more appropriate to use a clock that does not require software modification and is cheap to implement. All polarimetric measurements of chapter 5 were acquired with a reproduced k-space clock.

2.4.2.2 Analog K-space Clock

Signal from the MZI is transformed to electrical voltage at the balanced detector. Laser duty cycle is 0.64 hence no clock signal is output from the MZI when the laser is not lasing. To accommodate for dead space when laser is not lasing, clock output is switched between the MZI k-space clock and a 27 MHz fixed oscillator to present a consistent clock signal at the A/D clock input. Switching between clock and oscillator is

timed with the rising and falling edges of the global trigger signal (figure 2.10). The circuit switches from k-space clock to fixed oscillator at the falling edge and then back from oscillator to k-space clock at the rising edge. The clock signal is low-pass filtered then converted to a TTL pulse train using a high speed comparator before being connected to the digitizer external clock input. Extra caution is exercised to ensure that the number of acquired signal samples does not extend beyond the laser sweep into the oscillator sweep, which would degrade image resolution. The swept source laser has a coherence length limited to 6 mm (23 MHz maximum clock frequency) and as such this clocking method is limited to 25-30 MHz before the circuit (which relies on zero crossings) starts missing clock cycles.

The necessity of a real time clock system that would generate a clock signal linear in k-space and is representative of laser nonlinearity at every sweep is established. Clocking at frequencies higher than the limitations exhibited by the clock described in the previous chapter is desirable and sometimes necessary. As such, we developed the same concept of clock doubling or quadrupling discussed in section 2.4.2.1 except analog circuitry was utilized instead of software. Because the MZI fringe signal is best at lower frequencies, we set the MZI to generate a clocking signal of about 12.5 MHz maximum (actual signal varies from about 11MHz to 12.5MHz). This signal quadrupled yields a clock signal that is linear in k-space domain with 50 MHz maximum frequency. A nominal frequency oscillator clock needs to be introduced in the dead space region of the MZI generated signal so that a persistent sampling clock is presented to the acquisition board. This requires switching between the quadrupled clock and oscillator. This switching is timed with the trigger signal generated from timing the off period in laser duty cycle. Quadrupling was based on the principle of rectification. Full wave

rectification happens in real time and works independent of frequency (if proper fast switching diodes are used).

Full wave rectification of a $\sin(\omega)$ wave yields a main component at $\sin(2\omega)$ and other components like $\sin(\omega)$ and $\cos(\omega)$. To obtain $\sin(4\omega)$, we band-pass $\sin(2\omega)$ to filter out all the other components, then rectify the resultant signal again and band pass $\sin(4\omega)$. Figure 2.13 shows the block diagram of the circuitry used for analog quadrupling of the k-space clock signal from the MZI [55].

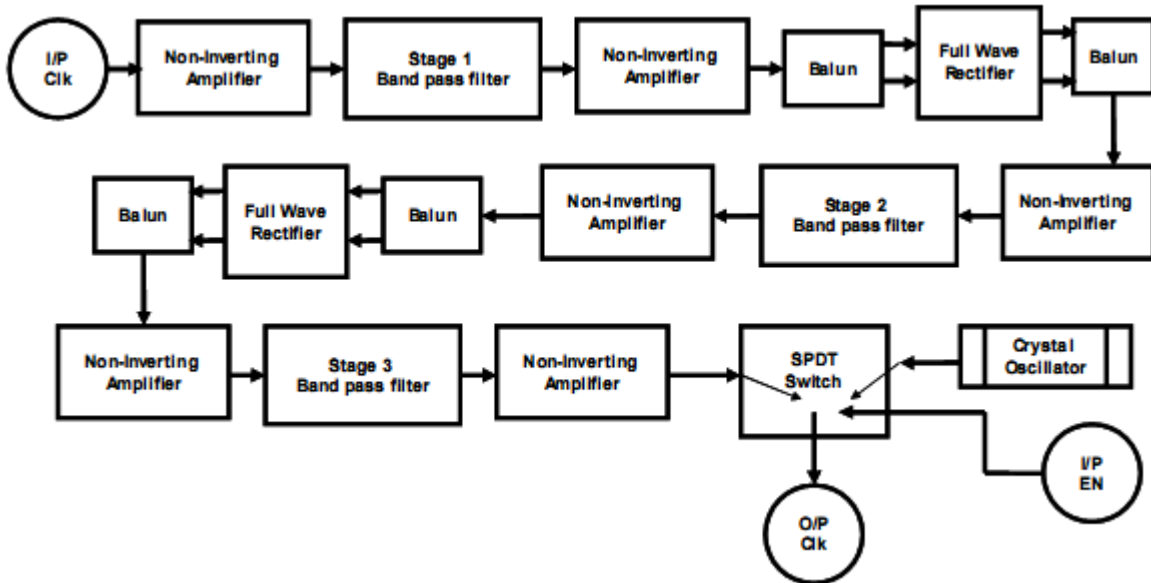


Figure 2.13: Block diagram of the analog quadrupled k-space clock [55].

2.4.2.3 Different Clock Schemes Performance Evaluation:

To compare different clocking schemes the left eye of a healthy volunteer (25 years old male) was imaged. Images were acquired as ring scans about the optic nerve head. Each ring scan image consists of 720 A-scans and is 7.35 mm in circumference. Images were acquired within few seconds of each other. At first the image was acquired

with a 50 MHz internal clock (figure 2.14) to show the dramatic effect on resolution and SNR degradation when the laser non-linearity is not corrected. Second, the same ring scan image was acquired for the same subject while the subject remained fixated on the same target while the software processed quadrupled clock was used (figure 2.15). Maximum image depth was calculated at 2.6mm. Using the same MZI used for the software quadrupled clock we switched to the analog quadrupled clock (figure 2.16). All parameters were identical except the number of acquisition points per laser sweep changed. In both cases we tried to maximize number of points per acquisition to maximize image quality. In case of the analog quadrupled clock, measured scan depth in air was about 3.2mm which is about a 23% increase over the software quadrupled clock. Decreased imaging depth in the software quadrupling approach was due to imperfect quadrupling. Also, the analog clock provides an apparent improvement in axial resolution (image appears sharper), greater signal to noise ratio (image of the retina appears brighter with the same brightness and contrast settings), and deeper image penetration depth.

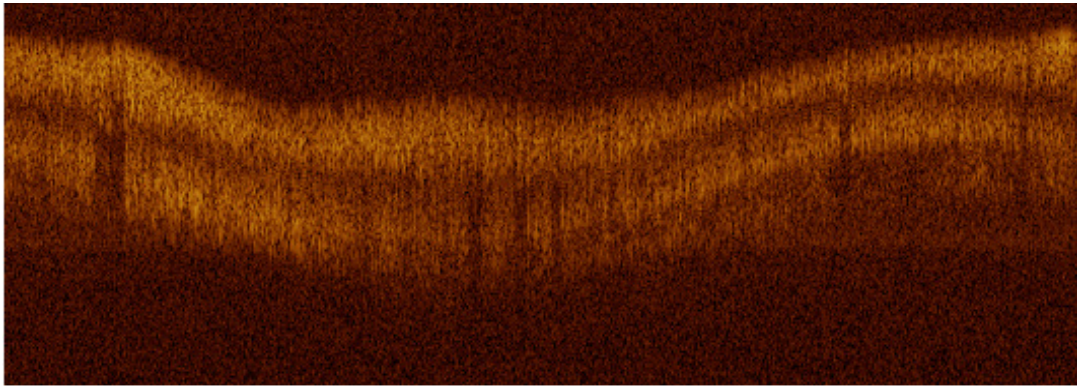


Figure 2.14: A ring scan image of a healthy volunteer acquired about the optic nerve head with a 50 MHz time uniform clock.

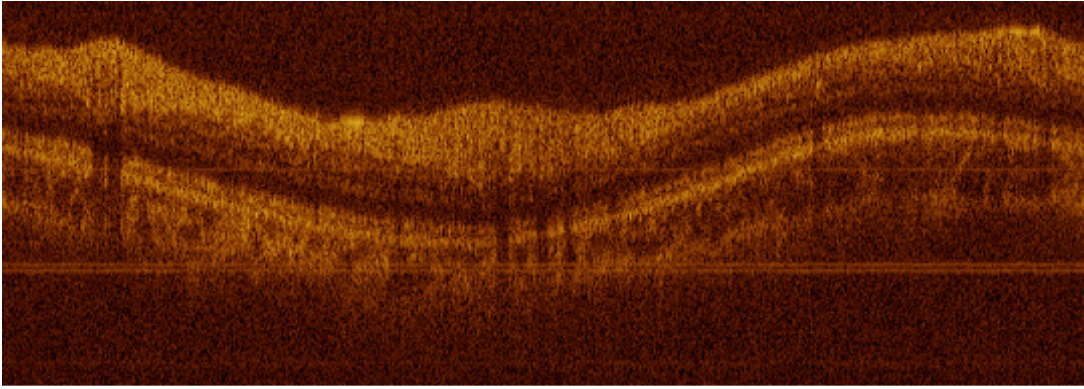


Figure 2.15: A ring scan image of the same healthy volunteer acquired about the optic nerve head with software quadrupled reproduced k-space clock.

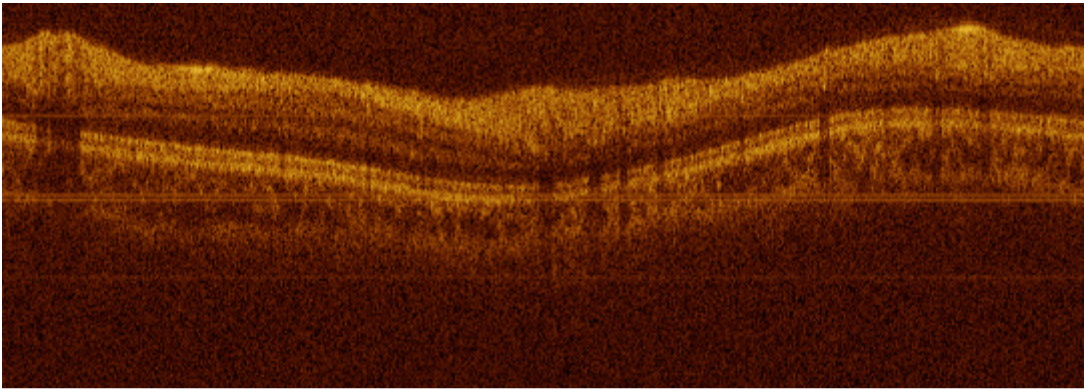


Figure 2.16: A ring scan image of the same healthy volunteer acquired about the optic nerve head with analog quadrupled k-space clock

Since images are not necessarily acquired at the same retinal location we decided to complete a more quantitative comparison between the two clocks. In this case we imaged a silver coated mirror and computed signal to noise ratio (SNR) and longitudinal axial resolution (PSF). The aim of these measurements was not to determine system absolute minimum resolution and sensitivity but rather compare the two clocking schemes. SNR and PSF measurements were obtained at various imaging depths from 0.2mm to 2mm by moving the reference arm while keeping the sample arm fixed. For the analog quadrupled clock we performed measurements twice. First, with the maximum number of samples per acquisition (776) and then with 656 samples per

acquisition to match the maximum number of acquisitions we record when using the software quadrupled clock. Results for SNR and PSF are shown in tables 2.1.

Table 2.1: SNR and PSF comparison at various depths between analog quadrupled and software quadrupled clocks

Depth (mm)	Hardware Quadrupled				Software Quadrupled	
	776 Samples/Sweep		656 Samples/Sweep		656 Samples/Sweep	
	SNR	PSF	SNR	PSF	SNR	PSF
0.2	26.3	17.8	25.8	18.7	25.2	20.4
0.5	25.8	17.1	24.7	18.3	23.8	21.3
0.8	23.5	17.4	22.9	18.4	22.1	21.6
1.1	21.6	16.5	21.2	17.9	19.6	23.4
1.4	19.5	17.1	19.2	18.2	17.4	24.8
1.7	18.3	16.4	17.1	18	15.1	26
2.0	16.8	17.1	16	18.5	13.5	27
Mean	21.7	17.1	21	18.3	19.5	23.5
Slope	-5.3dB/mm	No Drop	-5.4dB/mm	No Drop	-6.5dB/mm	-2.7μm/mm

As evident from table 2.1 the analog quadrupled clock provides superior SNR and PSF compared to the software quadrupled clock (although both perform well). Compared to published work, I believe that the analog quadrupled clock provides the lowest SNR degradation with increasing depth. Also, no degradation in resolution was observed for the analog quadrupled clock whereas PSF degradation with depth for the software quadrupled clock was less and better than interpolation approaches.

2.4.3 Operation of the SS-PS-OCT System

The system was operated in two modes depending on type of measurement performed. When polarimetric information was not necessary then the system operated in balanced detection mode. Whenever polarization sensitive measurements were recorded (all polarization data presented in Chapters 4 and 5), the system operated in single-sided mode whenever polarization sensitive measurements were required.

To accurately measure sample birefringence, reference horizontal and vertical light needs to have equal amplitude across the optical spectrum for all input polarization states at the detection arm (chapter 4). We attempted to balance H and V channels across the spectrum for all three incident polarization states for the two detection arms. We were able to balance one arm properly. We used a polarization controller at the reference arm and makeshift polarization controllers to balance ($V = H$) for the three polarization states ($-120^\circ, 0^\circ, +120^\circ$) for both detection arms.

The polarization controller in the reference arm is the large paddle type (FPC560 by Thorlabs). The controller transformed and polarization state of light from any arbitrary input state to any arbitrary state at the output. Since the longest fiber segment in the reference arm was only 1m long, we were only able to have one fiber loop per paddle. The reason why we used the large paddle type polarization controller and short fiber segments is explained in detail in Appendix A. To control the polarization state of light at the detection arm, we used a makeshift polarization controller composed of fiber wrapped around a 1/2" steel post.

The use of makeshift polarization controllers was necessary since detection arm fiber segments were short (0.6m each). Each makeshift polarization controller consists of a regular half-inch diameter steel post mounted on the optics tray. The H/V ratio was actively monitored during the polarization adjustment process that involved adjustment to the reference arm polarization controller in conjunction with careful looping and twisting of the first detection arm fiber about the post that effectively acts as a polarization controller. We were able to equalize H and V for all three states across the spectrum for the first detection arm; however, we could not equalize H and V for the second detection arm since reference arm and detection arm adjustments are coupled. To align the second

arm would require further adjustment of the reference arm polarization controller which would in turn misalign the first detection arm.

With the actual polarization adjustments we were able to make the ratio of V over H in the good arm (first arm) nearly uniform across spectrum. We had to attenuate coupling back into fiber for the H channel until the ratio was almost equal to unity (figure 2.17). Further discussion can be found in Appendix B.

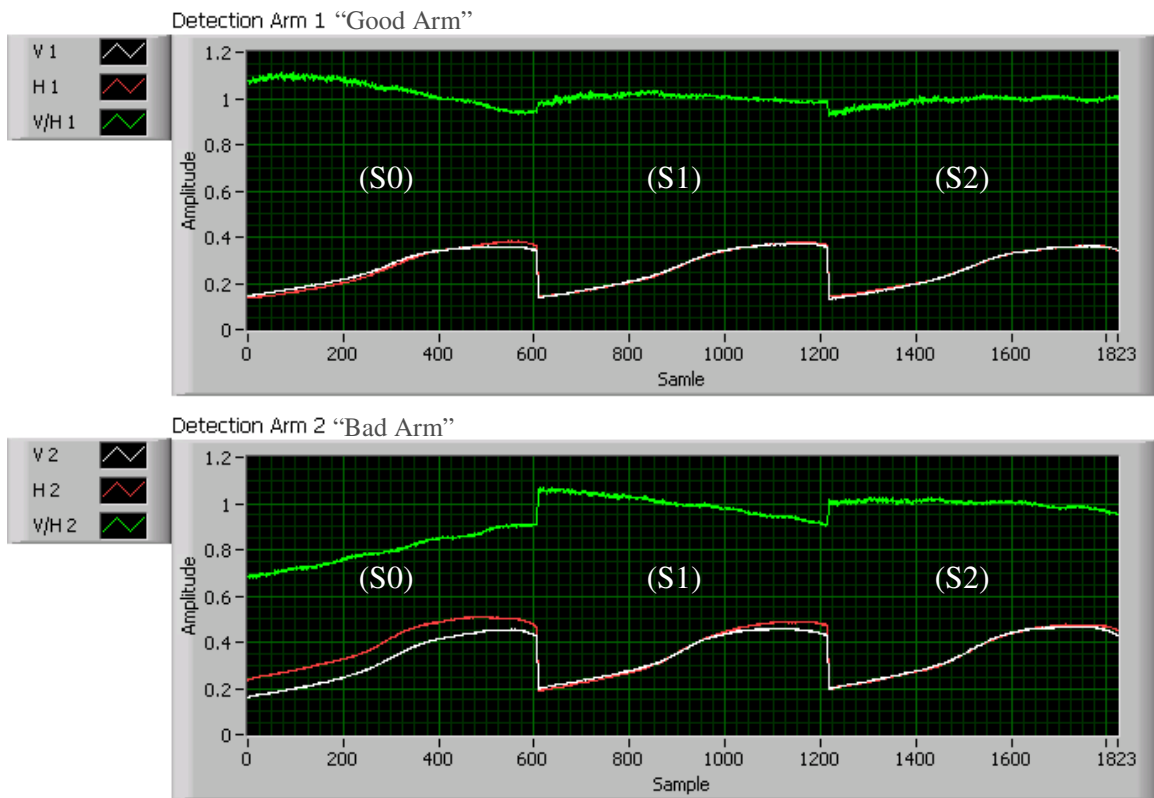


Figure 2.17: Three laser sweeps corresponding to the three polarization states for both arms. The white curve is for the horizontal channel, the red curve is for the vertical channel and the green is the ratio of V over H. (a) Good detection arm (arm 1). (b) Bad detection arm (arm 2). As can be seen the V over H ratio for the good arm is almost one for the whole spectrum for all three states, whereas for the bad arm state 0 is very far from a ratio of one and varies substantially across the spectrum.

Chapter 3: Slit-lamp Based OCT and LSLO Retinal Imaging

3.1 INTRODUCTION

OCT sample arm setups can substantially differ depending on imaging application. For example, imaging human skin requires a simple hand piece that can include a set of galvanometers and focusing lens, whereas imaging the vasculature or luminal organs such as the esophagus can require the use of a rotating catheter or endoscope. For imaging the eye of anesthetized animals, instrumentation including galvanometers, an afocal triplet lens pair, and a focusing lens has been applied for imaging anterior parts of the eye. The focusing lens is not necessary for imaging the posterior eye since the cornea and lens provide the necessary power. Imaging of the human eye, however, requires a special interface since anesthesia and surgical manipulations of the eye are not standard of care. Human eyes exhibit involuntary movements known as micro- and macro-saccades. Head movements, cardiac rhythm, and respiratory cycle add to eye movements. All these movements complicate retinal imaging and can cause image degradation. Stable imaging of the eye is therefore critical.

3.2 LSLO/OCT PATIENT INTERFACE

To image a large number of patients with ease and repeatability, we acquired a commercial line scanning laser ophthalmoscope (LSLO, by PSI Corporation). The LSLO system was incorporated with the SS-PSOCT instrumentation into a single system with a shared optical interface. The LSLO system consists of two main components. The first component is the electronics control box, and the second is the optical head.

The electronics box was modified to include all electronic connections from the computer to the OCT/LSLO servo drivers for the scanning galvanometers, laser power monitor, and the LSLO superluminescent diode (SLD) (QSDM-830-2, by QPhotonics LLC, Ann Arbor, MI). Manufacturer supplied diodes frequently deteriorated so we added a heat sink and fan to dissipate heat generated in the box. Design of the driver was such that the SLD was always ON whenever power was supplied to the electronics box even when only OCT scanning functionality was needed. To extend the SLD life we installed an ON/OFF switch such that the source is only ON when LSLO imaging is used. We also adjusted SLD current and temperature controls to obtain optimal and stable power output.

The patient interface consists of an optical head mounted through an adapter onto a modified slit lamp (SL-130). The optical head has two optical inputs, one fiber input for the LSLO and the second for OCT. The optical head has galvanometer mirrors and a doublet asphere module. Figure 3.1 shows a ZEMAX layout of the patient interface optics.

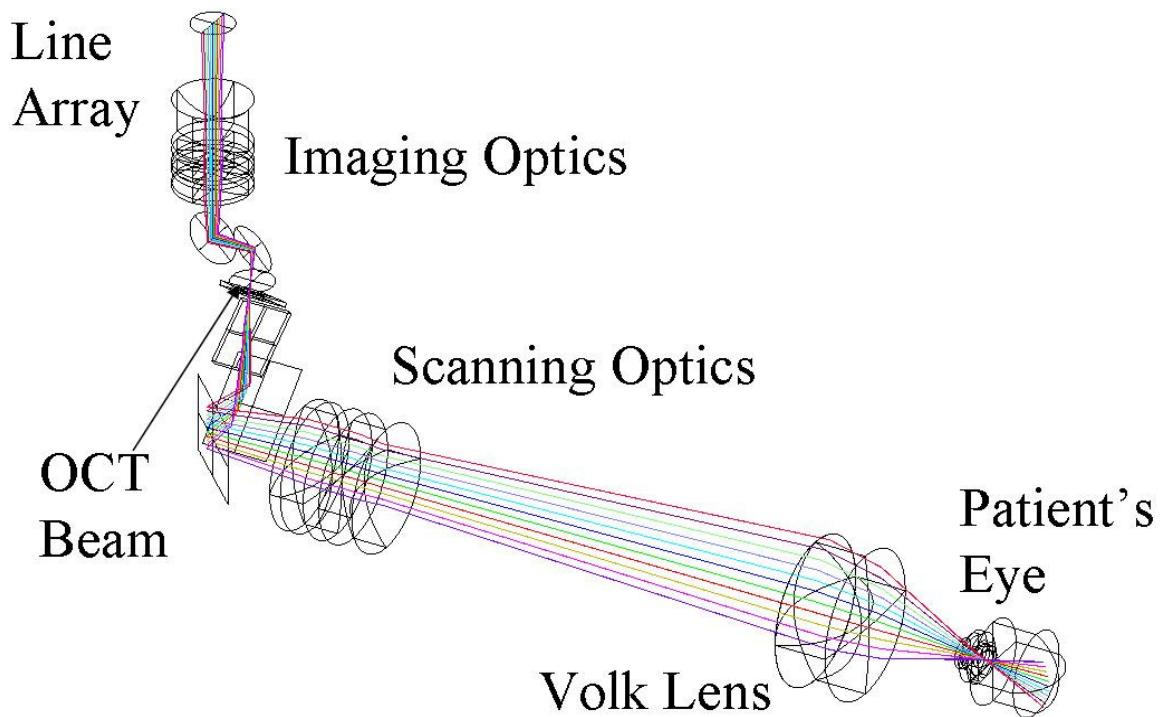


Figure 3.1: ZEMAX model of the optical patient interface module. Model shows propagation of LSLO light from input to the retina and back to the CCD line camera

A slit lamp interface was used since the slit lamp is easily operable is familiar to both ophthalmologists and patients. The slit lamp consists of a chin and head rest that stabilizes the patient's head in order to reduce head motion during measurement. The optical interface can then be moved close to the patient's eye, which allows for easy alignment with the patient. Our setup combines a slit lamp interface with LSLO/SS-PSOCT instrumentation. The LSLO provides a real time fundus image, from which the operator can direct PS-OCT scans to be recorded at precise locations on the retina. The image of a patient's retina as well as the region of interest where PS-OCT scans were performed is stored on file so that when patients are reexamined, the same retinal locations can be scanned again. Comparisons of recorded retinal images and

measurements at the same location over time can accurately track thickness and birefringence changes. The rest of the system is mounted on a portable cart for ease of maneuverability. The mobility, compact size, and familiar interface of the design should allow for the system to be successfully used in clinical studies (Figure 3.2).

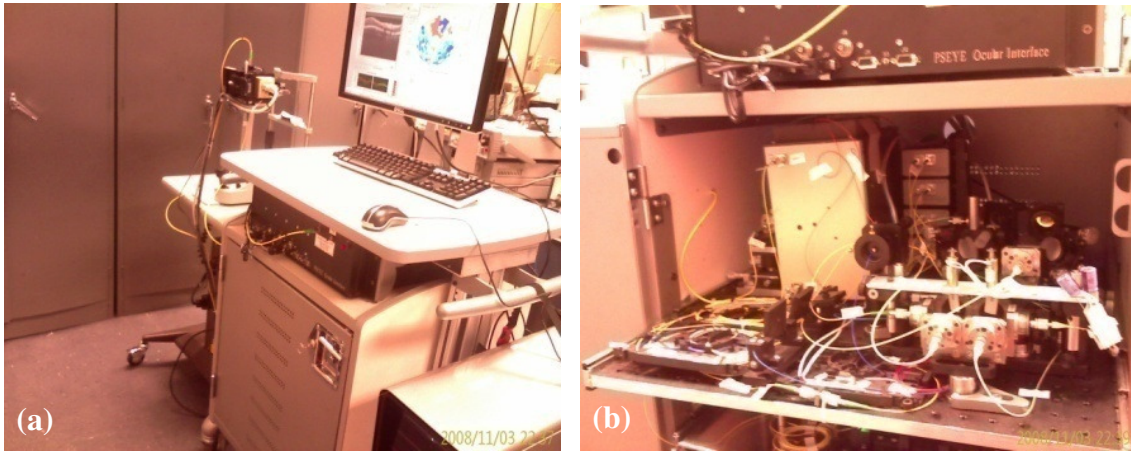


Figure 3.2: (a) The LSLO and the SS-PSOCT system on a cart with the patient interface module placed on a slit lamp. (b): Optics and electronics tray

3.2.1 Hazard Analysis

The instrument consists of a SS-PSOCT system, an LSLO and a patient interface. The instrument is used for imaging the human posterior eye. As use of this instrument involves projecting a laser beam directly into the subject's eye, a conservative retinal hazard analysis was performed.

The OCT portion of the system uses a tunable laser source which sweeps through a range of wavelengths (1020-1100 nm) with 18.8 μ s pulses at a repetition rate of 34 kHz and a peak power at 1076 nm of 6.3 mW. MPE for thermal hazard from a single-pulse of time duration t_{sp} is given by:

$$MPE_{SP} = 9.0 \times t_{sp}^{0.75} \times 10^{-3} = 9.0 \times (18.8 \times 10^{-6})^{0.75} \times 10^{-3} = 2.57 \text{ mJ/cm}^2 \quad (3.1)$$

MPE for thermal hazard from three consecutive pulses, as in the case when polarization sensitive measurements are performed, is given by:

$$MPE_{3P} = 3^{-0.25} \times MPE_{SP} = 3^{-0.25} \times 2.57 \times 10^{-6} = 1.953 \text{ mJ/cm}^2 \quad (3.2)$$

MPE of average power for thermal and photochemical hazard for three pulses with total duration time, t_{3A} , is given by:

$$MPE_{3A} = 9.0 \times t_{3A}^{0.75} \times 10^{-3} = 9.0 \times (56.4 \times 10^{-6})^{0.75} \times 10^{-3} = 5.863 \text{ mJ/cm}^2 \quad (3.3)$$

The most conservative value is 1.953 mJ/cm^2 and hence the peak irradiance is given by:

$$E = \frac{MPE_{3P} \times N}{t} = \frac{1.953 \times 10^{-6} \times 3}{56.4 \times 10^{-6}} = 103.88 \text{ mJ/cm}^2 \quad (3.4)$$

For a 1.5 mm beam diameter the maximum safe power incident on the cornea is given by:

$$P_M = 103.88 \times \pi \times (0.75)^2 = 1.836 \text{ mW} \quad (3.5)$$

The worst case parameter for the LSLO was selected to couple with the SS-PS-OCT for an overall analysis. Analysis of the worst case LSLO beam shows that the peak irradiance on the subject's eye is approximately 7% of MPE and hence when scanning both the LSLO and OCT beams the maximum permissible OCT power incident on the cornea is at least 1.7mW [7].

Experimental measurements were performed by the office of Environmental Health and Safety at the University of Texas at Austin and concluded that the peak irradiance to the subject's eye was below MPE.

To safely operate the system we continuously monitor output laser power (figure 3.3) at the trigger detector output. The trigger detector has two electrical output signals, one is the AC signal, used as the system's global trigger, and the second is the DC signal. The DC signal was acquired using the 6251 DAQ board and calibrated to power incident on the cornea. The one-to-one correspondence between average trigger DC voltage and

measured peak power at the cornea was determined using the 2033 NewFocus photoreceiver and the 1935 calibrated Newport power meter.

All measurement results presented in chapter 5 were acquired with $440\mu\text{W}$ average incident power on the cornea. Maximum power at 1076nm wavelength was 1.14mW, below the MPE for a beam with a 1.5mm spot size incident on the cornea.

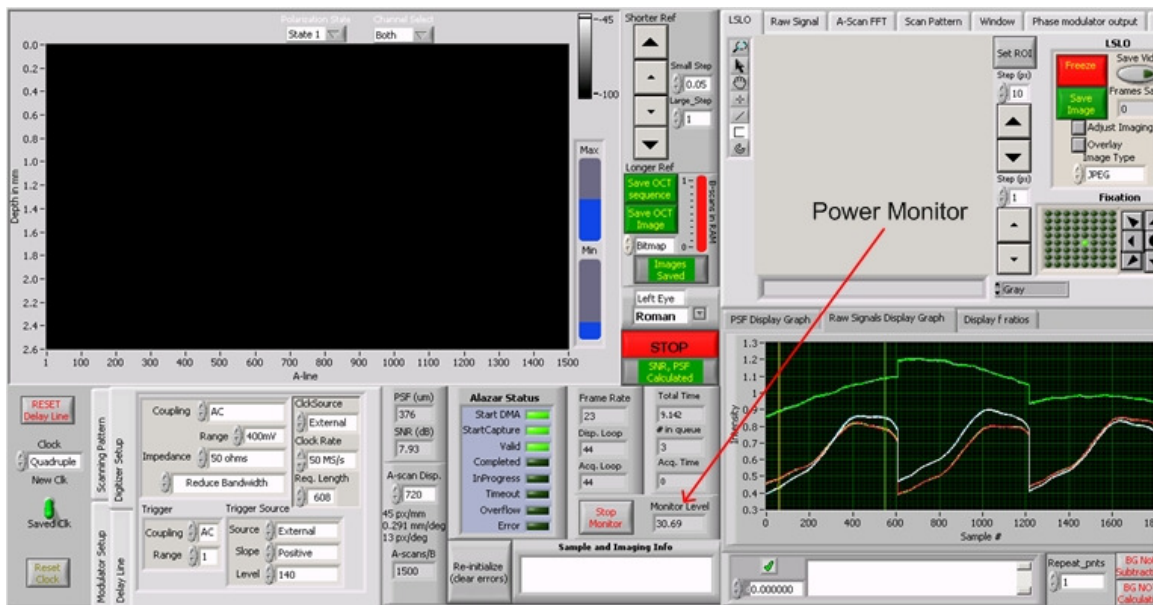


Figure 3.3: Screenshot of the acquisition software showing the monitor voltage

3.2.2 Eye Fixation

To record high quality images of the retinal nerve fiber layer it is necessary to reduce eye movement and to accurately focus light on the retina. The forehead and chin rests of the modified slit-lamp greatly reduce head movement. Even when the head is stable the eye can move in any direction, so a fellow eye fixation module (a set of green LEDs with only one LED ON at a time) was used to further stabilize and fixate the eye and to visualize specific retinal areas of interest. The operator can use the LSLO image

to visualize the ONH and retinal vasculature in real time. Position of the fixation LED can be adjusted until the ONH is in the desired position. Different areas of the retina can be imaged simply by adjusting fixation target position.

The above mentioned fixation scheme suffers from two main drawbacks. Fixation LED size (about 1.8 mm) is too large, and the plane containing the set of LEDs is discrete, making fine adjustments and tight fixation difficult. A second drawback is that a variation exists in the way people's fellow eye tracks relative to the fixated eye. Hence, it was desirable to develop same-eye fixation.

Placing the fixation target anywhere between input light optics and the eye would result in partial obscuring of portions of the retina. To avoid obscuring images we replaced the 45 degree silver coated mirror that reflects light into the final doublet asphere module into the eye with a dichroic mirror that transmits visible light from the fixation LED but reflects near infrared LSLO and PSOCT light. The dichroic mirror was angled at 45 degrees, and the fixation module was placed behind the mirror. The fixation target, dichroic mirror, doublet asphere, and the eye were all collinear. The same eye fixation target was made up of a green-LED with adjustable output radiance. The LED was positioned on a two-axis gimble mount to allow for continuous albeit manual adjustments. The body of the LED was painted black except for a small windowed area to provide a tight fixation target.

Despite the advantages of same eye fixation, the approach was abandoned because the dichroic mirror introduced polarization mode dispersion (PMD) and therefore rendered polarization measurements unreliable. The dichroic mirror also caused a delay between horizontal and vertical light components rendering the point spread function of the system about twice as wide compared to when the silver coated mirror was used.

3.3 HARDWARE DISPERSION BALANCING

Since OCT is an interferometric technique, dispersion balancing between reference and sample arms becomes of paramount importance to ensure good image quality. Several approaches have been used to match dispersion imbalance between reference and sample arms. The most intuitive hardware based approach would be to match materials in the sample and reference arms, which means that fiber lengths in the reference and sample arms should be matched and that any optical elements in the sample arm should be compensated for in the reference with the same optical material and length. However, this method is not practical in the case of human retinal imaging where upwards of 7-10 different glass materials may be present. Another approach is to numerically correct dispersion imbalance in software post processing.

To measure dispersion, a Hilbert transform was used to extract the analytic phase signal. Since the signal was acquired with a linear k-space clock, all nonlinearity in phase was due to a dispersion imbalance. Figure 3.4 shows the residual phase non-linearity due to dispersion. Numerical correction was verified to work but was not implemented, since the correction involved computing a Hilbert transform, subtracting the phase residual shown in Figure 3.4, and then computing the inverse Hilbert transform before computing the FFT. The main drawback of this method, is computation time for the Hilbert transforms that consequently increased processing time considerably, making the numerical approach non viable. Instead, we corrected for dispersion imbalance in hardware while minimizing the number of glass elements (a borosilicate and a flint glass) even though the sample arm contained several glass materials.

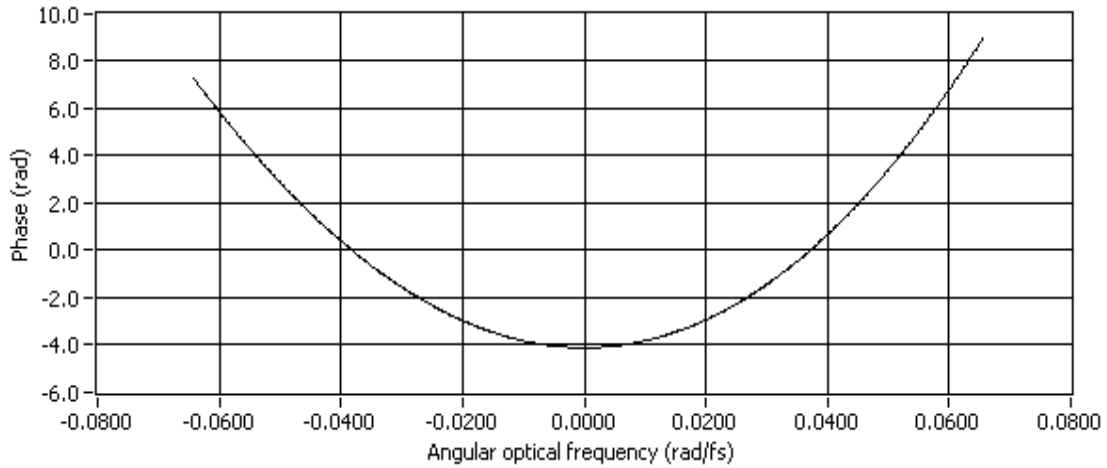


Figure 3.4: Polynomial fit to dispersion imbalance between reference and sample arms over the source spectrum.

3.3.1 Simulation

Three model eyes and LSLO patient interface optics were simulated using ZEMAX. The first model named the “Liou model eye” was based on an eye model created by Liou and Brennan [56]. The Liou model eye includes both a curved surface at the retina and the effect of the cornea on image quality and best simulates the human eye. The second model named the “Cuvette eye model” consists of a plano-spherical lens with a focal length of 38.1 mm and 25.4 mm diameter (KXP079, by Newport Corporation) to provide an approximation of the average cornea and lens power. Behind the lens are two transparent cuvettes (standard 10 mm inner dimension with 1 mm thick walls) fastened together with a portion of the walls shared by the cuvettes trimmed out. The cuvettes are filled with water to approximate the aqueous humor of the eye. A mirror was placed on the outer surface of the cuvette to provide a single reflecting surface. The third model named the “no water model eye” is the “Cuvette eye model” without water in the

cuvettes. The last model is used to confirm that effect of water dispersion is negligible at 1060nm.

A Zemax Programming Language (ZPL) macro was written to compute optical path length (OPL) versus wavelength. OPL vs. wavelength was then converted to phase vs. optical frequencies (ν) (from 273.448 THz (1097.1 nm) to 294.614 THz (1018.28 nm)) and saved to an ASCII text file. Using MATLAB, the ASCII data was fitted to a linear equation to remove group delay. To isolate the nonlinear (NL) section of the phase signal, the linear fit was subtracted from the original signal. This NL part represents dispersion in the system and was plotted vs. angular optical frequency for the three eye models. Also, the maximum dispersion range was tabulated and compared with experimental results. Results are displayed in figure 3.5 and table 3.1 below.

Table 3.1: Total phase variation across the spectrum calculated from the three model eyes. Cuvettes model eyes with and without water in the OPL show that there is no significantly added dispersion due to water.

Modeled Dispersion	Computed Dispersion
Liou model eye	2.21 π radians
Cuvette model eye	1.99 π radians
No Water model eye	1.97 π radians

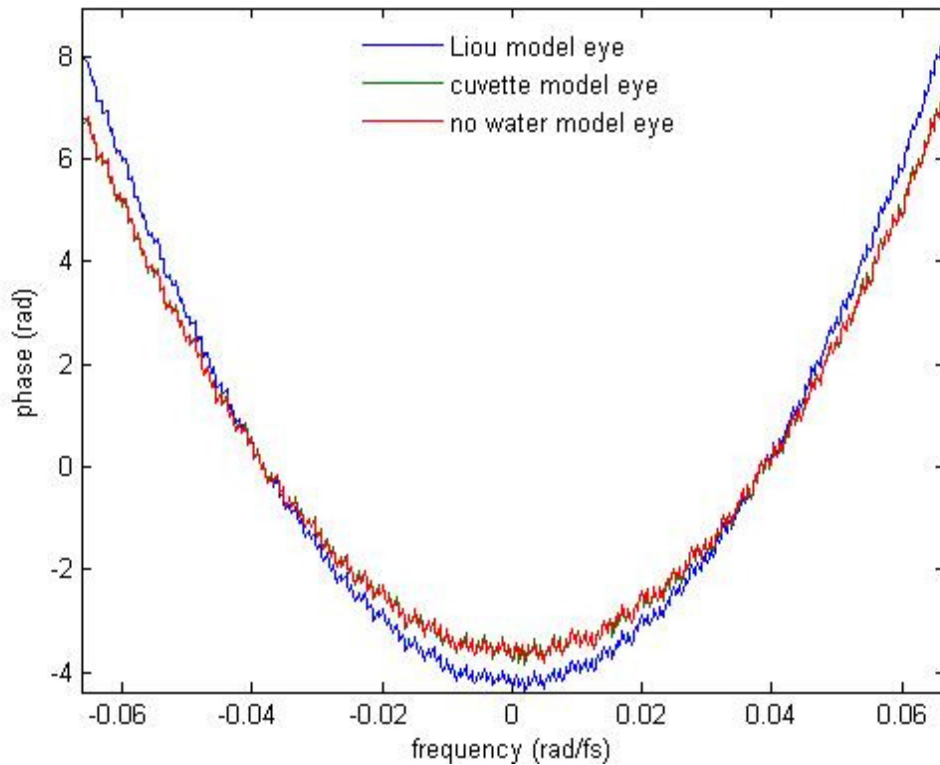


Figure 3.5: Phase delay vs. optical frequency for three model eyes. Addition of water in the cuvette did not significantly alter the dispersion profile which is consistent with 1060nm being a water dispersion minimum

3.3.2 Design

Design specification was to match experimental dispersion mismatch between sample (with Liou model eye) and reference arms. Using a human eye instead of the Liou model eye was not done because measurement was simpler with just a mirror and inter-patient variability could not be accounted for. Differences between the Liou model eye and any human eye is expected to be insignificant at the source wavelength (1060 nm) and therefore no substantial resolution degradation is expected. Using the measured dispersion mismatch profile, the appropriate glass rod to place in the reference arm was

designed. The rod was simulated as a two-element glass composed of flint and borosilicate elements. Flint and borosilicate were chosen because the system optics contains both flint and borosilicate elements. Using the optimization capability of ZEMAX, the choice of flint and borosilicate glass lengths was optimized. Design constraint on the glass rod was to minimize OPL error between the two-element glass and the desired dispersion profile for laser source wavelengths. Few combinations of glass type and length could produce dispersion profiles similar to that sought for. The final choice was the glass combination that maintained highest transmission over the source spectrum and was not too expensive. Figure 3.6 shows the dispersion profile match for the two-element glass rod design (Zemax) and the experimental data.

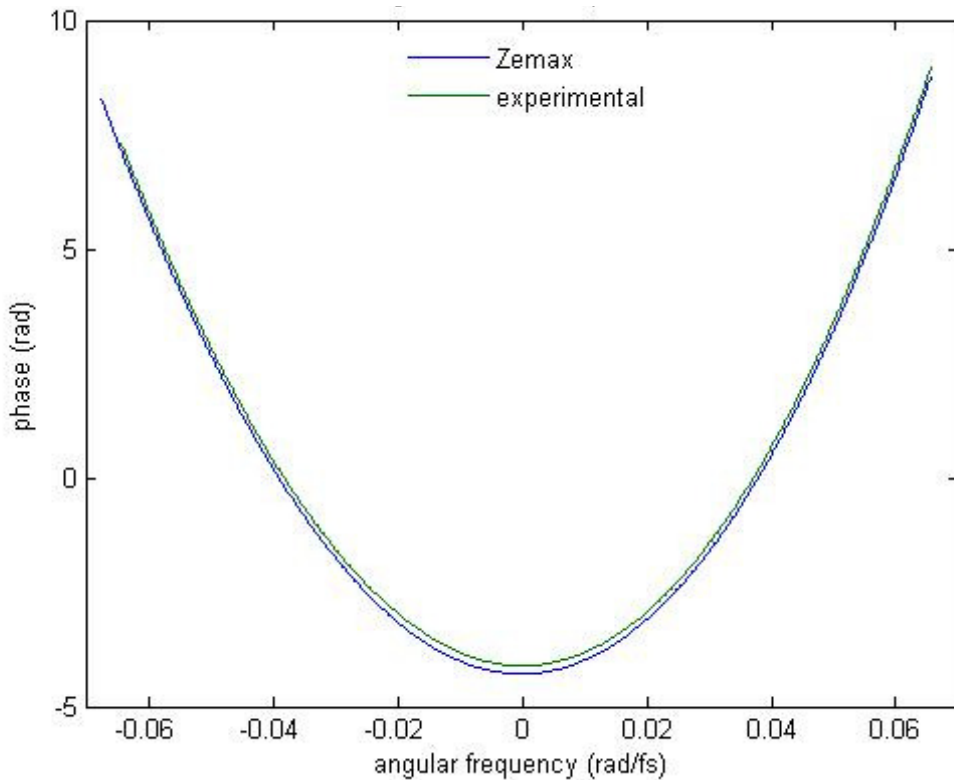


Figure 3.6: Dispersion profiles of Zemax simulated glass rod (Blue) and model eye (Green).

3.3.3 Experimental Verification

A B-scan image of an infrared sensor card (model 5842 by NewFocus) was recorded using identical test conditions first without the glass rod (Figure 3.7a) and then with the glass rod (Figure 3.7b). The recorded images demonstrate substantial improvement in image resolution and an increase in SNR of a few dB after placement of the glass rod in the reference arm. After dispersion balancing, the system point spread function (PSF) closely matched the laser's PSF as will be shown in the next section

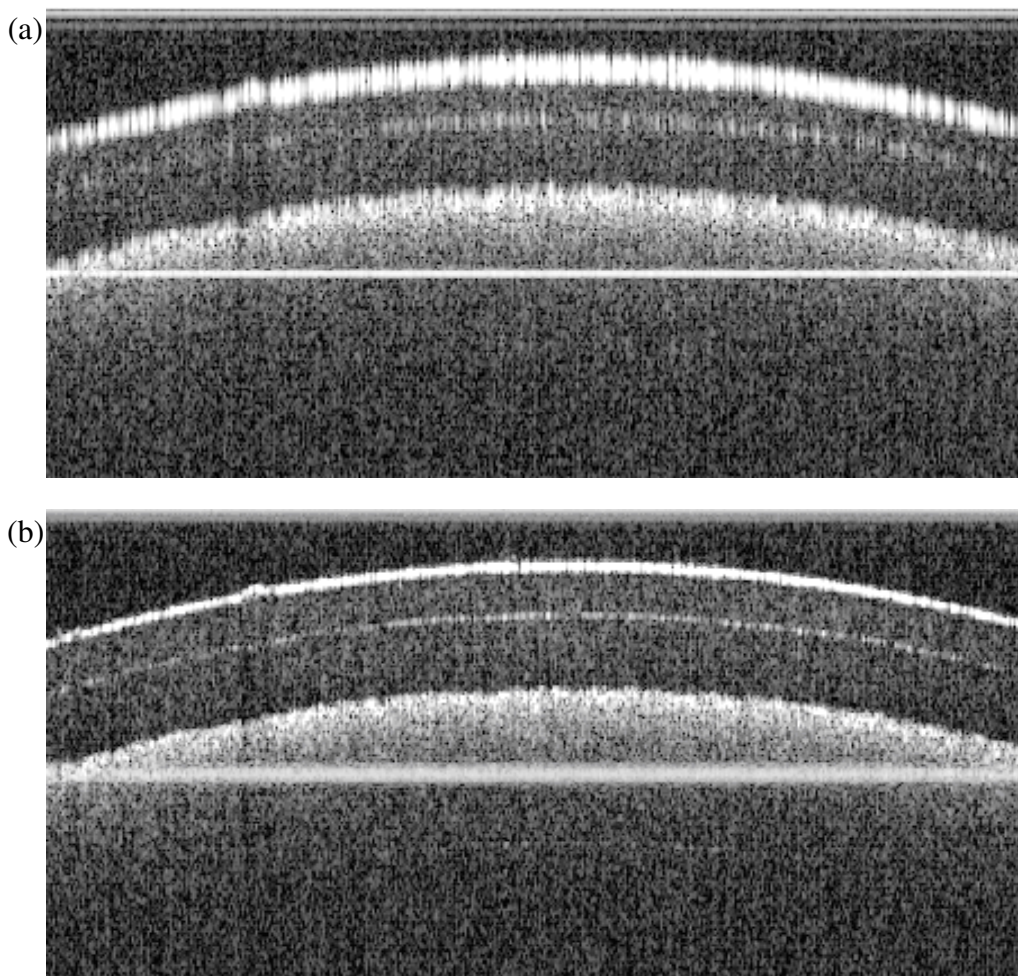


Figure 3.7: OCT image of infrared sensor card. (a) Without dispersion balancing. (b) With dispersion balancing

3.4 AXIAL RESOLUTION AND SENSITIVITY MEASUREMENTS

3.4.1 Axial Resolution

Since the swept source laser spectral profile is not Gaussian (Figure 3.8), we cannot use the Gaussian approximation to measure axial resolution accurately. To measure axial resolution we compute the full width at half maximum (FWHM) of the point spread function (PSF) of the laser.

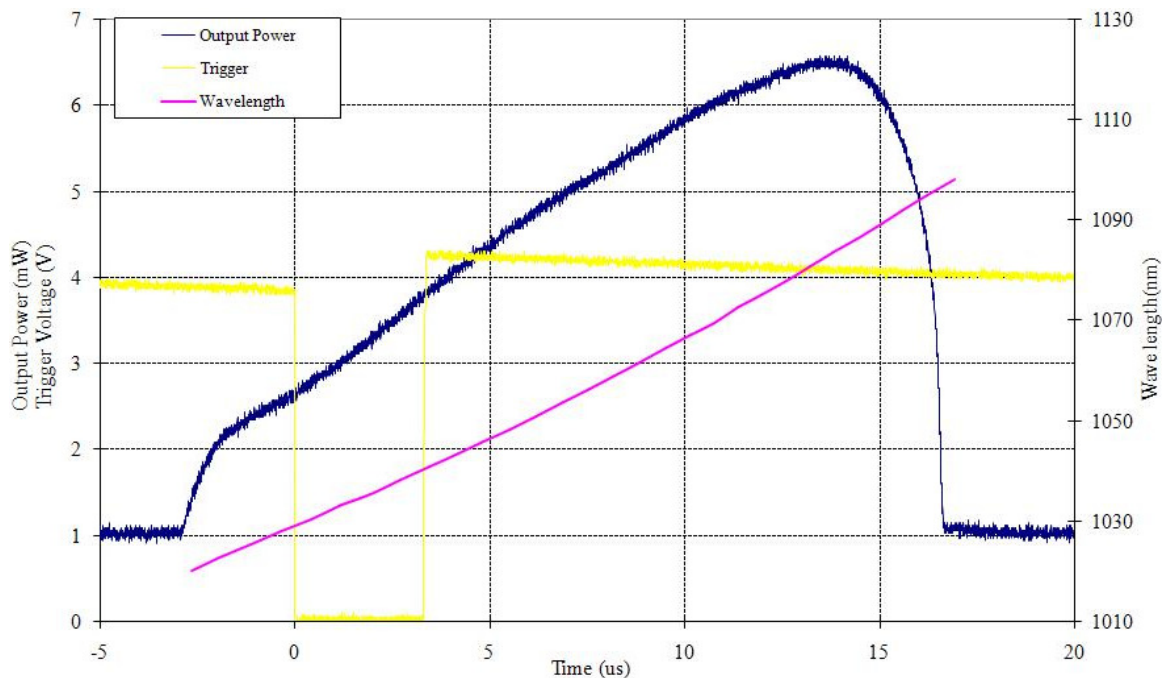


Figure 3.8: Optical spectrum of swept laser source. Blue curve: optical power (mW) as a function of time. Yellow trace: trigger voltage (V). Magenta curve: wavelength versus time

To measure PSF we first measure the optical power spectrum as a function of time, and then using the relationship between wavelength and time we obtain the power spectrum profile as a function of optical frequency (figure 3.9).

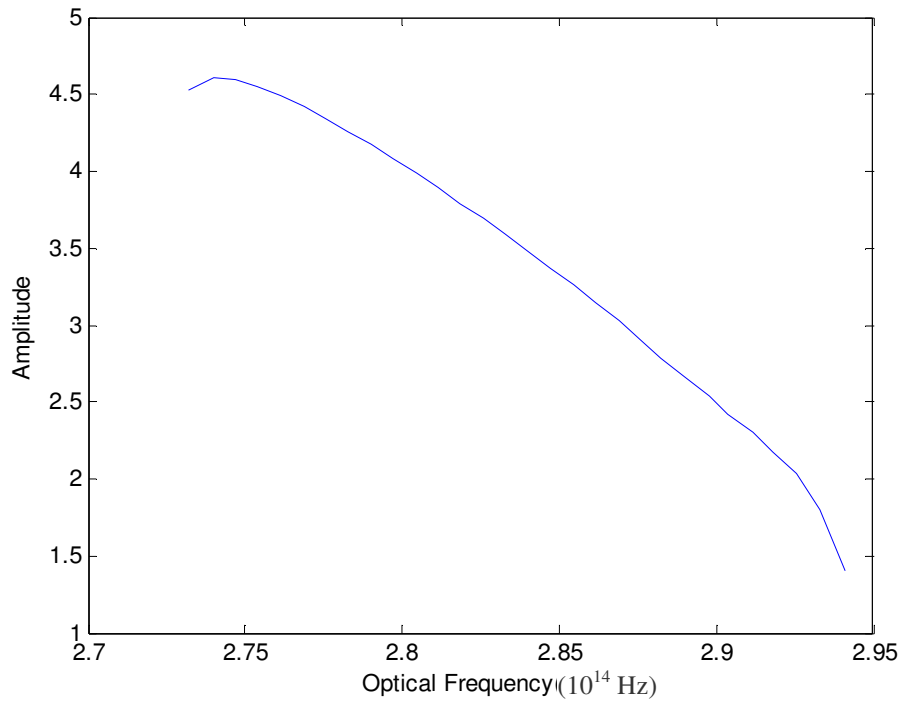


Figure 3.9: Optical power spectrum profile of the swept laser source as a function of optical frequency

Optical power spectrum of figure 3.9 was uniformly sampled and zero padded then inverse Fourier transformed to obtain the PSF. The spatial dependence of the source PSF was obtained by multiplying the time delay by the speed of light (Figure 3.10a). A zoomed in image of the PSF is shown in figure 3.10b.

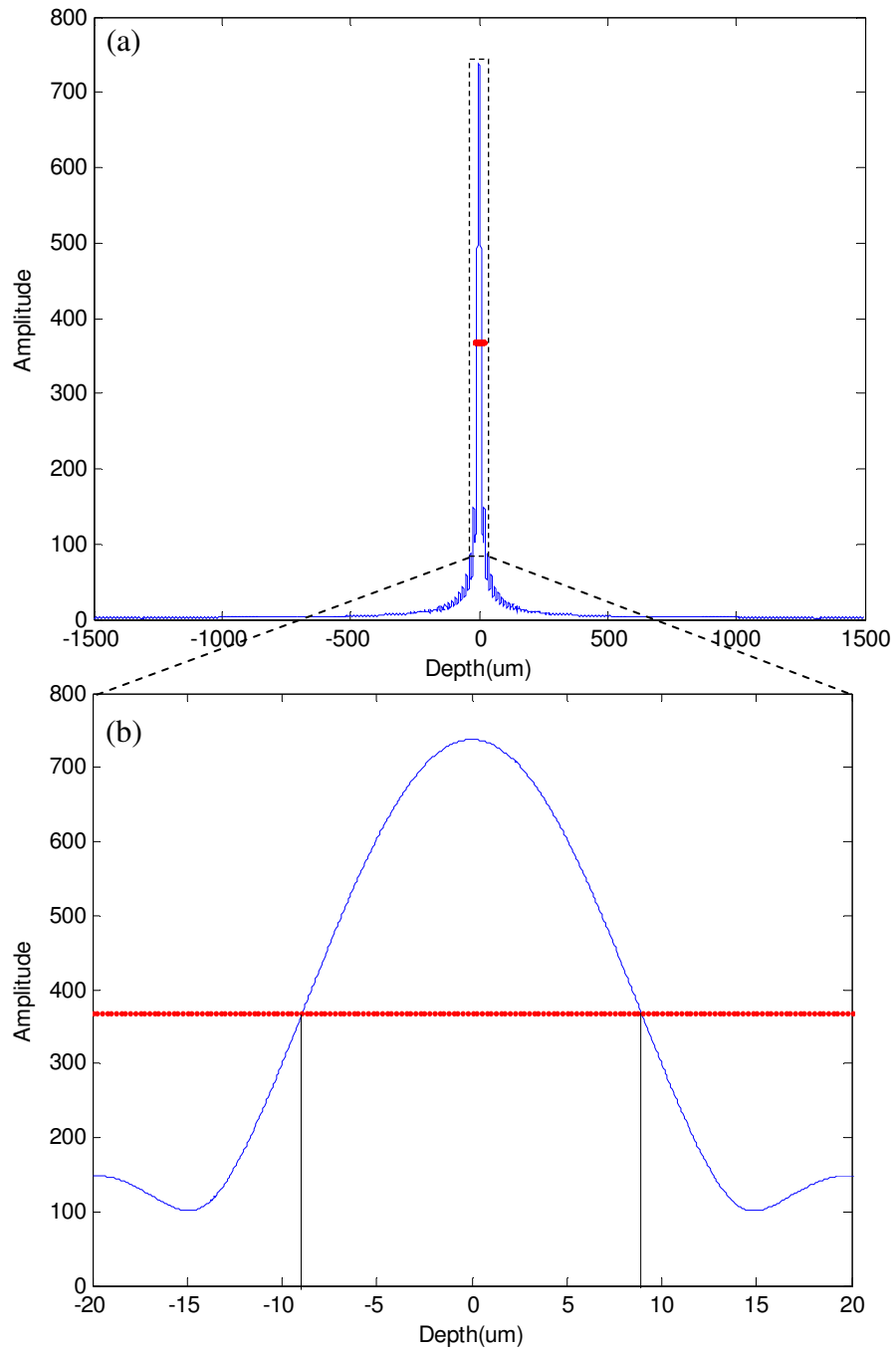


Figure 3.10: (a) Swept laser source PSF. (b) A zoomed in view of the PSF near the center. Amplitude is in arbitrary units

Axial resolution taken as the FWHM of the coherence function envelope is 17.4 μm and matched experimental axial resolution of about 17.1 μm measured with a single reflector positioned at the sample arm. Measured axial resolution in air corresponds to a resolution of about 12.4 μm in tissue (assuming an average index of refraction of 1.38). If the swept source laser profile had a perfectly Gaussian distribution with center wavelength at 1059nm and FWHM $\Delta\lambda$ of 58nm, then the theoretical resolution of 8.5 microns given by equation (1.3) could be achieved in air.

3.4.2 SNR and Sensitivity

To measure SNR and sensitivity, light from the sample arm was passed through a neutral density filter (NDF) then focused onto a mirror. With a total attenuation of 43.7dB, SNR was measured to be 48.6dB at a depth of 0.2 mm. Attenuation represented the double pass signal attenuation through the variable NDF and focusing lens, and is given by:

$$Attenuation = 20 \log_{10} \left(\frac{I_{in}}{I_{out}} \right) \quad (3.6)$$

$$Sensitivity = SNR + Attenuation \quad (3.7)$$

Electrical system sensitivity given by equation (3.7) was calculated to be 92.3dB at 0.2mm depth or 93.4dB at 0mm depth with 6.4mm/dB sensitivity roll off. Coupling losses in the system were not minimized at the time of the measurement nor was the analog quadrupled clock used, so higher SNR and sensitivity is expected.

Chapter 4: Polarimetric Data Processing

4.1 INTRODUCTION

Swept source polarization sensitive optical coherence tomography (SS-PSOCT) provides high resolution depth-resolved tomographic imaging with ability to characterize phase retardation (δ), birefringence (Δn), and eigen-axis ($\hat{\beta}$) of turbid birefringent media. Several methods to measure δ and Δn using PSOCT data have been suggested [29, 39, 45, 50]. These methods are successful in measuring δ and Δn with good accuracy for thick sections of highly birefringent samples like tendon ($\Delta n \approx 10^{-3}$) but introduce uncertainties for thin samples of weakly birefringent tissue like the retinal nerve fiber layer (RNFL) ($\Delta n \approx 10^{-4}$).

Speckle noise is common to spatially coherent imaging methods such as ultrasound and OCT and contributes to image degradation [57]. Speckle's degrading effects are also present in PSOCT polarimetric detection and hinder accurate detection of tissue retardation and birefringence [58]. Kemp et al. used multiple incident states and a nonlinear fitting algorithm to determine polarimetric tissue properties with high sensitivity and invariance to unknown incident state and unitary polarization transformations [59]. Kemp et al. demonstrated the high sensitivity of the method in imaging a thin turbid birefringent film and in primate RNFL using a bulk-optics time-domain PS-OCT system.

We developed the same technique "multiple states nonlinear fitting algorithm" for our SS-PSOCT system and confirmed correctness by measuring phase retardation and birefringence of a thin turbid birefringent film similar to that used by Kemp et al. and

then applied the technique to measure with high accuracy birefringence, phase retardation, and optic axis of human RNFL.

4.2 THEORY

In our SS-PSOCT system interference between reference and sample arm light for vertical, $\Gamma_v(z)$, and horizontal, $\Gamma_h(z)$, polarization components is detected. After detection and digitization, the real-valued interference fringe intensities are windowed. The window used is similar to a Hanning window and can be adjusted to increase image contrast albeit at the cost of decreased axial resolution and SNR. Depth-resolved horizontal $E_h(z)$ and vertical $E_v(z)$ complex electric field amplitudes, and relative phase difference $[\phi_{diff}(z)]$ are obtained by an optimized fast Fourier transform (FFT) algorithm based on the Intel[®] C primitives. We used three consecutive input polarization states (state 0: $-2\pi/3$, state 1: 0, and state 2: $2\pi/3$) uniformly distributed on the QU great circle on the Poincare sphere. To remove the effect of the input polarization states on the reference beam we introduce phase correction to $\phi_{diff}(z)$. For data corresponding to state 0, we add $-2\pi/3$ to $\phi_{diff}(z)$, for data corresponding to state 2 we add $2\pi/3$ to $\phi_{diff}(z)$.

Stokes vector, $\vec{S}(z)$, represents the intensity and polarization state of light backscattered from the tissue specimen at depth z , whose parameters are related to the amplitudes of the components of the electric field, $E_h(z)$ and $E_v(z)$, resolved in two perpendicular directions normal to the direction of propagation, $E_h = E_{h0}(t)\cos(\omega t + \delta_h)$ and $E_v = E_{v0}(t)\cos(\omega t + \delta_v)$.

$$\vec{S}(z) \equiv \begin{bmatrix} I(z) \\ \mathbf{Q}(z) \\ \mathbf{U}(z) \\ \mathbf{V}(z) \end{bmatrix} = \begin{bmatrix} E_V(z)^2 + E_H(z)^2 \\ E_V(z)^2 - E_H(z)^2 \\ 2E_V(z)E_H(z)\cos(\varphi_{diff}(z)) \\ 2E_V(z)E_H(z)\sin(\varphi_{diff}(z)) \end{bmatrix} \quad (4.1)$$

Normalization of Stokes vectors by total radiant power, $I(z)$, provides the necessary information to fully represent depth-resolved polarization data. Normalized Stokes vectors are given by $S(z)$, such that:

$$S(z) \equiv \begin{bmatrix} Q(z) \\ U(z) \\ V(z) \end{bmatrix} = \begin{bmatrix} E_V(z)^2 - E_H(z)^2 \\ 2E_V(z)E_H(z)\cos(\varphi_{diff}(z)) \\ 2E_V(z)E_H(z)\sin(\varphi_{diff}(z)) \end{bmatrix} / (E_V(z)^2 + E_H(z)^2) \quad (4.2)$$

4.2.1 Poincare Sphere Representation of Noise-Free Data

Normalized Stokes polarimetric data is plotted using a three-dimensional Cartesian coordinate system (Q, U, V) on a sphere with unit radius. The Poincare sphere is useful to visualize light propagation in birefringent media [60, 61]. Stokes parameters representing polarization state of light backscattered from depth z in the specimen are uniquely represented by a single point on the Poincare sphere.

In a noise-free model the idealized behavior of the propagation of depth-resolved polarization data $S(z)$ on the Poincare sphere in the absence of diattenuation is a circular arc on the surface of the sphere [P(z)]. In the presence of diattenuation the circular arc is modified to a spiral converging toward the eigen-axis ($\hat{\beta}$) (figure 4.1). Diattenuation is the differential amplitude attenuation between eigenpolarization states. Light backscattered from a tissue specimen at depth z accumulates a total phase-delay equal to the round-trip or double-pass retardation [$2\delta(z)$] and differential attenuation

corresponding to double pass diattenuation $[2\varepsilon(z)]$. However, since diattenuation is negligible in the RNFL we will only concentrate on results of phase retardation $\delta(z)$.

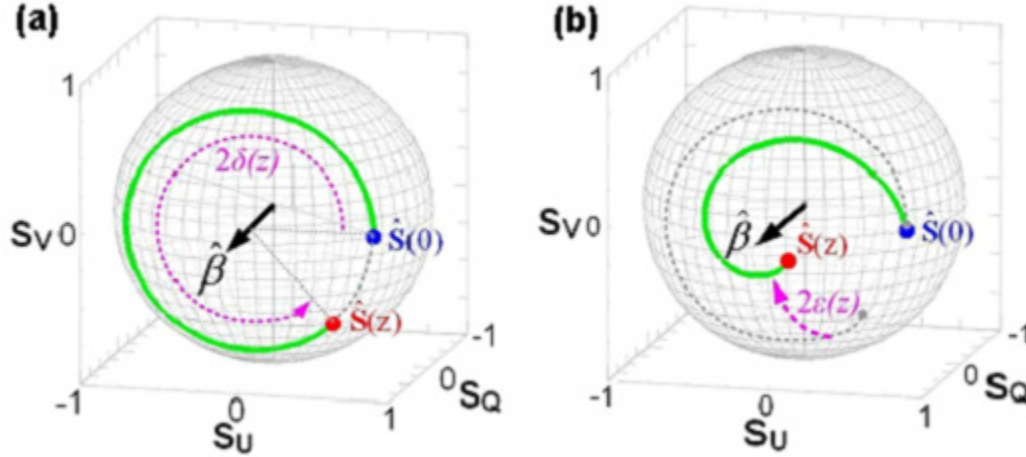


Figure 4.1: Trajectories from the specimen surface to depth z of noise-free propagation of backscattered light in anisotropic media represented on the Poincaré Sphere. (a). Arc due to double pass retardation, $2\delta(z)$, about $\hat{\beta}$ only. (b). Same circular arc converging toward $\hat{\beta}$ in the presence of double pass diattenuation, $2\varepsilon(z)$, results in a three-dimensional spiral [62].

4.2.2 Estimation of RNFL Parameters

To determine phase retardation from polarimetric speckle noise corrupted data $[S(z)]$ recorded with the SS-PSOCT instrument requires estimation of three model parameters to mathematically specify the noise-free model polarization arc $P(z)$. The three parameters are double pass phase retardation, 2δ , eigen-axis, $\hat{\beta}$, and polarization state at the first surface $P(0)$. A Levenberg-Marquart [63] multi-state nonlinear fitting algorithm is used to determine double-pass phase retardation and eigen-axis for the polarimetric speckle noise corrupted data. Implementation of the algorithm requires a

residual function, R_M , (M=3 incident polarization states for our SS-PSOCT system implementation) such that

$$R_M = \sum_{m=1}^M R_0 \left(S_m(z); \delta, \hat{\beta}, P_m(0) \right) \quad (4.3)$$

R_0 measures cumulative squared deviation between noisy $S(z)$ and noise-free model $P(z)$ and specifies goodness of fit.

$$R_0 = \sum_n \left| S(z) - P(z; 2\delta, \hat{\beta}, P(0)) \right|^2 \quad (4.4)$$

The multiple-state nonlinear fitting algorithm is an efficacious approach for determining tissue polarimetric parameters since all M noise-free model polarization arcs $P_m(z)$ are constrained to rotate about the same eigen-axis $\hat{\beta}$ by the same retardation 2δ . Uncertainty in any polarization state's arc is compensated for by the constraints placed on the other $m-1$ arcs by the residual function R_M . The multiple-state nonlinear algorithm has the advantage that it uses all depth-resolved points to measure polarimetric properties of specimen unlike other methods that only consider start and end points in their estimation [64-66].

4.2.3 Nonlinear Fitting Uncertainty

Uncertainty or asymptotic standard parameter errors of Levenberg-Marquardt non-linear fitting algorithm are calculated from the sum of squares of distances between measured and fitted data points.

$$\sigma_p = \sqrt{\text{diag} \left(\left[J^T J \right]^{-1} \cdot \frac{\sum_{i=1}^N (S_i - P_i)^2}{N} \right)} \quad (4.5)$$

where S_i is i^{th} measured noisy data point, P_i is i^{th} noise-free fitted data point, N is number of data points, J is Jacobian matrix $[\partial P/\partial x]$, vector x represents all inputs for the non-linear model. J represents local sensitivity of the model to variation in the parameter x .

The “uncertainty” we use in the remainder of this dissertation is defined as $\sigma_p \cdot z_\alpha$, where α is the confidence interval for the fitted parameters, and z_α is the normal distribution boundary at confidence interval α . For example, if confidence interval is set as 95% and unit phase retardation is y , then uncertainty is measured as $1.96\sigma_p$ ($z_{0.95}=1.96$), and the probability that the true unit phase retardation is in the range $[y-1.96\sigma_p, y+1.96\sigma_p]$ will be 95%.

4.2.4 Polarimetric Signal to Noise Ratio

SS-PSOCT is susceptible to several noise sources (e.g. shot noise, random intensity noise, quantization noise, and intensity speckle noise); however, the most problematic noise source that hinders accurate determination of retardation is polarimetric speckle noise. Intensity speckle noise is common to both polarization channels and is removed from polarimetric data by Stokes vectors normalization. Polarimetric speckle noise, on the other hand, is different for horizontal and vertical polarization channels and causes degradation of trajectories on the Poincare sphere $[S(z)]$.

Kemp et al. introduced the term polarimetric signal-to-noise ratio (PSNR) to characterize the ability of PSOCT to extract a model $P(z)$ from noisy $S(z)$. When differential amplitude attenuation, $[\epsilon(z)]$, is much smaller than phase retardation, $[\delta(z)]$, PSNR is given by [59]:

$$PSNR = \frac{l_{arc}}{\sigma_{speckle}} = \frac{2\delta \sin(\gamma)}{\sigma_{speckle}} \quad (4.6)$$

where l_{arc} is arc length of the noise free polarization arc $P(z)$ associated with $S(z)$, γ is separation angle between eigen-axis $\hat{\beta}$ and model Stokes vector at the first interface $P(0)$. $\sigma_{speckle}$ is polarimetric speckle noise standard deviation and is the point-by-point angular variation on the Poincare sphere between $S(z)$ and model $P(z)$:

$$\sigma_{speckle} = \left(\frac{1}{N} \sum_n \left(\cos^{-1} (S(z) \cdot P(z)) \right)^2 \right)^{1/2} \quad (4.7)$$

where N is number of depth-resolved sample points within the specimen.

Increasing PSNR can be accomplished either by reducing polarimetric speckle noise standard deviation, $\sigma_{speckle}$ or, by increasing arc length, l_{arc} . Reducing polarimetric speckle noise can be achieved by increasing number of uncorrelated speckle fields, N_A . Ensemble averaging of N_A separate trials is known to reduce additive white noise in recorded signals by a factor of $N_A^{1/2}$. Although statistics of polarimetric speckle noise in SS-PSOCT are not necessarily similar to white noise, Kemp et al. showed experimentally that averaging N_A uncorrelated speckle fields increases PSNR by $N_A^{1/2}$ for up to 36 speckle fields [59]. We experimentally demonstrated a ten-fold increase in PSNR after averaging Stokes vectors for $N_A = 100$ speckle fields in a birefringent film, after which a diminished return was obtained with increased N_A . Increasing PSNR can also be accomplished by increasing arc length, l_{arc} . Arc length is a function of retardation δ and angle separation between the eigen-axis $\hat{\beta}$ and the initial Stokes vector $P(0)$. Retardation and $\hat{\beta}$ are sample dependent and therefore if incident polarization state on the specimen is such that $\delta = 90^\circ$ arc length and hence PSNR are increased. However, since single-mode optical fiber and anterior segments of the eye introduce birefringence choosing $P(0)$ a priori to provide 90 degree angle separation is usually not possible.

Assuming birefringence is the same at 850 nm and 1060 nm, such that: $\Delta n_{850} = \Delta n_{1060} = \Delta n$, and re-writing equation (1.36) we get:

$$\frac{\lambda_{1060}}{2\pi} \cdot \frac{\delta_{1060}(z)}{z} = \Delta n = \frac{\lambda_{850}}{2\pi} \cdot \frac{\delta_{850}(z)}{z} \quad (4.8)$$

Eliminating the common terms in equation (4.8) above, we get:

$$\delta_{850}(z) = \frac{\lambda_{1060}}{\lambda_{850}} \cdot \delta_{1060}(z) = \frac{1060}{850} \cdot \delta_{1060}(z) = 1.25 \cdot \delta_{1060}(z) \quad (4.9)$$

Polarimetric OCT imaging at 850 nm might have an advantage over imaging at 1060 nm since phase retardation would be 25% larger than at 1060 nm and the larger phase retardation the higher PSNR would presumably provide a more accurate measurement. However, a more detailed study would need to take into consideration other factors that affect PSNR of imaged sample.

To increase PSNR and therefore decrease phase retardation measurement uncertainty we acquired data in clusters of N_A averaged uncorrelated A-scans. RNFL anterior and posterior boundaries were detected (boundary detection described in section 5.1). Then Q, U, and V are measured for each of the N_A uncorrelated consecutive A-scans and averaged. The averaged Q, U, and V, are then normalized by $I_{ave}(z) = \sqrt{Q_{ave}^2 + U_{ave}^2 + V_{ave}^2}$ to obtain depth-resolved normalized Stokes vectors, $S(z)$ for each cluster of N_A A-scans. We used three incident polarization states (state 0: $-2\pi/3$, state 1: 0, and state 2: $2\pi/3$) uniformly distributed on the QU great circle on the Poincare sphere. Using multiple incident polarization states insures that at least one separation angle will be close to ninety degrees ($\gamma_m \approx 90^\circ$).

Figure 4.2 shows the relationship between averaging N_A uncorrelated fields and increase in measured PSNR. The top row shows noisy polarization arcs, $S_m(z)$, and noise-free model polarization arcs, $P_m(z)$, for a thick cluster from the inferior quadrant of a healthy volunteer's left eye. The bottom row shows $S_m(z)$ and $P_m(z)$ for a thin cluster from the nasal quadrant of the same healthy volunteer's left eye. Left column shows the results of ensemble averaging 100 A-scans per cluster; the middle column shows the

results of ensemble averaging 36 A-scans per cluster; the right column shows the result of 16 A-scans per cluster. $\hat{\beta}$ represents polarization eigen-axis. For the thick cluster 36 A-scans per clusters are sufficient to accurately estimate birefringence and eigen-axis $\hat{\beta}$, whereas for the thin cluster 36 A-scans per cluster introduce substantial error in estimation of eigen-axis $\hat{\beta}$ and up to 81 A-scans per cluster are needed for the accurate estimation of eigen-axis $\hat{\beta}$, birefringence is still fairly accurately estimated with 49 A-scans per cluster. Points in figure 4.3 show the resultant increase in PSNR as a function of number of ensemble averaged uncorrelated fields, N_A . Measured PSNR increases by a factor of $N_A^{1/2}$ with 95% confidence. It is apparent from the figure that PSNR no longer increases by $N_A^{1/2}$ after $N_A = 81$. The reason for diminished increase could be due to imperfect separation between averaged fields such that some of the fields are still correlated.

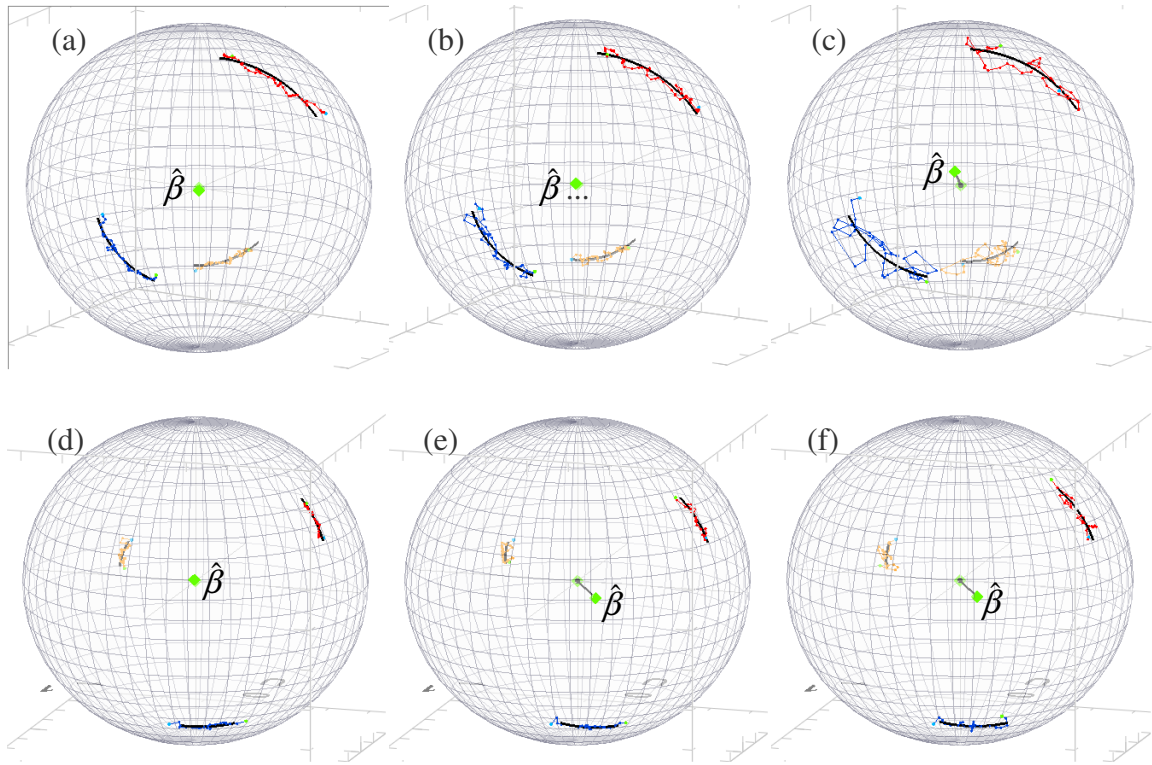


Figure 4.2: Arcs and fits recorded from the left eye of a healthy patient. Top row is from a thick cluster in the inferior quadrant. Bottom row is from a thin cluster in the nasal quadrant. (a): 100 A-scans per cluster, PSNR = 32.58 dB. (b) 36 A-scans per cluster, PSNR = 26.90 dB. (c) 16 A-scans per cluster, PSNR = 11.71 dB. (d) 100 A-scans per cluster, PSNR = 21.99 dB. (e) 36 A-scans per cluster, PSNR = 18.35 dB. (f) 16 A-scans per cluster, PSNR = 13.82 dB. For thick clusters 36 A-scans per clusters are sufficient to accurately estimate birefringence and eigen-axis $\hat{\beta}$, whereas for thin clusters 36 A-scans per cluster introduce an error in birefringence and eigen-axis $\hat{\beta}$ estimation and 81 A-scans per cluster are needed for the accurate estimation of birefringence and eigen-axis $\hat{\beta}$.

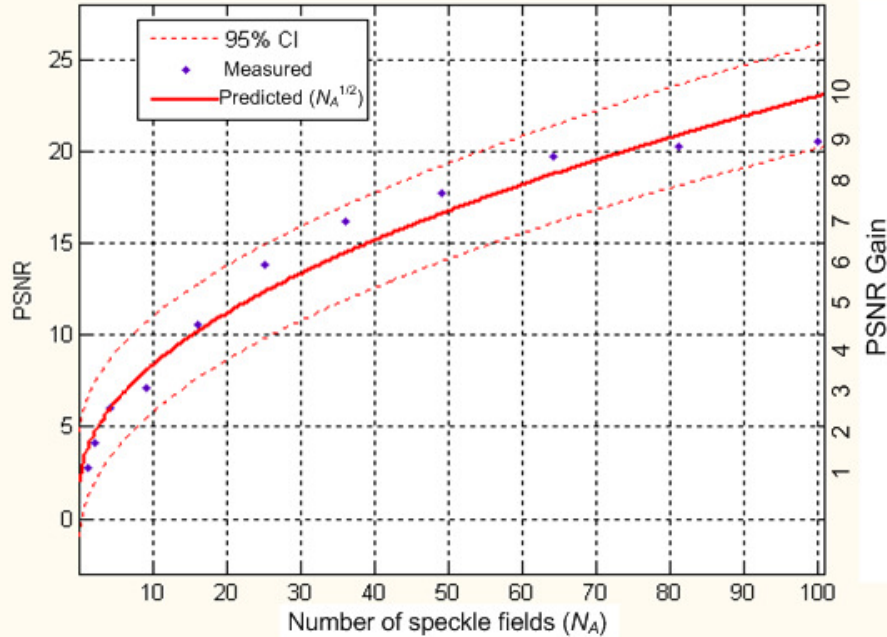


Figure 4.3: Ensemble averaging of N_A uncorrelated fields increases PSNR by a factor of $N_A^{1/2}$. Data was acquired from the RNFL of a healthy individual’s left eye.

4.3 RESULTS

Inasmuch as no generally accepted turbid polarimetric standard to measure accuracy of PS-OCT systems exists, system calibration is difficult. Most researchers have used a quarter-wave-plate to measure polarimetric accuracy which is problematic since data from only two axial points is obtained (from first and last surfaces) and birefringence is high and may encompass many waves of retardation. To measure SS-PSOCT system sensitivity for birefringence measurement with the multiple-state nonlinear fitting algorithm, we measured phase retardation (δ) and birefringence (Δn) of a thin weakly birefringent turbid film (NewFocus model 5842) similar to that used by Kemp et al.

Three incident polarization states and 100 A-scans per cluster were recorded on a square grid area on the (150 μm thick) birefringent film. Single pass phase retardation was measured to be $\delta = 38.1^\circ$, which corresponds to single pass phase retardation per 100 μm of $25.4^\circ/100\mu\text{m}$ or $\Delta n = 7.48 \cdot 10^{-4}$ at 1060 nm center wavelength. Kemp et al. measured $\delta = 24.5^\circ$ in 80 μm thickness of the same birefringent film single pass phase retardation which corresponds to $30.6^\circ/100\mu\text{m}$ or $\Delta n = 7.23 \cdot 10^{-4}$ at a wavelength of 850 nm. A possible reason for discrepancy in birefringence values between our SS-PSOCT measurement and that obtained with Kemp's bulk optics system is measurement uncertainty of the two systems or that the sample measurements were recorded at different locations. Considering a single pass uncertainty in our measurement ($\pm 0.5^\circ/100\mu\text{m}$), our birefringence value is in the range $[7.33 - 7.6] \cdot 10^{-4}$ and using Kemp et al. $\pm 1^\circ/100\mu\text{m}$ single pass measurement uncertainty birefringence value is in the range $[6.99 - 7.47] \cdot 10^{-4}$.

The birefringent film is an excellent retardation calibration target since the film is weakly birefringent ($\sim 7 \cdot 10^{-4}$) and close to the average RNFL birefringence ($\sim 3.2 \cdot 10^{-4}$) [20]. The film also exhibits scattering, although weaker than the RNFL, can be of similar SNR to that recorded from the RNFL images of elderly patients (the highest risk population for glaucoma).

Figure 4.4 shows the evolution of polarimetric speckle noise corrupted normalized Stokes parameters (Q_n , U_n , and V_n) with their fits for the thin birefringent film for three incident polarization states ($S_0 = -120^\circ$, $S_1 = 0^\circ$, and $S_2 = +120^\circ$) as well as polarimetric speckle corrupted arcs, $S_m(z)$ and their noise-free fits, $P_m(z)$ on the Poincare sphere such that $m = 0, 1, \text{ and } 2$. All three incident polarization states on the Poincare sphere fit to the same eigen-axis, $\hat{\beta}$.

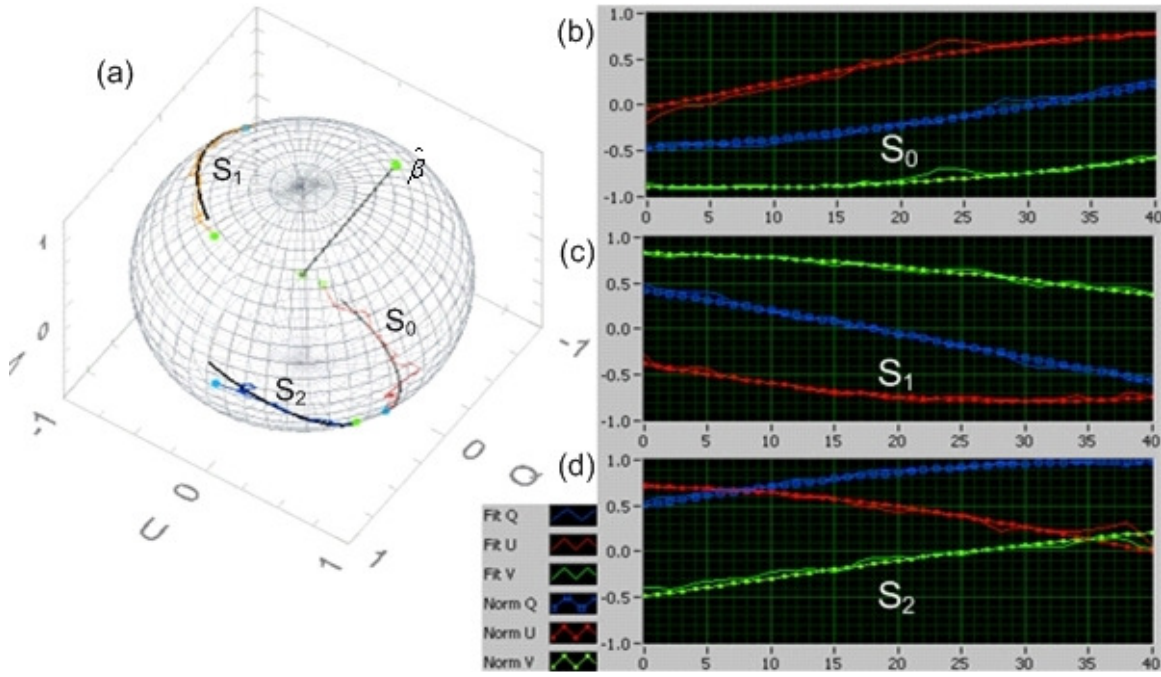


Figure 4.4: Data from the weakly turbid birefringent film showing (a) polarimetric speckle corrupted arcs, $S_m(z)$ and their noise-free fits, $P_m(z)$ such that $m = 0$ (red), 1(orange), and 2(blue). All three states on the Poincaré sphere fit to the same eigen-axis, $\hat{\beta}$. Evolution of the polarimetric speckle noise corrupted normalized Stokes parameters (Q_n , U_n , and V_n) for the three incident polarization states (b): $S_0 = -120^\circ$, (c): $S_1 = 0^\circ$, and (d): $S_2 = +120^\circ$ (solid lines), as well as the noise-free model fits (dotted lines)

4.4 CONCLUSION

We tested accuracy of the SS-PSOCT system without balanced detection by imaging a turbid weakly birefringent film and obtained comparable results to those published by Kemp et al. We successfully determined noise free polarimetric properties of the turbid weakly birefringent film using the nonlinear fitting algorithm with multiple incident polarization states. Increasing the number of uncorrelated speckle fields increased PSNR by the square root of number of averaged speckle fields.

Chapter 5: Patient Measurements

5.1 BLOOD VESSEL DETECTION AND IMAGE REGISTRATION

Blood vessel detection is important in retinal imaging since eye vasculature can be used as a landmark for image registration. Accurate blood vessel detection depends on underlying contrast provided by the imaging scheme. For example, one contrast mechanism arises from the difference in light absorption between blood and tissue; other contrast mechanisms include speckle or Doppler shift differences between blood and surrounding tissue.

Blood vessels have been detected from three types of acquired images: line scanning laser ophthalmoscope (LSLO) images, raster scan polarization diverse intensity images, and continuous ring scan polarization diverse intensity images. Blood vessels are visualized directly in LSLO images, but with raster and continuous OCT ring scans, a blood vessel map must be reconstructed with a depth integral of signal intensity. For each retinal position, signal intensity from 185 μm deep from the anterior surface of the retina down to of 370 μm depth is averaged. Blood vessels about the optic nerve head tend to be closer to the posterior boundary of the RNFL and the lower layers of the retina. Signal intensity was not averaged starting at the anterior retinal surface, because the strong signal from above blood vessels would decrease contrast between blood vessels and surrounding tissue.

Steps needed for constructing blood vessel maps from recorded PS-OCT raster scan images are described in figure 5.1. First, the anterior boundary of the RNFL is detected for each B-scan of a PS-OCT continuous raster scan. Average signal intensity is calculated from 185 μm to 370 μm deep from the anterior RNFL boundary. Juxtaposing

averaged signals from all B-scans produces a fundus-like image of the retina centered about the optic nerve head (figure 5.1b). Each averaged signal layer in figure 5.1a corresponds to a layer in figure 5.1b. A 2-D median filter is applied to the fundus-like image, then adaptive histogram equalization. Edges are detected using a canny edge detection algorithm (figure 5.1c).

The boundary detection algorithm is an intensity based algorithm that works on individual A-scans. The first step in the process is to apply a Wiener filter to the B-scan using a rectangular filter. The goal is to reduce speckle noise along the axis of the boundary and maintain edges in the B-scan image. Several filters were tried, but the Wiener filter provided the best combination of despeckling and edge preservation in our OCT images. The curvelet transform also performed very well; however, inaccurate features were introduced along the curvelet directions. After the B-scan is Wiener filtered, each despeckled A-scan has a bisquare fit applied. Bisquare fitting further removes influence of speckle and gives a smooth curve. A simple threshold is applied to the curve fit which then gives anterior and posterior RNFL boundaries. Each boundary is independently filtered to remove outliers. Boundaries are then overlaid on the images.

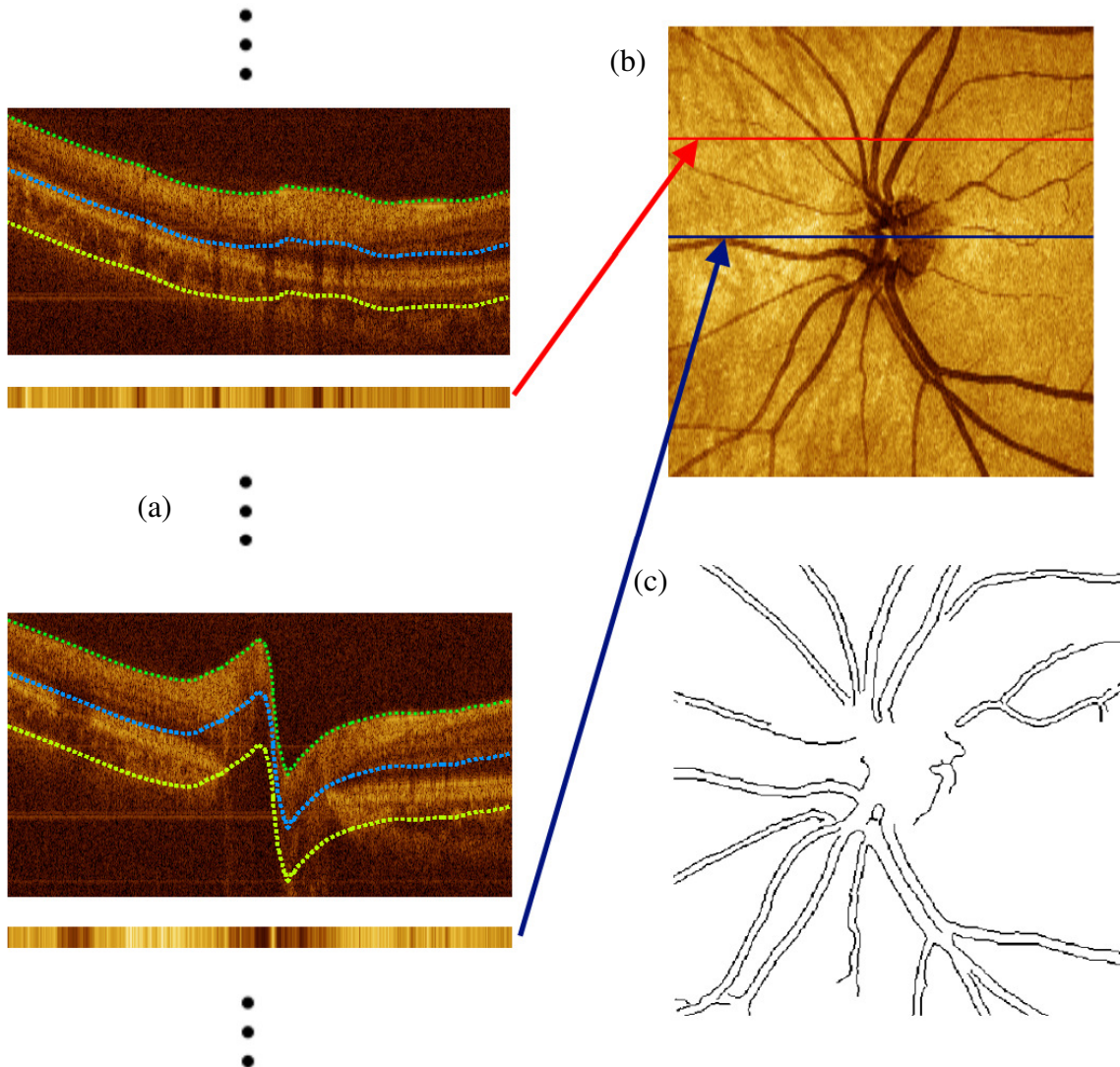


Figure 5.1: Steps to reconstruct blood vessel map from OCT raster scans. (a) B-scan images from different locations in the retina. Green dotted line represents anterior RNFL boundary; blue line represents the offset from which intensity is averaged; fluorescent green line represents the boundary at which averaging is stopped. Average signal intensity is displayed below each B-scan. (b) Averaged signals from each B-scan are plotted as a line representing the location of the B-scan acquisition until the whole fundus-like image is reconstructed. (c) Map of blood vessel edges reconstructed from the fundus-like image in (b).

The method of reconstructing a blood vessel map from ring scan images is similar to the method described above for reconstructing blood vessel map from raster scan images, with the additional step of applying a polar transformation to B-scan data.

The fundus-like maps reconstructed from raster scan images and continuous ring scan images (figure 5.2a, b) show more contrast and at higher resolution than the LSLO fundus-like image (figure 5.2c). Blood vessel maps detected from the fundus-like images of figure 5.2 are shown in figure 5.3. The blood vessel maps suggest that raster scans give better results than ring scan and both work better than the LSLO.

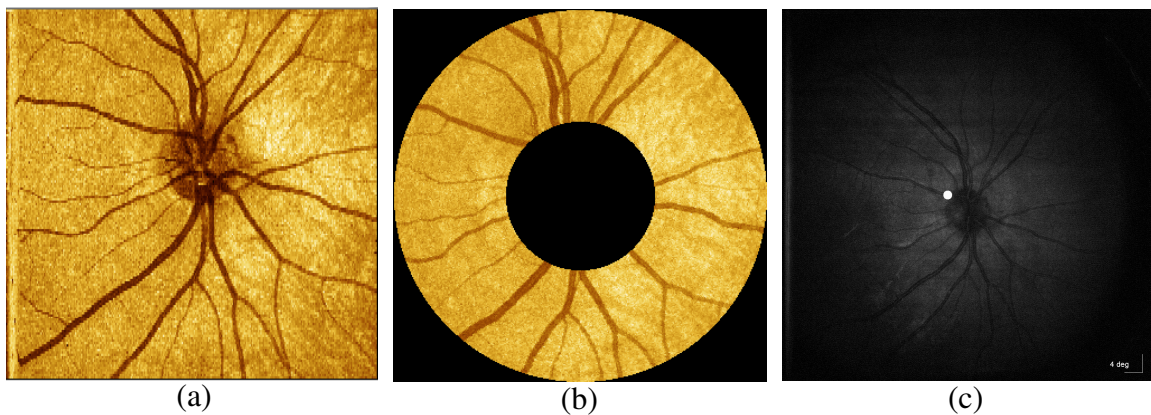


Figure 5.2: Fundus-like images reconstructed from (a) raster scan and (b) continuous ring scan (c) LSLO image. All maps are from the same imaging session.

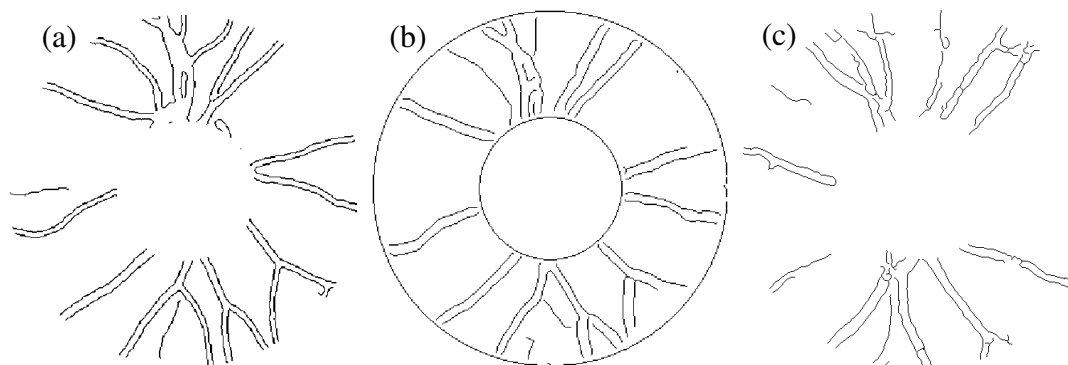


Figure 5.3: Blood vessel edges obtained from (a) raster scan, (b) continuous ring scan, and (c) LSLO images.

5.2 CLUSTERED THICKNESS, BIREFRINGENCE, AND PHASE RETARDATION MAPS

5.2.1 Clustered Ring Scan and Clustered Maps

Our SS-PSOCT system can be used to measure thickness, birefringence, and phase retardation of the RNFL. In order to record more accurate measurements with less uncertainty, clusters of 100 uncorrelated A-scans are averaged to form clustered RNFL thickness, birefringence, and phase retardation maps. A set of clustered ring scans is performed to acquire clustered maps. The eye fundus is divided into annular rings. Each ring consists of a number of clusters, where each cluster is formed by N_A A-scans. Figure 5.4 shows a clustered scan pattern overlaid on the LSLO image. The clustered scan consists of 10 rings of 36 clusters each. Each cluster is made up of 100 A-scans in a sinusoidal pattern.

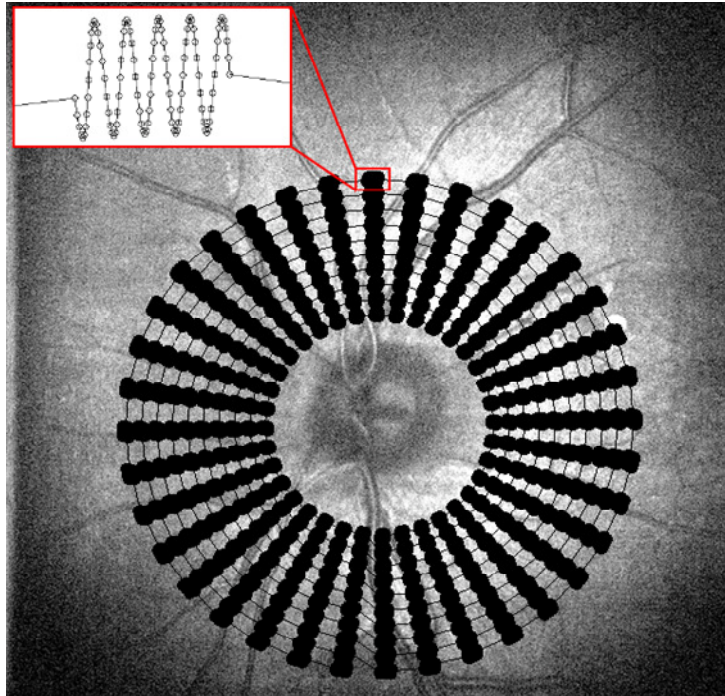


Figure 5.4: Scanning pattern of clustered ring scan overlaid on the LSLO fundus image. Scanning pattern of each cluster is shown in the inset in the upper-left corner. Each circle in the inset represents A-scan. The area covered by the cluster is $66\mu\text{m} \times 42\mu\text{m}$ for inner ring and $66\mu\text{m} \times 130\mu\text{m}$ for outer ring.

5.2.2 RNFL Boundary Detection

Many factors complicate accurate RNFL thickness measurement. Blood vessels obscure portions of the RNFL in recorded PS-OCT images. Thresholds for the boundary detection algorithm (section 5.1) were selected so that the posterior RNFL boundary is at the top of the blood vessel when large blood vessels are present but includes the whole RNFL when no blood vessel or small blood vessels are present. Another important error factor comes from the system axial resolution limitation ($12\mu\text{m}$ in tissue). Uncertainty in RNFL group index assumed to be $n = 1.38$ (1.34 — 1.39) can introduce up to 4% error.

Anterior RNFL boundary layer is easily determined since a sharp and usually smooth gradient difference exists between the RNFL and the aqueous humor. Automatic determination of the RNFL posterior boundary on the other hand is not trivial since intensity gradient at the edge is not sharp and is usually a nonuniform boundary. Erroneous boundary detection can further influence birefringence measurement accuracy. If a detected posterior boundary is overestimated, fitted arcs will be skewed and introduce error. If instead the boundary is greatly underestimated then birefringence measurement uncertainty will be high. Inclusion of data overlying and possibly containing blood vessels data for birefringence estimation may greatly affect accuracy since blood flow introduces phase shift between horizontal and vertical polarization states of light that may be interpreted as phase delay and hence birefringence. Accurate boundary detection is hence of the utmost importance. Moreover, excluding large blood vessel data it is required when measuring birefringence.

To accurately measure birefringence, a three-step approach was implemented: (1) automatic boundary detection, (2) automatic/manual boundary detection, and (3) manual boundary detection. The three-step approach is described in a flow chart (figure 5.5). An automatic boundary detection algorithm is used to first determine RNFL boundaries and calculate birefringence. This method is defined as “automatic” fitting. During automatic birefringence calculation, we also calculate birefringence uncertainty. A threshold value is used to determine if measurement uncertainty is sufficiently low. If uncertainty from automatic fitting is higher than the specified threshold value, then the posterior boundary is defined as fixed offset from anterior boundary for all A-scans in the cluster, where offset is the average RNFL thickness calculated in the previous step by the automatic boundary detection algorithm. This method is the “automatic/manual” method. If uncertainty of automatic/manual fitting is still high (most likely due to the influence of

blood vessels), the user can manually set anterior and posterior boundaries and re-measure until lowest possible measurement uncertainty is obtained. This is the “manual” fitting method.

The RNFL is a birefringent layer surrounded by non birefringent posterior and anterior layers. Birefringent data follows an arc on the Poincare sphere and hence a deviation from the arc occurs when data is collected from a non-birefringent medium. Adding polarization information to the intensity based boundary detection algorithm can potentially improve RNFL boundary detection.

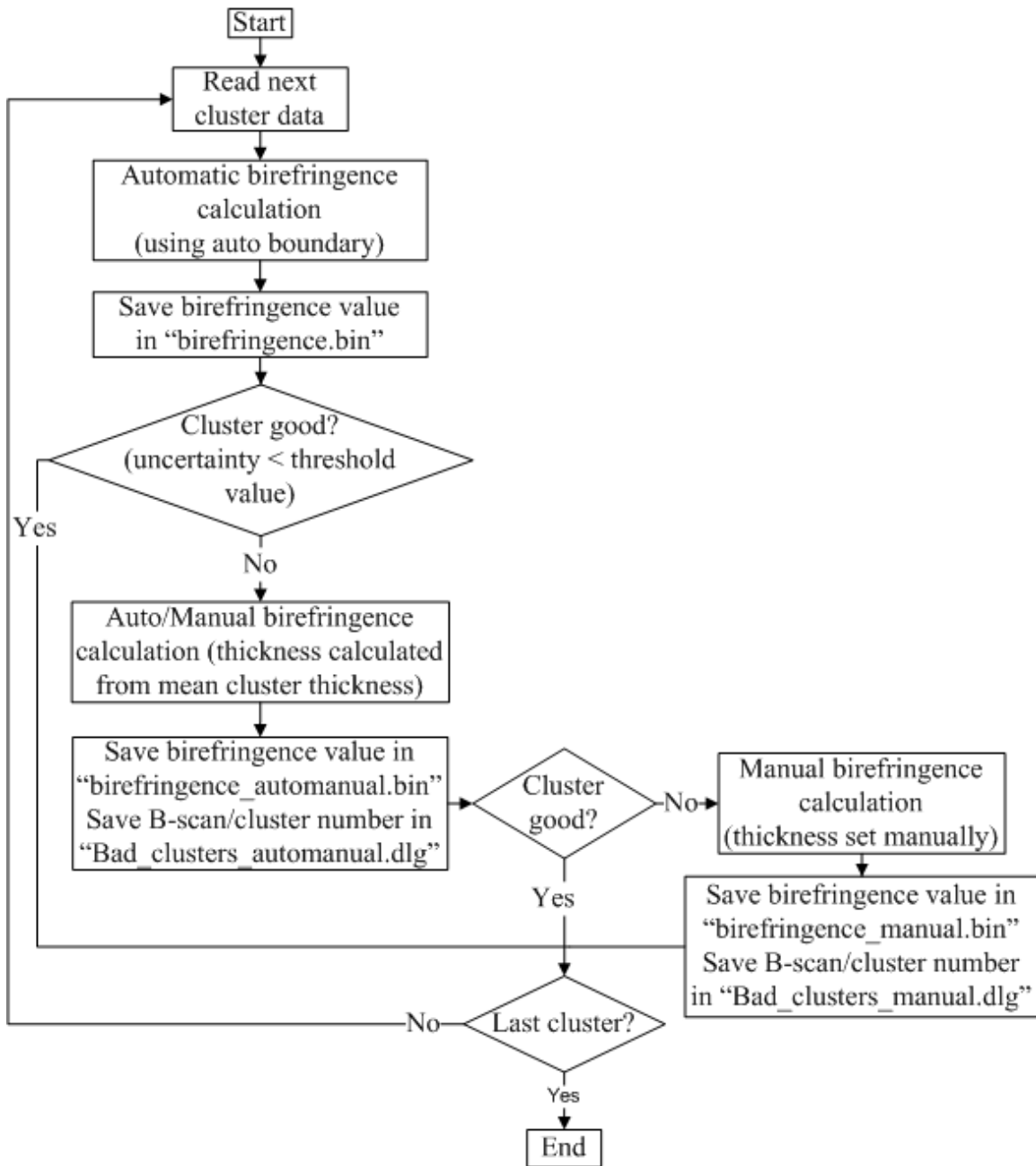


Figure 5.5: Flow chart for calculating clustered birefringence maps using a three-step approach.

Clustered birefringence maps obtained using the three different fitting schemes are shown in figure 5.6. Birefringence maps calculated using automatic/manual fitting

does not show any statistical difference from the birefringence map obtained using manual fitting. However, both maps look substantially different from the one obtained using the automatic scheme. This comparison reveals that the automatic/manual method in the three-step fitting strategy reduces the fitting error and uncertainties of most clusters, whereas only few clusters need to be adjusted manually.

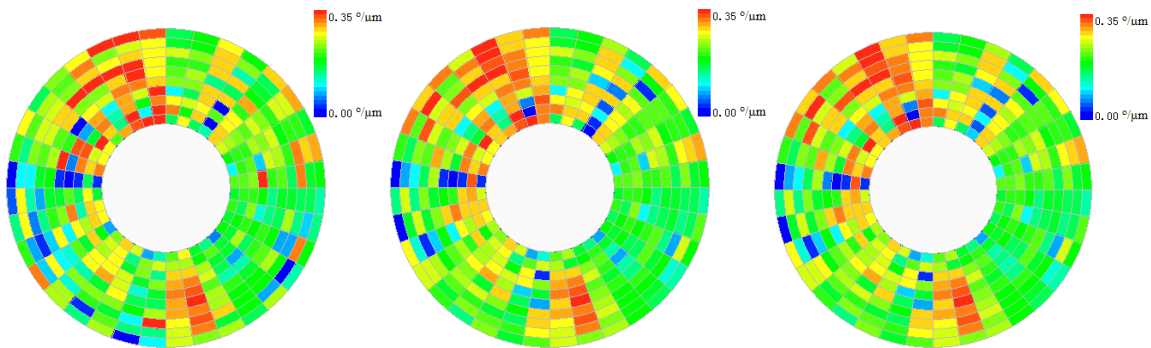


Figure 5.6: Comparison of clustered birefringence maps using different RNFL boundary detection strategies. Left: automatic boundary detection. Middle: auto/manual boundary detection. Right: manual boundary detection.

Averaged uncertainty of all clusters in each scheme is compared in figure 5.7. A paired sample Wilcoxon Sum Rank test (non-parametric method) was performed to calculate p-values comparing uncertainty from each scheme. Wilcoxon Sum Rank test results show significant decrease in uncertainty from automatic to either automatic/manual or manual boundary detection ($p = 0$). Improvement between automatic/manual and manual boundary detection is not significant ($p = 0.5$). Considering the additional time requirement for manual boundary detection, and the limited gain provided by manual boundary detection automatic/manual boundary detection may be sufficient.

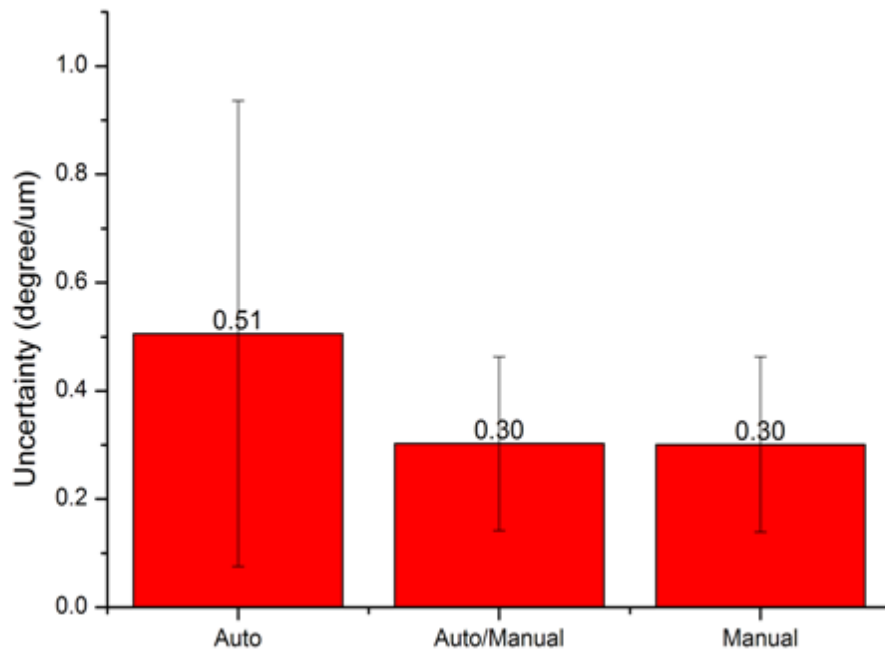


Figure 5.7: Comparison of averaged uncertainty during Stokes fitting using automatic boundary, automatic/manual boundary, and manual boundary detections. Spread bars represent the spread in uncertainty value from all clusters in the map

5.2.3 Optimized Clustered Scan Parameters

In a clustered scan, three scan parameters can significantly impact the processing time of clustered maps: number of B-scans, number of clusters in each B-scan, and number of A-scans per cluster. Generally speaking, a higher B-scan number and/or cluster number results in more detailed clustered birefringence maps, thickness maps, and phase retardation maps, while a larger cluster size decreases uncertainty during fitting. However, increasing any of these parameters significantly increases processing time. To find a balance between performance and processing time, we investigated the impact of each parameter on clustered birefringence maps, thickness maps, and phase retardation

maps in (figures 5.8, 5.9, and 5.10). All maps were from a healthy patient's right eye (OD) and were acquired such that the innermost ring is at 2 mm diameter and the outermost at 5 mm. All maps were analyzed using the auto/manual scheme.

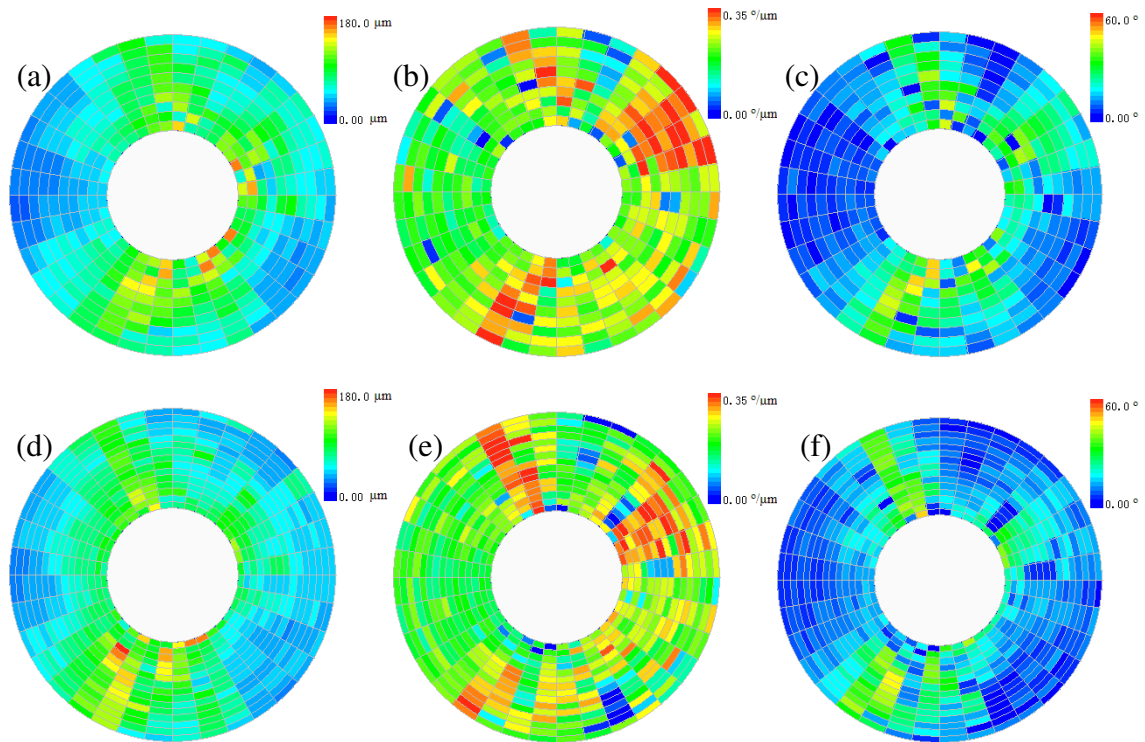


Figure 5.8: Influence of B-scan number. (a) thickness map (10 B-scans); (b) birefringence map (10 B-scans); (c) phase retardation map (10 B-scans); (d) thickness map (15 B-scans); (e) birefringence map (15 B-scans); (f) phase retardation map (15 B-scans). Cluster number = 36 and Cluster size = 100 for all maps. All maps are acquired about the ONH with 2 mm inner ring diameter and 5 mm outer ring diameter.

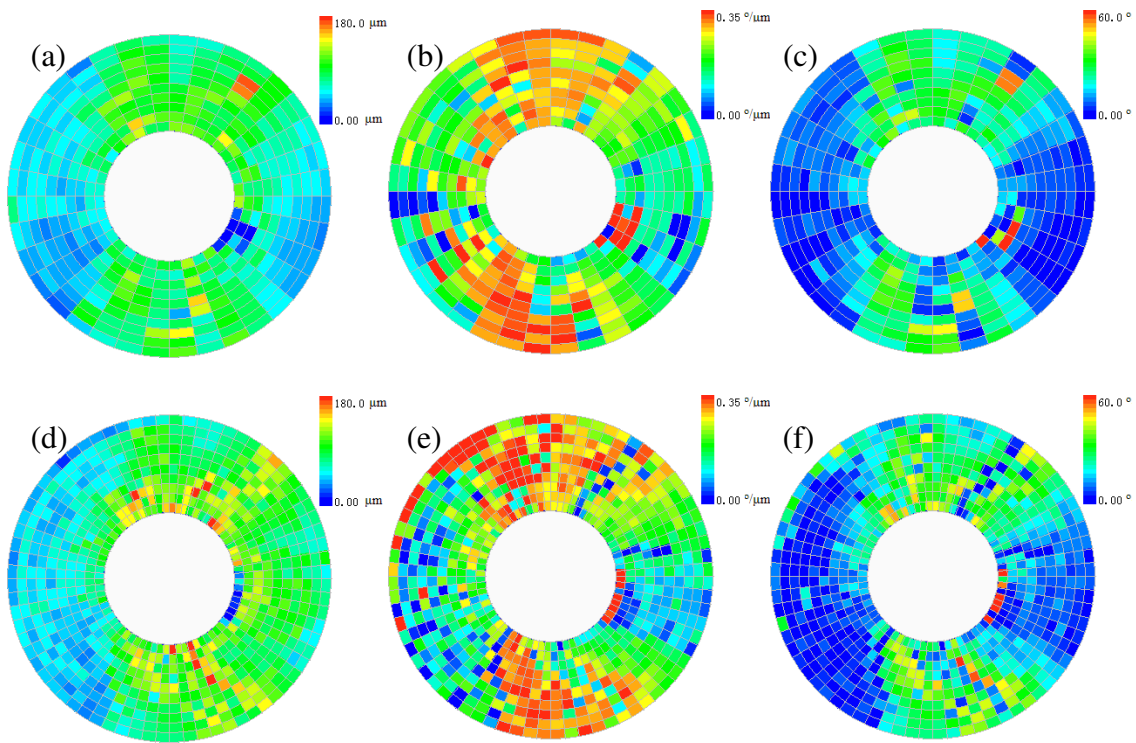


Figure 5.9: Influence of Cluster number. (a) thickness map (36 clusters per B-scan); (b) birefringence map (36 clusters per B-scan); (c) phase retardation map (36 clusters per B-scan); (d) thickness map (72 clusters per B-scan); (e) birefringence map (72 clusters per B-scan); (f) phase retardation map (72 clusters per B-scan). B-scan number = 10 and Cluster size = 100 for all maps. All maps are acquired about the ONH with 2 mm inner ring diameter and 5 mm outer ring diameter.

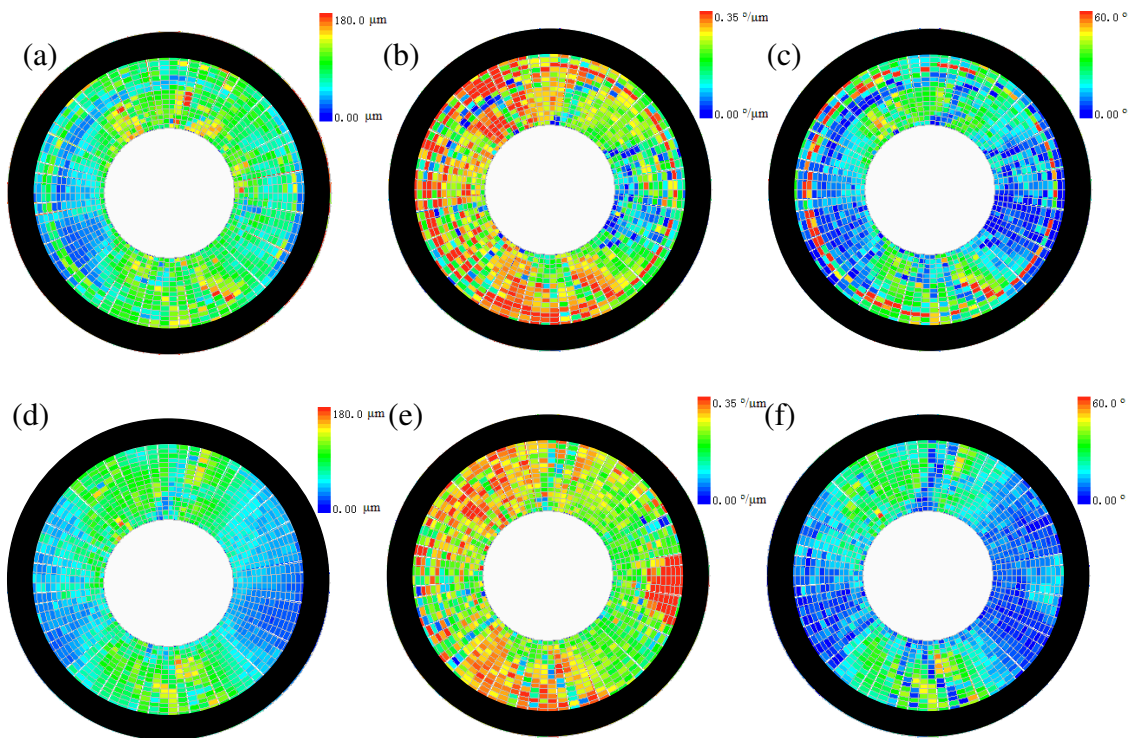


Figure 5.10: Influence of Cluster size. (a) thickness map (100 A-scans in each cluster); (b) birefringence map (100 A-scans in each cluster); (c) phase retardation map (100 A-scans in each cluster); (d) thickness map (50 A-scans in each cluster); (e) birefringence map (50 A-scans in each cluster); (f) phase retardation map (50 A-scans in each cluster). B-scan number = 20 and Cluster number = 80 for all maps. All maps are acquired about the ONH with 2 mm inner ring diameter and 5 mm outer ring diameter.

As figure 5.8 shows, little difference is observed in the map patterns utilizing different B-scan numbers since observation of abrupt changes as a function of distance from the center at the same angle is not expected. Figure 5.9 shows blood vessel patterns may be detected from phase retardation maps with greater cluster numbers, but processing time is doubled when number of clusters per B-scan increases from 36 to 72. In figure 5.10, outer rings are blacked out since the volunteer could not keep his/her eyes open for the duration of imaging time and multiple blinks occurred. A faster laser sweep speed would allow for denser scans without increase in acquisition time. No significant

difference was seen between 50 A-scans per cluster and 100 A-scans per cluster except in the temporal quadrant.

5.2.4 TSNIT Analysis for Clustered Thickness, Birefringence and Phase

Figure 5.11 depicts the variation of thickness as a function of angle. 72 clusters were acquired per ring for a total of ten concentric rings about the ONH. Each point represents the averaged thickness at the corresponding angle for all ten rings. The spread bars about each point represent the spread of thickness from all ten rings at corresponding angle. The retina was divided into four quadrants about the optic nerve head for further analysis: superior (S), inferior (I), temporal (T) and nasal (N). Superior and inferior quadrants are 120° each; nasal and temporal are 60° each. Figure 5.11b shows average thickness per quadrant with spread bars depicting variation in thickness for the ten concentric rings. The RNFL is thicker in the superior and inferior quadrants (Figure 5.11). As the RNFL is thicker in the superior and inferior regions, the distribution of blood vessels is denser in those areas, as shown by the clustered thickness map with overlaid blood vessels (Figure 5.12).

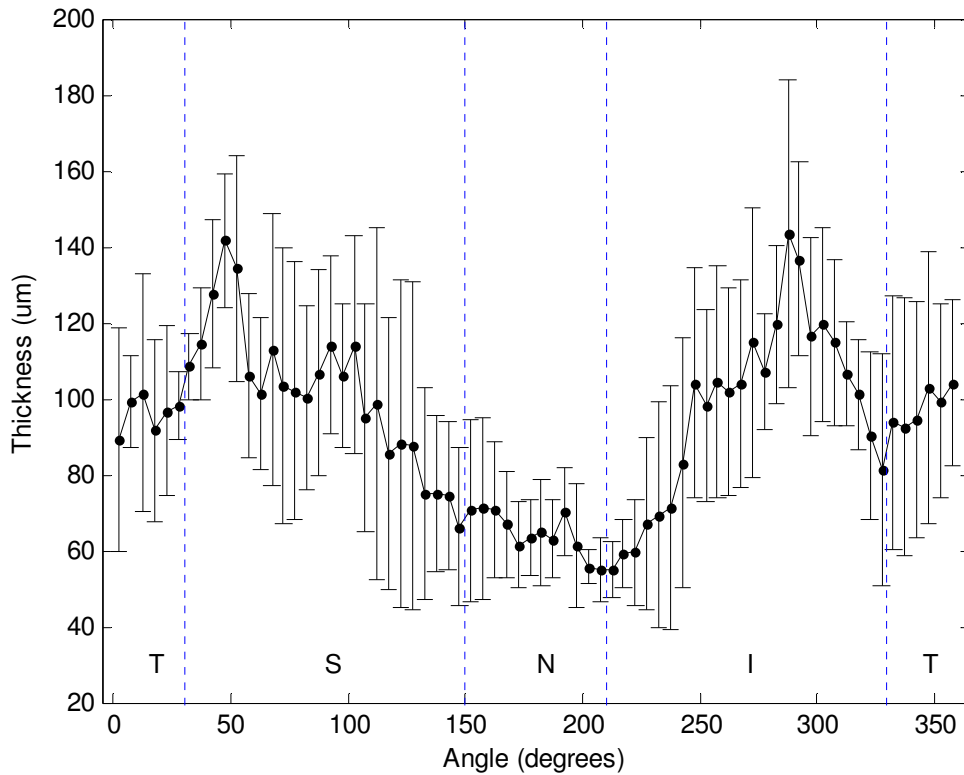


Figure 5.11: RNFL thickness (μm) in different retinal regions of a healthy patient's left eye (OS). Curve shows the relationship between averaged thickness and angular position starting at the temporal region and rotating in a counter-clockwise fashion. Spread bars represent the thickness spread across the ten rings at the same angle.

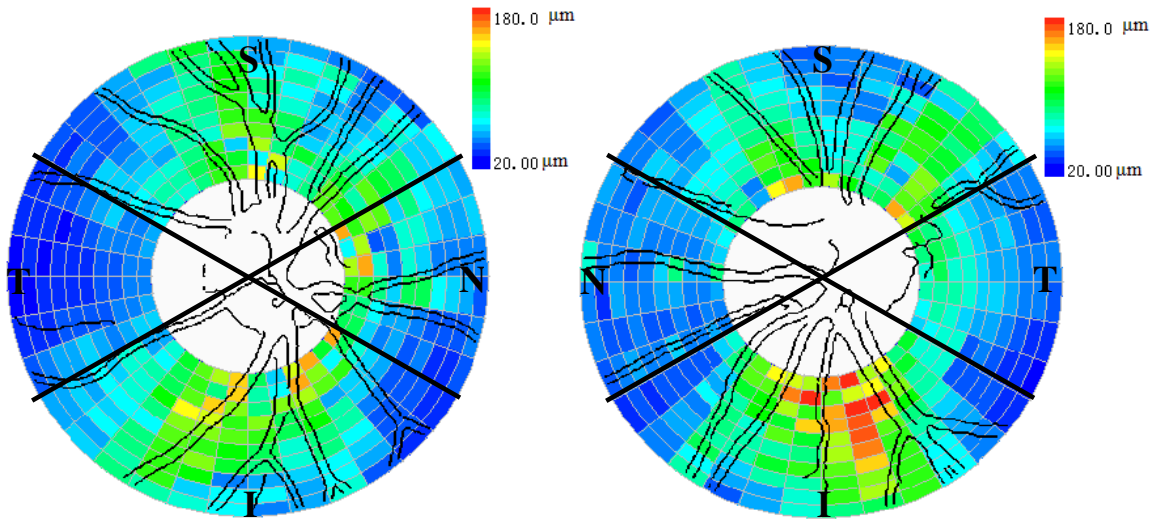


Figure 5.12: Clustered thickness maps with superimposed blood vessels detected from raster scans. Left: right eye (OD) (colorbar: 0 μm – 180 μm). Right: left eye (OS) (colorbar: 0 μm – 180 μm). In superior and inferior regions, RNFL is thicker and blood vessels are denser.

Birefringence properties of different retinal areas were studied in a similar manner as thickness. The averaged birefringence data, represented at phase retardation per unit depth, also shows a non-uniform distribution of birefringence in the retina as a function of angle about ONH (figure 5.13). Since the RNFL birefringence is related to the RGC neurotubule density, the distribution of birefringence may represent the density of neurotubules in different areas.

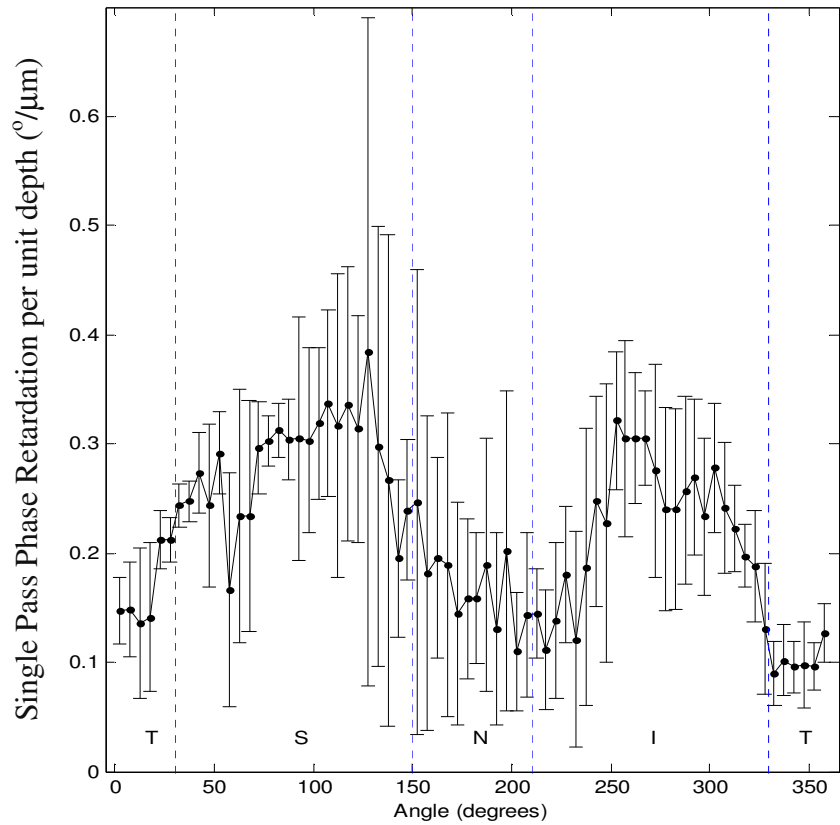


Figure 5.13: Birefringence ($^{\circ}/\mu\text{m}$) in different retinal regions. Curve shows the relationship between single pass phase retardation per unit depth and angular position. Spread bars represent the birefringence spread across the ten rings at the same angle.

The phase information is calculated by dividing measured single pass phase retardation per unit depth by measured thickness. Phase retardation is non-uniformly distributed in the retina as a function of angle about ONH (figure 5.14).

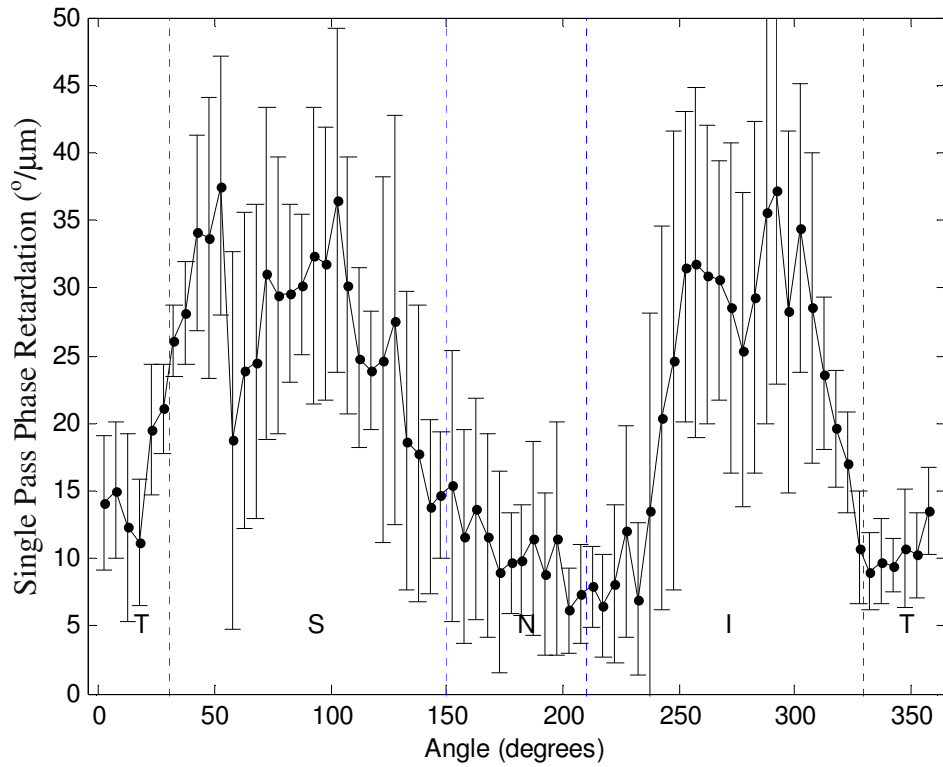


Figure 5.14: Phase retardation ($^{\circ}$) in different retinal regions. Curve shows the relationship between single pass phase retardation and angular position. Spread bars represent phase retardation spread across the ten rings at the same angle.

5.4 UNCERTAINTY IN MEASURED BIREFRINGENCE

During Stokes fitting, uncertainty is calculated for each cluster as a measure of fitting quality. Uncertainty values of each cluster are plotted on clustered maps as shown in figure 5.15. Uncertainty maps can help identify clusters with unreliable fits. These clusters may be removed from further study.

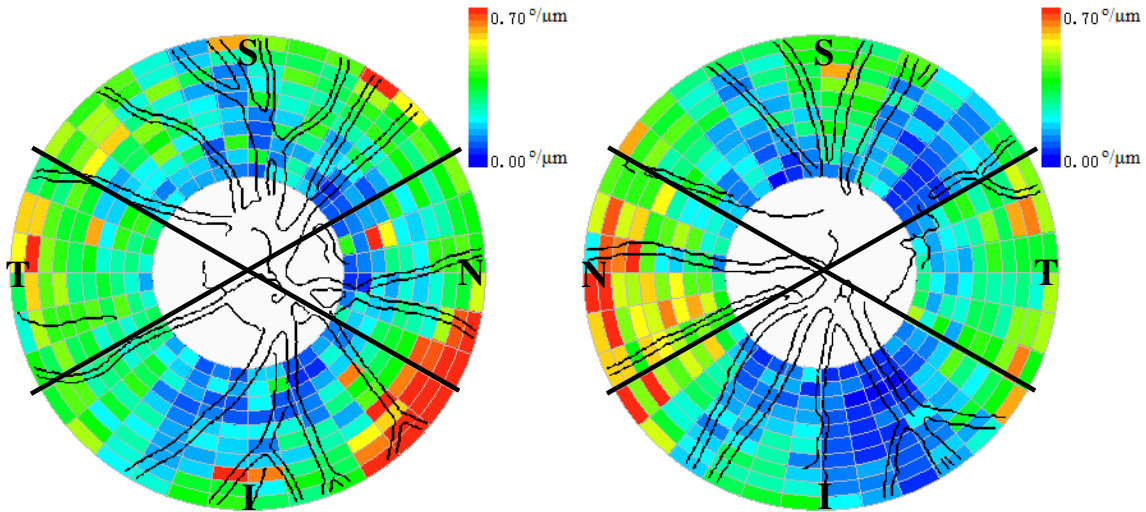


Figure 5.15: Uncertainty maps with blood vessels for both eyes. Left: OD (right eye). Right: OS (left eye).

Quality of fits on the Poincare sphere is greatly dependent on the number of depth data points used in the fit. The more depth points used in Stokes fitting the lower uncertainty is, as can be seen from figure 5.16. Figure 5.16a shows a Poincare sphere model of an RNFL $44\mu\text{m}$ thick, which has a single pass phase retardation of 2.925 degrees, 13.38 degrees per $100\mu\text{m}$, and 0.21 degree per $100\mu\text{m}$ uncertainty ($\pm 1.57\%$). Figure 5.16b shows a Poincare sphere result of an RNFL $138\mu\text{m}$ thick, which has a single pass phase retardation of 22.85 degrees, 33.02 degrees per $100\mu\text{m}$, and 0.08 degree per $100\mu\text{m}$ uncertainty ($\pm 0.24\%$). Uncertainty values are much lower for the thicker RNFL cluster; however both uncertainties are sufficiently low.

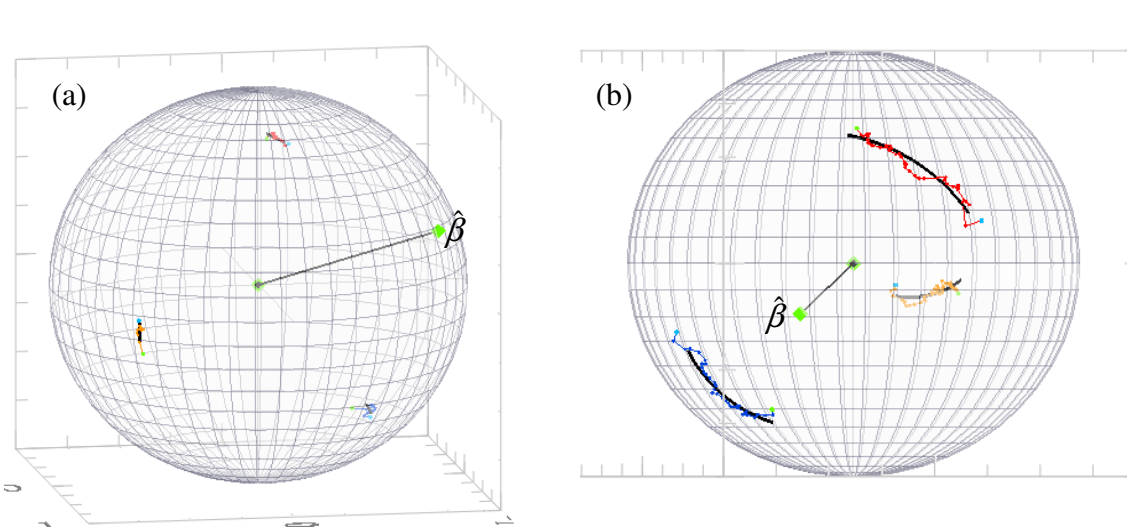


Figure 5.16: Poincare sphere model of (a) 44 μm thin RNFL cluster ($\pm 1.57\%$ birefringence uncertainty) and (b) 138 μm thick RNFL cluster ($\pm 0.24\%$ birefringence uncertainty).

In inferior and superior quadrants where the RNFL is thick, fitting uncertainty is low, but in temporal and nasal regions where the RNFL is thin, fitting uncertainty is higher. Comparison of uncertainty in different regions is shown in figure 5.17. Also, uncertainty normally increases at retinal locations near blood vessels, especially in the temporal and nasal regions. In the temporal and nasal regions, blood vessels are shallow in the RNFL and shadow laser power, preventing the PS-OCT system from accurately acquiring data.

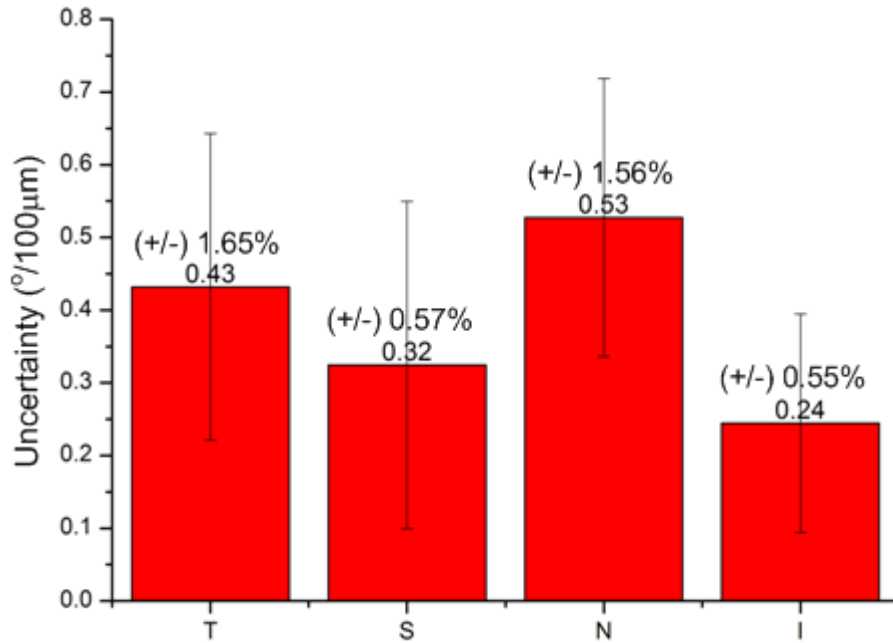


Figure 5.17: Comparison of absolute uncertainty in different regions in retina. Lower values are for average uncertainty per quadrants in degrees per 100 microns. Upper values are average percentage error in birefringence measurement. Spread bars represent uncertainty spread in different clusters per quadrant.

5.3 OPTICAL AXIS MAPS

5.3.1 Overview

Direction of the optical axis in the retina is of interest to ophthalmologists and vision science investigators. The optical axis correlates to structural properties of nerve fibers in the RNFL. For each cluster, during Stokes fitting, we obtain an Eigen axis (optical axis), which is described by a point on the Poincare sphere. The optical axis is a 3-D Stokes vector (Q_{axis} , U_{axis} , V_{axis}). Because direction of the optical axis on the fundus

can be considered 2-D, conversion from the 3-D optical axis on the Poincare sphere to 2-D optical axis direction is needed.

Transformation from 3-D Stokes vector to 2-D is described in figure 5.18. 3-D optical axes from all clusters in a B-scan are plotted on the Poincare sphere. Each optical axis is represented by a point on the surface. The set of all optical axes from each B-scan in the ideal case forms a plane. A multiple linear regression model is constructed to fit a plane according to the computed optical axes. A coordinate transformation is applied so that the fitted plane is contained to the QU plane. The process of coordinate transformation will be described in the following section. Finally, all points on the sphere surface are projected onto the QU plane, forming the transformed optical axis on the QU plane.

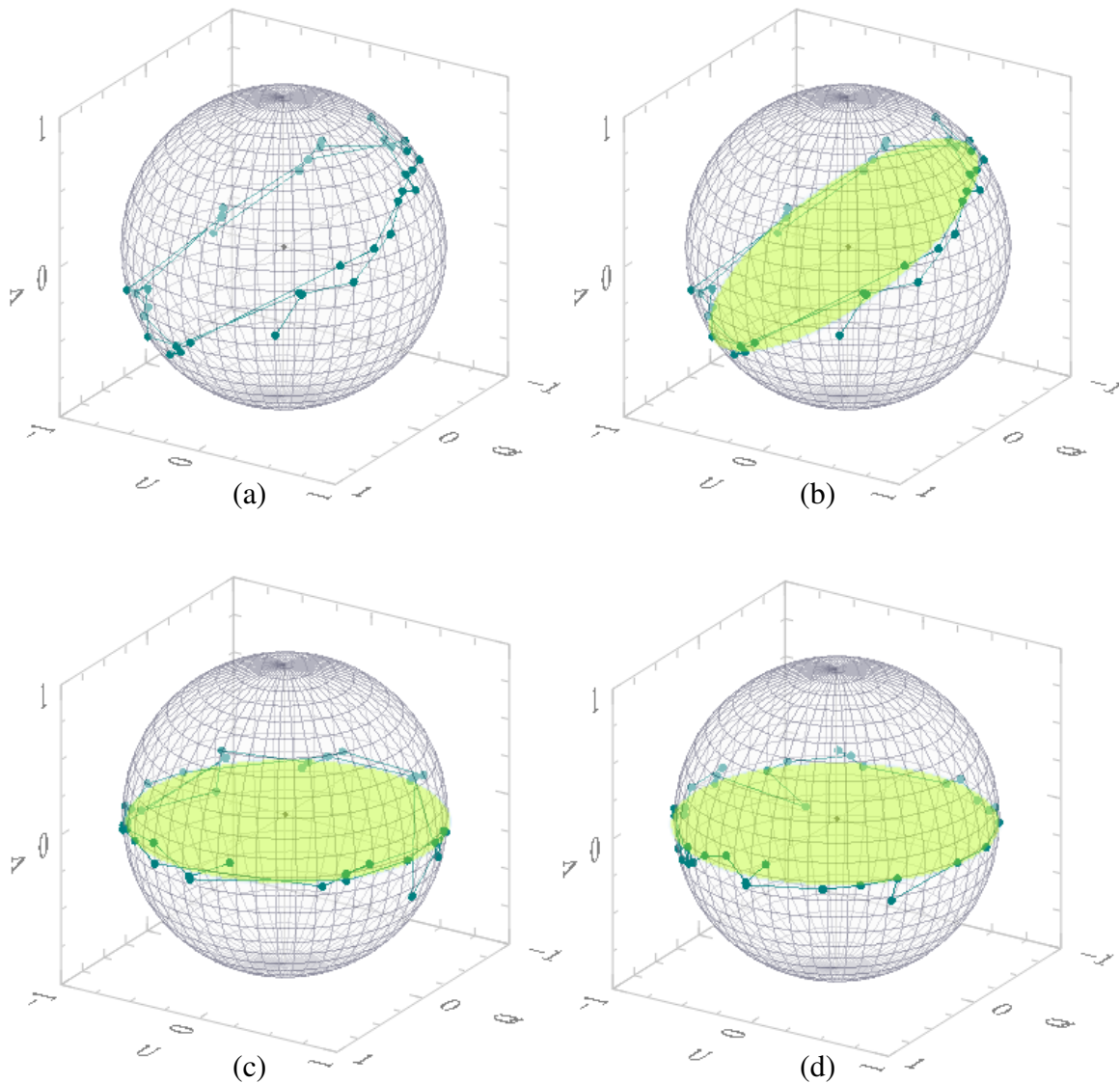


Figure 5.18: Finding optical axis position in a Poincare sphere. (a) The optical axes of 36 clusters per B-scan plotted as points on the Poincare sphere surface. (b) Plane fit to the 36 clusters by a multiple linear regression model. (c) The fitted plane rotated to the QU plane using Euler's rotation theorem. (d) For each point, the azimuthal angle divided by two so that the optical axes forms one ring in the QU plane. The position of the optical axis in the retina can be calculated from the azimuthal angle of points on the QU plane.

5.3.2 Euler's Rotation Theorem

The process of coordinate transformation includes an Euler's rotation, which rotates the coordinates of optical axis points on the Poincare sphere to new coordinates that are distributed around the UV plane. An Euler's rotation has three steps. First, data is rotated with angle α about the V axis in the QUV coordinate system. Then, rotated with angle β about the new Q axis, and finally, rotated with angle γ about the new V axis.

The Euler's rotation matrix is:

$$R = \begin{pmatrix} \cos \alpha & \sin \alpha & 0 \\ -\sin \alpha & \cos \alpha & 0 \\ 0 & 0 & 1 \end{pmatrix} \cdot \begin{pmatrix} 1 & 0 & 0 \\ 0 & \cos \beta & \sin \beta \\ 0 & -\sin \beta & \cos \beta \end{pmatrix} \cdot \begin{pmatrix} \cos \gamma & \sin \gamma & 0 \\ -\sin \gamma & \cos \gamma & 0 \\ 0 & 0 & 1 \end{pmatrix} \quad (5.1)$$

Any point $P = \begin{pmatrix} x \\ y \\ z \end{pmatrix}$ in the original coordinate system will be rotated to a new

coordinate $P' = P \cdot R$ in the new coordinate system after Euler's rotation.

For the optical axis calculation, we first set the plane formed by the optical axis points on the sphere surface, and then we used the normal vector to represent the direction of the plane. We then rotated the unit normal vector (x_N, y_N, z_N) to a new coordinate $(0, 0, 1)$ after applying Euler's rotation so that the plane would be parallel with the QU plane. To do so, we used the following relations:

$$\begin{aligned} \cos \alpha &= \frac{y_N}{\sqrt{x_N^2 + y_N^2}}, & \sin \alpha &= \frac{x_N}{\sqrt{x_N^2 + y_N^2}} \\ \cos \beta &= \frac{z_N}{\sqrt{x_N^2 + y_N^2 + z_N^2}}, & \sin \beta &= \frac{\sqrt{x_N^2 + y_N^2}}{\sqrt{x_N^2 + y_N^2 + z_N^2}}; \\ \cos \gamma &= 1, & \sin \gamma &= 0. \end{aligned}$$

After Euler's rotation, the optical axis is near the QU plane, as shown in Figure 5.17c.

5.3.3 Offset Compensation in Optical Axis Maps

Plotting the optical axis direction at each cluster forms the optical eigen-axis map. The optical axis map after coordinate transformation is shown in figure 5.19a. Physiologically, the direction of the optical axis should approximately form a radial pattern from the ONH, which is inconsistent with the optical axis map in figure 5.19a. This inconsistency exists because the absolute lab frame coordinates are not known due to random fiber transformation. A coordinate transformation rotates each optical axis to the QU plane, but the directions of the optical axis of each B-scan on the QU plane can have an offset. An offset algorithm rotates the optical axes about V on the Poincare sphere to generate offset values for each B-scan, compensating the optical axis direction so that they form a radial pattern. Two offset calculating strategies are developed and compared: rotation for each ring (figure 5.19b) and rotation for the whole map (figure 5.19c).

For the rotation of each ring approach, the compensation offset is defined as:

$$Offset_b = \frac{1}{A} \sum_{k=0}^A (\theta_{e,b,k} - \theta_{o,b,k}) \quad (5.2)$$

where $Offset_b$ is the compensation offset for the b^{th} B-scan, A is the number of A-scans in each B-scan, $\theta_{e,b,k}$ is the expected axis direction of the k^{th} A-scan in the b^{th} B-scan, and $\theta_{o,b,k}$ is the calculated axis direction of the k^{th} A-scan in the b^{th} B-scan. $\theta_{e,b,k}$ is determined from the physical position of the cluster, and $\theta_{o,b,k}$ is calculated from Euler's rotation theorem. After calculating the offset for each B-scan, the calibrated optical axis direction of the b^{th} B-scan is:

$$\theta_{c,b,k} = \theta_{o,b,k} + Offset_b \quad (5.3)$$

where $\theta_{c,b,k}$ is axis direction after offset compensation using each ring rotation strategy.

In the rotation of the whole map strategy, the compensation offset is defined as:

$$Offset = \frac{1}{AB} \sum_{j=0}^B \sum_{k=0}^A (\theta_{e,j,k} - \theta_{o,j,k}) \quad (5.4)$$

and the calibrated optical axis direction for any cluster is:

$$\theta_{c,j,k} = \theta_{o,j,k} + Offset \quad (5.5)$$

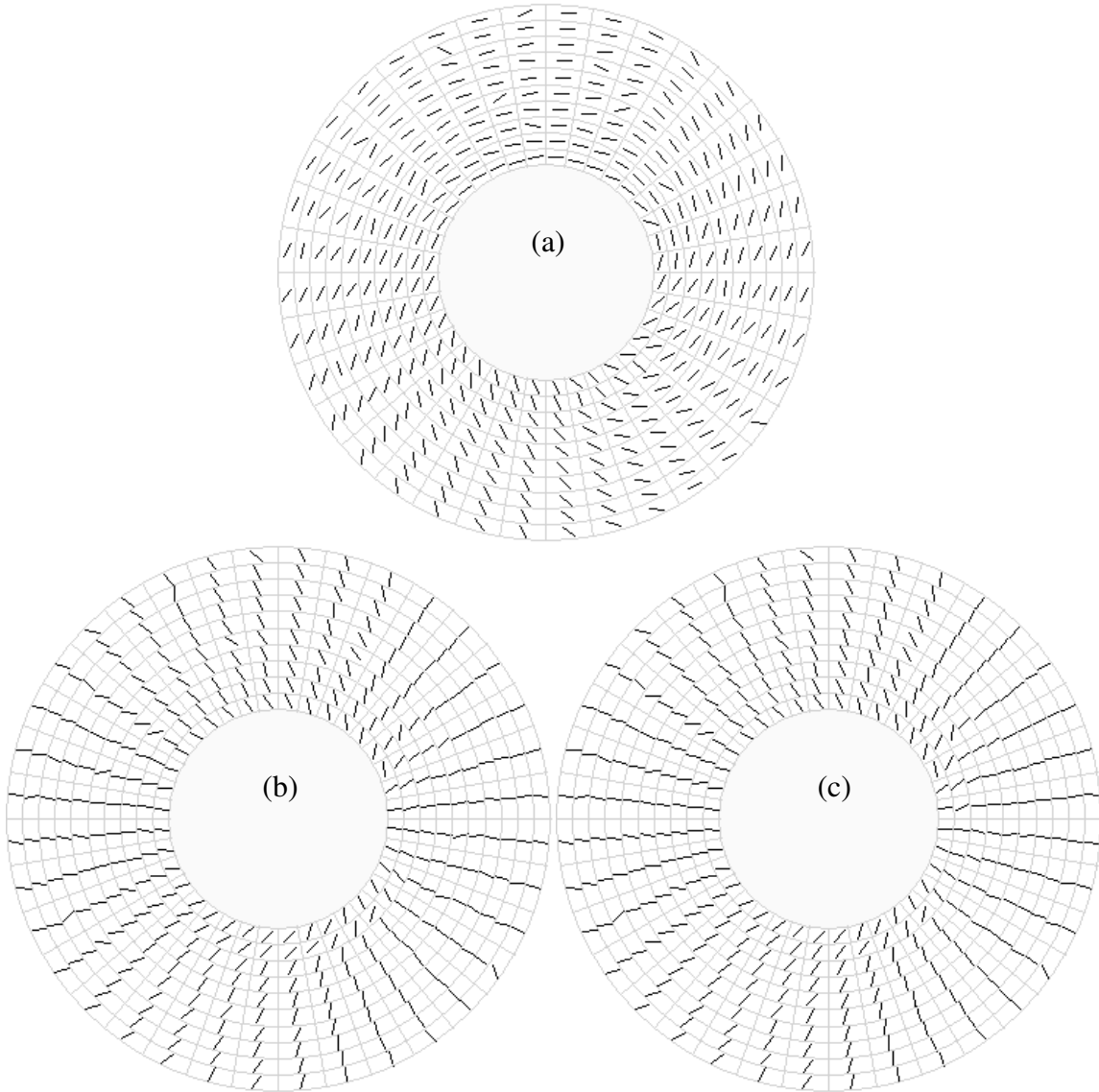


Figure 5.19: Optical axis maps. (a) Before offset rotation. (b) After offset rotation of each ring. (c) After offset rotation of the whole map.

The rotation of each ring strategy finds an optimal value, which minimizes the difference between expected optical axis direction which stems from the nerve fiber physiology and calculated optical axis direction for each B-scan, while the rotation of the whole map strategy finds an optimal value minimizing the difference for all of the clusters. The rotation of each ring strategy forms a better radial pattern than the rotation of the whole map strategy, but the rotation of the whole map method better compensates for outlier clusters. However, no significant difference exists between the optical axis maps generated by the two strategies. The justification for rotation of each ring should be looked at. One can argue that no real physical interpretation justifies rotation of each ring. One can motivate the rotation of the entire map though.

5.3.4 Optical Axis Map with Overlaid Blood Vessels

The optical axis maps with blood vessels are shown in Figure 5.20. Optical axes in the retina do not form perfectly radial patterns. This is perhaps because the direction of optical axes seems to point to the optic cup, not the center of the ONH as the optical axis maps show. However, during OCT measurements, ring scans were acquired peripapillary about the optic nerve head (ONH). Placement lies between the center from which nerve fibers spread (the optic cup) and the center for clustered ring scans (the center of the ONH). Since the axis map represents the direction that nerve fibers spread.

Blood vessels also affect optical axis map patterns. Optical axis direction tends to point to the center of the ONH cup in a similar fashion as blood vessels aggregate to a main vein and artery that travels down the optic nerve from the optic nerve head cup. In the case of clusters that overlap shallow blood vessels the optic axis pattern seems to deviate from the expected optic axis direction that is representative of the nerves

physiology. The reason may be due to the phase shift that is caused by blood flow. In areas where blood vessels are deep, this interaction is not significant and cannot be recognized from the optical axis maps, but when the blood vessels are near the surface of RNFL, the influence of blood vessels on nerve fibers cannot be neglected. A second reason may be due to the fact that blood vessels introduce higher estimation uncertainties and/or to failed fitting calculations due to a decrease in PSNR.

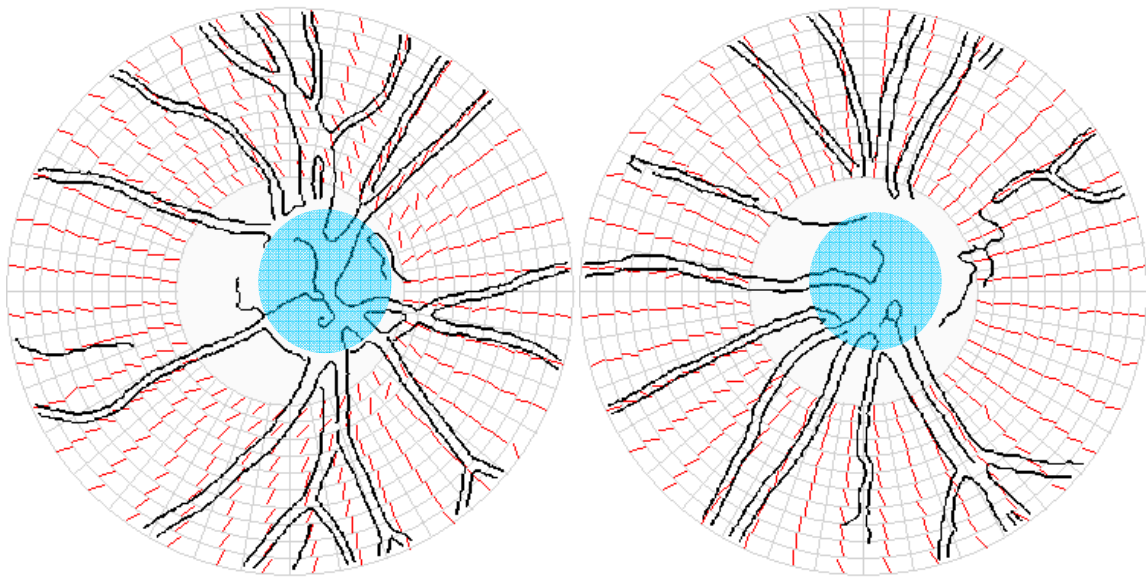


Figure 5.20: Optical axis map with blood vessels shows that the directions of optical axes are pointing to the center of the optic cup, which is indicated by the blue regions. Left: OD (right eye); Right: OS (left eye).

5.4 CONCLUSION, AND OUTLOOK

In this dissertation I have introduced a new technology for measuring RNFL thickness, birefringence, phase retardation, and optic axis: swept source polarization sensitive optical coherence tomography (SS-PSOCT). To demonstrate a system capable of providing accurate RNFL birefringence measurements, several technical challenges

had to be overcome. Controlling polarization state of light in single mode fiber is difficult, especially at 1060nm. This project was very ambitious, and although we were successful in obtaining accurate birefringence measurements, we recorded fringe data using one detection arm and were not able to perform balanced detection for the clustered data used in RNFL birefringence measurements. SNR was sufficiently high to record accurate RNFL phase retardation and birefringence maps without balanced detection since other system components were properly optimized and since measured sample (RNFL) is the first layer of the retina and deep light penetration is not required.

In conclusion, we were able to measure birefringence accurately. We also devised a method to measure eigen-axis in the retina using single mode fiber without having recourse to polarization maintaining fiber. However, we were not able to record repeatable birefringence measurements with balanced detection and had to use one detection arm for the measurement.

Two incident polarization states would suffice to get high accuracy fits as can be seen from figure 5.21. However in the case that one of the incident polarization states is same as the eigen-axis then the algorithm will not return reliable fits. Single-mode optical fiber and anterior segments of the eye are birefringent, however, a priori knowledge of optic axis information from a previous acquisition can drive the choice of polarization states to use such that in subsequent measurements only two states are needed and maximum separation (90 degree separation angle) between $P(0)$ and eigen axis is obtained.

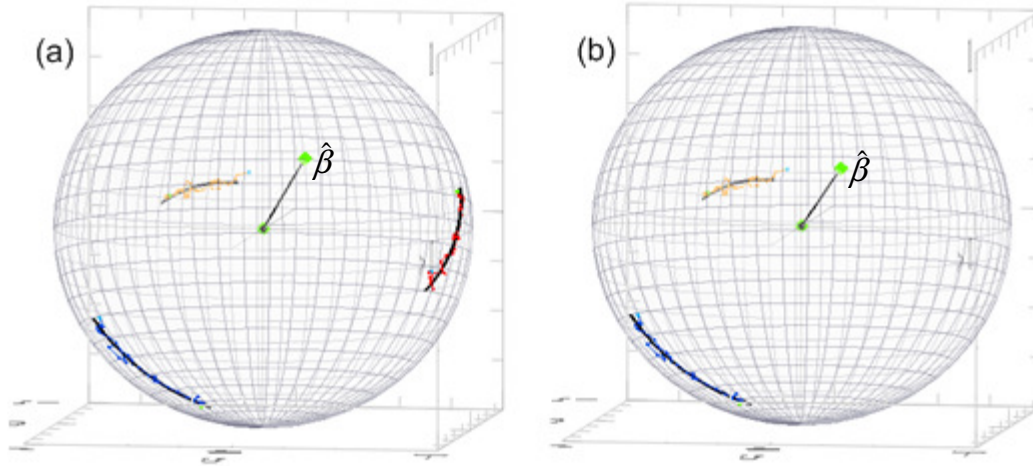


Figure 5.21: Noisy RNFL $S(z)$ arcs and their fits $P(z)$ for (a) 3 input polarization states, (b) 2 input polarization states. Results demonstrate that for high PSNR two states are sufficient even when the two chosen states provide less than optimal separation between $P(0)$ and eigen axis $\hat{\beta}$.

72 clusters per ring can be used instead of 36 clusters per ring in order to better map retinal birefringence. Ideally, one would want to use a variable number of A-scans per cluster depending on imaged quadrant, and use as many clusters per B-scan so as to cover the entire retinal angles about the ONH. Number of B-scans could be kept at 10 since no abrupt change happens in the radial dimension. Total acquisition can still be kept short at about 3 seconds with all the optimized acquisition schemes discussed.

Since we were not consistently able to record accurate SS-PS-OCT data with the fiber splitter in balanced mode, use of a bulk beam splitter could provide the solution (figure 5.22). Moreover, placing a polarizer after the reference arm and before the bulk splitter will guarantee that the H over V ratio will be equal to one for the whole spectrum for the three polarization states. The dispersion introduced by the polarizer however will need to be minimized and or compensated in the sample path of the interferometer unless a sheet polarizer is used instead.

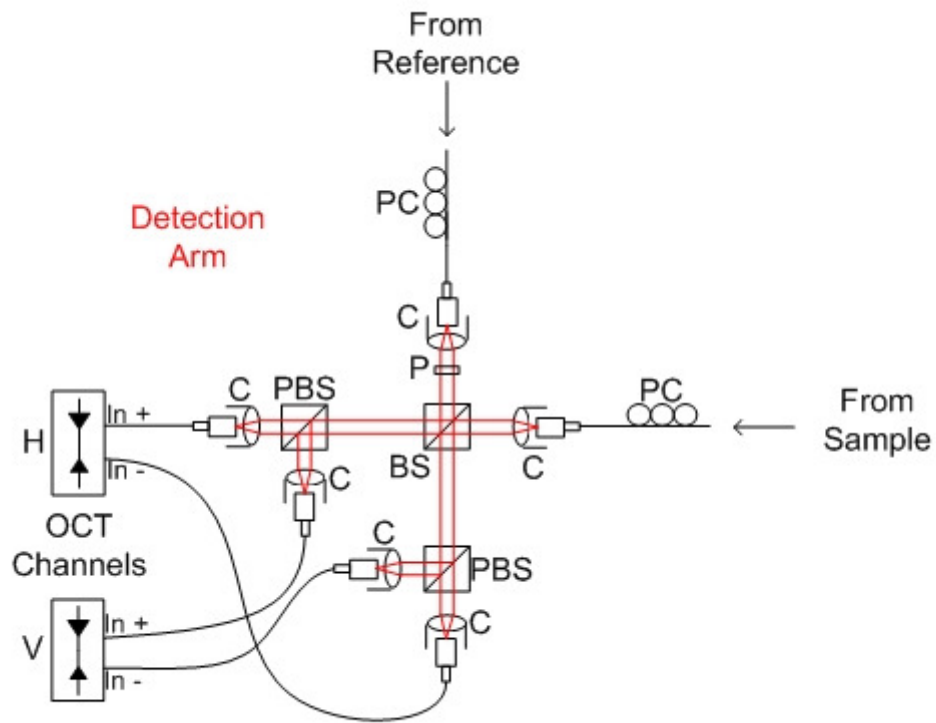


Figure 5.22: Proposed detection arm setup. P: sheet polarizer, BS: 50/50 bulk beam splitter, C: collimator, PC: polarization controller, PBS: polarization beam splitter.

Appendices

APPENDIX A POLARIZATION MODE DISPERSION

To achieve accurate birefringence results presented in this dissertation we completed two iterations of PS-OCT instrument design, construction and testing. The first PS-OCT instrument's optical components were arranged on an optical breadboard. The system was built with long fiber segments that contained many tight fiber bends. Using this instrument, balancing reference arm H and V intensity was inconsistent, and birefringence measurements were not repeatable. The system was later placed on a cart. In placing the instrument on the cart, most of the optical fiber was tightly looped and manual polarization controllers in the detection arm were replaced by dynamic polarization controllers (DPC). After replacing manual polarization controllers, the system could no longer measure birefringence since it was impossible to make the reference arm's horizontal and vertical signals equal in amplitude throughout the spectrum of the swept laser source. These observations prompted us to investigate the cause of the spectrally dependent variability that was attributed to polarization mode dispersion (PMD). Results of PMD measurements on fibers in different polarization controllers are discussed in later.

After we discovered sources of PMD in PS-OCT instrumentation, we completely rebuilt the fiber interferometer, taking precaution to minimize PMD. In this second PS-OCT instrument, no discernable delay was detected between the two polarizations (figure A.1), which indicates that PMD was low.

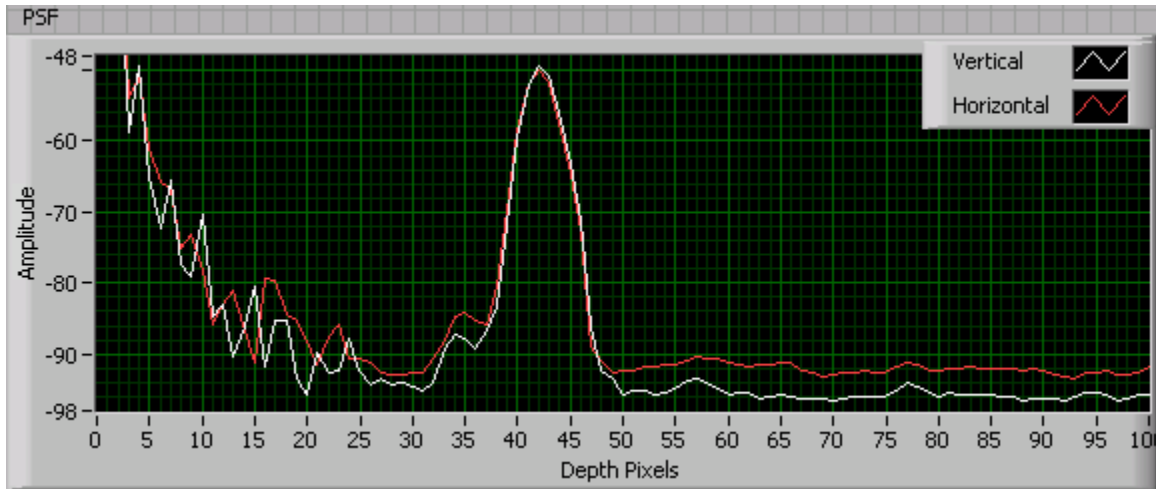


Figure A.1: PSF showing no delay between horizontal and vertical polarization detection channels. Amplitude is in dB logarithmic scale.

Two commercial dynamic polarization controllers (DPC) (PCD-M02, by General Photonics) were acquired, one for each detection arm. LabView Virtual Instrument (VI) was written to control the solenoids used to block either of the two detection arms. By blocking one detection arm, signals from the other detection arm can be acquired using the same balanced detectors. Using digital outputs of the PCIe 6259 DAQ card, we sent control signals to the DPC to control the amount of piezo-stress on the DPC for the unblocked arm. The DPC was driven in order to equalize horizontal and vertical amplitudes. Even though this method was automated, fast, and only needed to be repeated each time the system was turned on, it was soon abandoned, and the DPC was replaced by manual polarization controllers. Using the DPC H and V were only equalized for the three polarization states at the source center wavelength but were very different for the rest of the spectrum since stressing the fiber by the DPC introduced substantial amount of PMD.

To test for sources of PMD, the following experimental setup was devised. Light from a swept source laser was propagated through the fiber under test (with different

polarization controllers), and then collimated in free space using a fiber collimator (ThorLabs PAF-X-7-NIR). Light was then propagated through a Wollaston prism bulk beam splitter to decompose light into horizontal and vertical components. Each light beam was then focused using a microscope objective lens to a 200 KHz photoreceiver (2011-FS, by NewFocus). Horizontal and vertical channels were recorded and each normalized to unity. Difference of the two signals was divided by the sum and multiplied by two. This result was then multiplied by a hundred to obtain a percent polarimetric variation (PPV) curve given by:

$$PPV_i = 100 \cdot \left(2 \cdot \frac{\bar{H}_i - \bar{V}_i}{\bar{H}_i + \bar{V}_i} \right)$$

A weighted RMS value to describe the non-uniformity across the spectrum was measured using the following equation:

$$RMS_w = 2 \cdot \sqrt{\sum \left\{ \left[\frac{\bar{H}_i - \bar{V}_i}{\bar{H}_i + \bar{V}_i} \right]^2 \cdot (H_i + V_i) \right\}}$$

where $\bar{H}_i = \left(\frac{H_i}{\sum H_i} \right)$, and $\bar{V}_i = \left(\frac{V_i}{\sum V_i} \right)$. The RMS values are tabulated in Table A.1. It

is evident from the results that HI1060 FLEX introduced less PMD than HI1060 and that the large type paddles were the right choice for polarization control. We, however, built our system using HI1060 fiber since no off the shelf HI1060 FLEX fiber components were available. In order to keep PMD low we used the large type polarization paddles and kept their number to a minimum.

Table A.1: Non-linearity RMS value for all tested setups

Unit Under Test	Non-linearity RMS value
4m HI1060 fiber with large paddles	1.16
4m HI1060 FLEX fiber with large paddles	0.90
4m HI1060 FLEX fiber with small paddles	1.23
4m HI1060 FLEX fiber with polarite	1.29
25m HI1060 FLEX fiber with large paddles	6.16

Ideally, in the absence of PMD and interference between the two propagating principal states of polarization, the curve of percent polarimetric variation as a function of wavelength should be constant at zero. If there is a fixed amount of retardation as a function of wavelength then the curve will oscillate and will no longer be zero.

To test the effect stress has on PMD; we used a 4m length of HI1060 FLEX fiber in two configurations. In the first configuration, the fiber is passed through a manual polarization controller (Polarite, by General Photonics) that modifies polarization state of light by twisting a segment of fiber and by placing compressive stress along one axis of the fiber. In the second configuration, a manual polarization controller (FPC560, by Thorlabs Inc) that introduces loops in the fiber in three consecutive paddles and modifies the polarization state of light by rotating the paddles. Polarization controllers with larger diameter paddles were used (2.5 inch diameter). Figures A.2 and A.3 show that stress introduced by the Polarite polarization controller significantly increased PMD in the fiber.

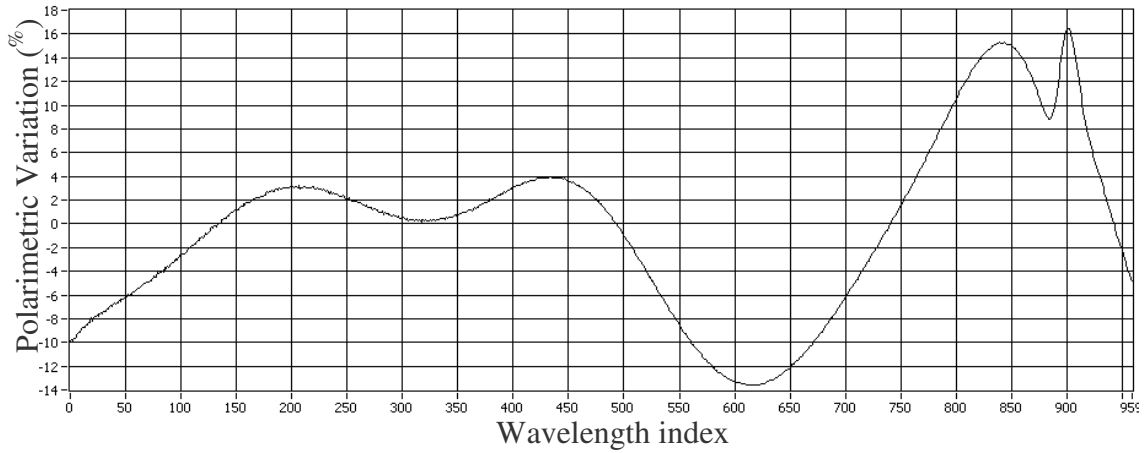


Figure A.2: Nonlinearity curve using 4m HI1060 FLEX with the Polarite polarization controller

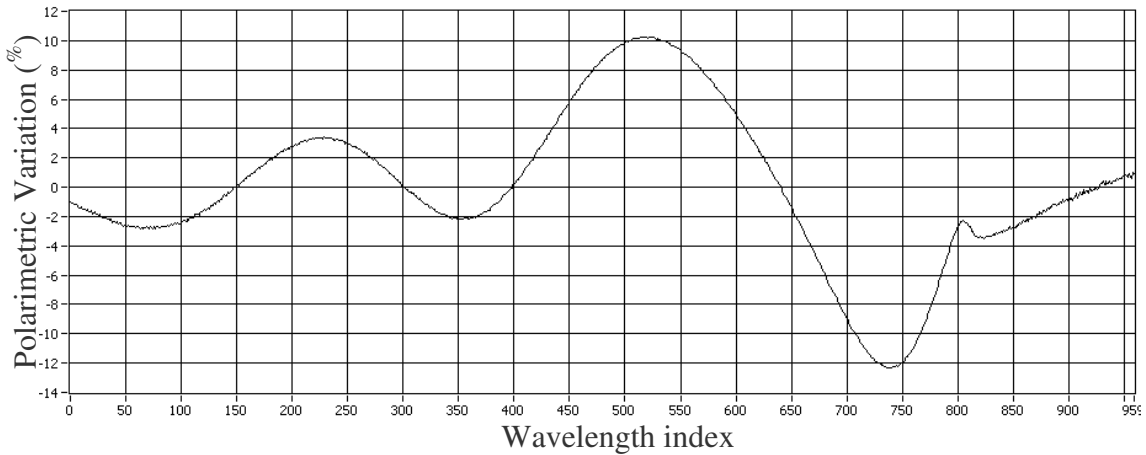


Figure A.3: Nonlinearity curve using 4m HI1060 FLEX with the large paddles type polarization controller

To show the effect fiber length has on PMD, we compared a 4m HI1060 FLEX fiber segment using the larger paddle type polarization controller to a 25m HI1060 FLEX fiber using the same polarization controller. The results from figures A.5 and A.6 show that fiber length has a significant effect on the amount of PMD, which is why the total optical fiber length of the reference and sample arms in the second iteration of the SS-PSOCT system were kept to less than three meters each.

Fiber bends were also suspected to have a significant effect on PMD, so we tested the same 4m HI1060 FLEX fiber with the paddle type polarization controller, except that the paddles' diameter was 1 inch (FPC030, by General Photonics) and compared to the measurement acquired with the larger type paddles. Comparing the results from figure A.4 to those from figure A.5, we notice that small bend radii introduce significantly more PMD.

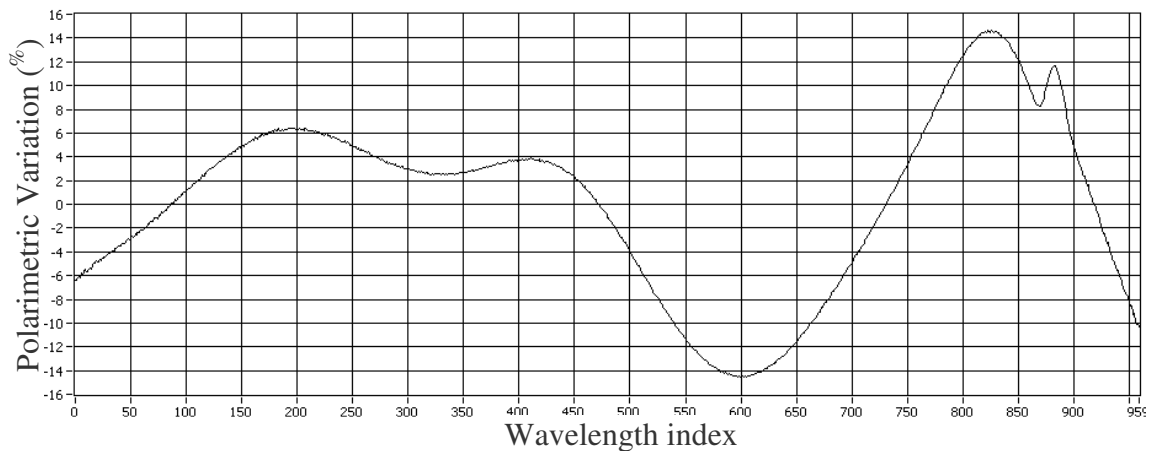


Figure A.4: Nonlinearity curve using 4m HI1060 FLEX with the small paddles type polarization controller

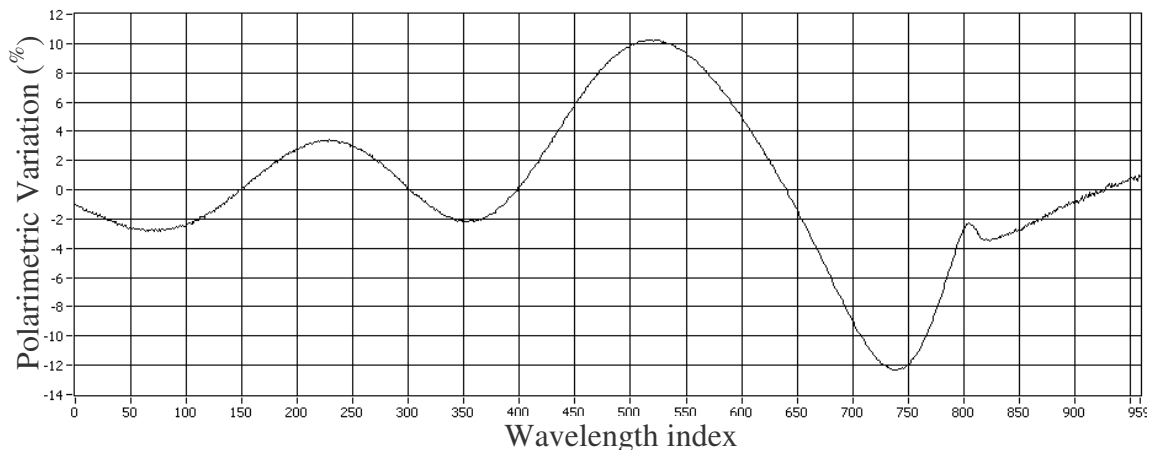


Figure A.5: Nonlinearity curve using 4m HI1060 FLEX with the large paddles type polarization controller

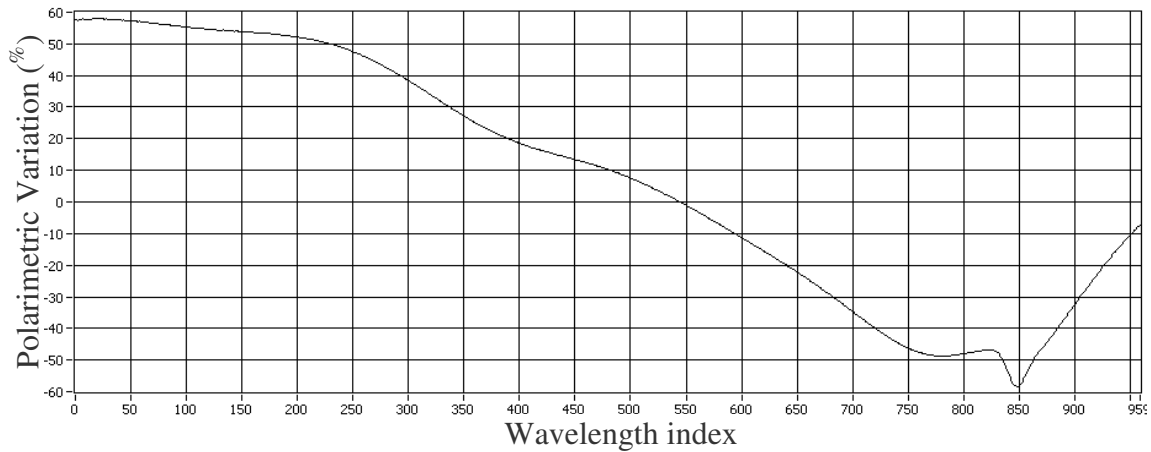


Figure A.6: Nonlinearity curve using 25m HI1060 FLEX with the large paddles type polarization controller

Corning does not supply data on PMD for their HI1060 or HI1060 FLEX fibers but advertise that HI1060 FLEX exhibits lower PMD. We tested the two kinds of fiber with the same length and using a polarization controller with large paddles. For the 4m lengths studied, we found that the difference in PMD between the two fiber types was small. Results are shown in figures A.7 and A.8.

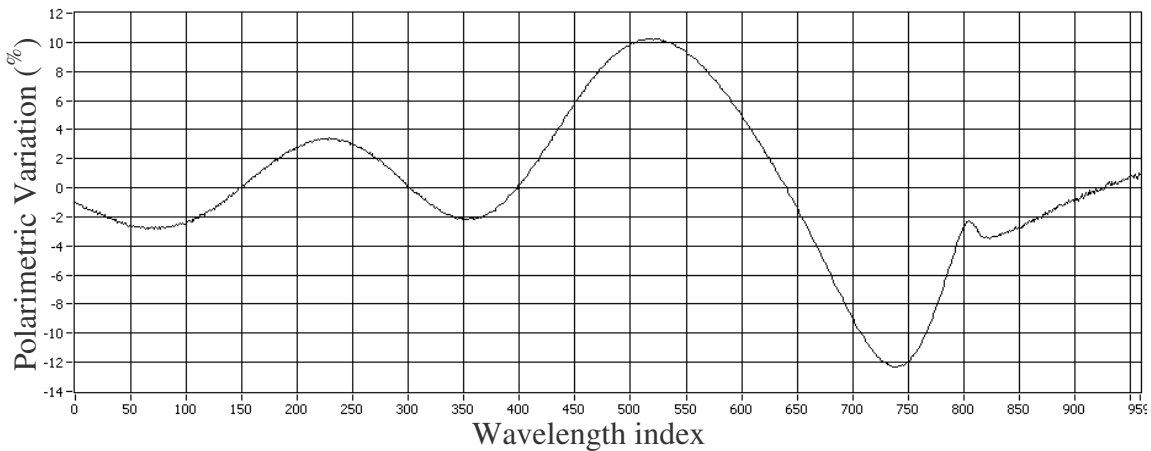


Figure A.7: Nonlinearity curve using 4m HI1060 FLEX with the large paddles type polarization controller

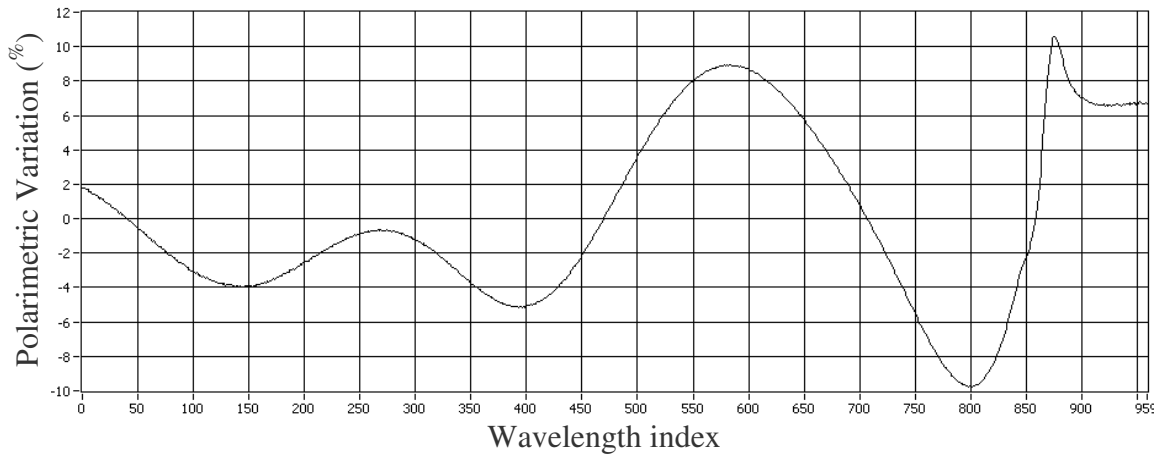


Figure A.8: Nonlinearity curve using 4m HI1060 with the large paddles type polarization controller

In summary it has been concluded that HI1060 FLEX fiber would be better to use than HI1060 fiber while maintaining fiber dimensions to a minimum and avoiding any stress or tight bends on the fiber. We used HI1060 fiber since off the shelf components that use HI1060 FLEX are not readily available.

APPENDIX B: EFFECT OF H AND V BALANCING ON POLARIMETRIC MEASUREMENTS

To test for the effect of H and V balancing we set up a test to image a birefringent film. In the first test we acquired data with balanced detection, and then we blocked one arm at a time to acquire data with each arm individually (without balanced detection). In order to rule out the potential effect of the detectors, we repeated the measurements by swapping fibers at the detectors. Results confirmed that birefringence measurements were only accurate for one detection arm regardless of which detector was used.

To test for the effect of sample arm polarization state, we repeated the measurement with one arm at a time; once with the sample arm fiber in the original, natural position and then with the sample arm fiber intentionally bent and twisted. The results showed that the sample arm did not have any effect except for changing the position of the eigen-axis on the Poincare sphere as long as no additional PMD was introduced.

We made three measurements of birefringence from the birefringent film with a different setup each time. Using the good arm we first measured with V and H equalization optimized (figure B.1a), then we slightly misaligned the coupling back to fiber at the good detection arm to make the ratio less than unity, while keeping the ratio uniform across the spectrum (figure B.1b), and finally we measure with un-optimized H and V (figure B.1c). We concluded that it is important to have V over H ratio equal to unity, and that a uniform ratio across the whole spectrum is critical. Applying a ratio correction to the data post-processing did not help improve results but rather just introduced a slight decrease in PSNR. Further study will need to be performed to quantify how much error is introduced in estimation of polarimetric properties when V

and H are not equalized. Knowledge of actual V and H values may be investigated to see if a correction in Stokes space may be implemented.

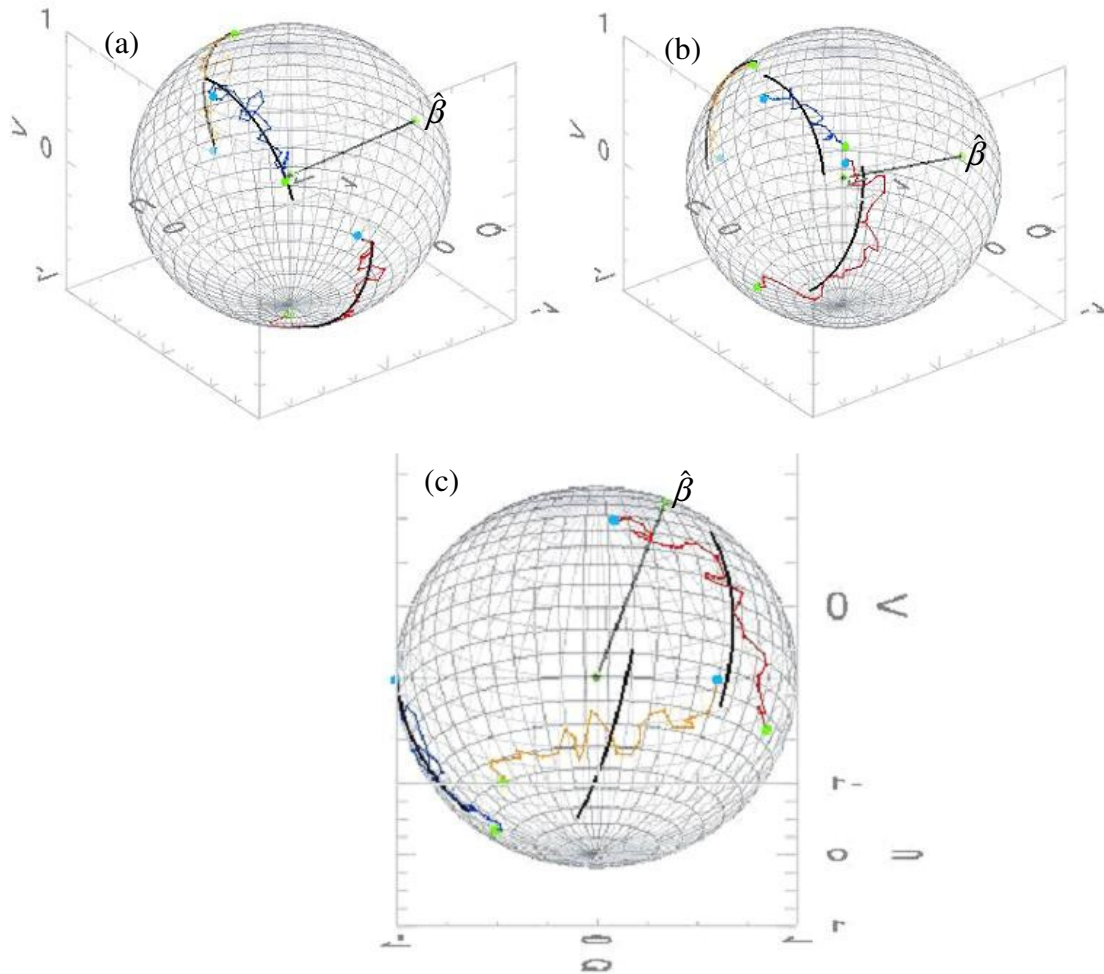


Figure B.1: Arcs and their fits for the same birefringent film and with all parameters kept the same except for the V/H ratio. (a) V/H ratio optimized and fits appear accurate. (b) V/H uniform but not unity and the fits look somewhat inaccurate. (c) V/H not uniform and not unity and the fits look inaccurate.

APPENDIX C DIGITIZER PHASE ERRORS

An assumption in constructing the PS-OCT instrumentation is that both horizontal and vertical polarization channels are acquired simultaneously. However, we noticed that some digitizers manufactured by Alazaar can introduce a phase delay between the channels. In discussions with the manufacturer, two reasons were identified for the observed phase delay. The FPGA on the digitizer was using a different clock signal for each acquisition channel and introducing a phase delay between A/D channels. Second, the A/D chips on the board work properly with a uniform temporal acquisition, but as discussed in Chapter 2, acquisition in the SS-PSOCT instrument must be linear in k -space, hence non-uniform in time.

The source of phase delay between the two acquisition channels results from the A/D attempting to compensate for a non-uniform frequency clock. Each A/D on the Alazaar card can compensate differently, thus introducing a relative time delay between the two channel acquisitions. The phase delay was a substantial problem for another PS-OCT system constructed in our laboratory since the phase error changed substantially and was unpredictable. In the PS-OCT system described here, we imaged reflection from a silver mirror and measured the phase delay between horizontal and vertical channels. Phase difference was measured to be less than 2 degrees and stayed constant for the course of several measurements of different durations.

Eventually, in collaboration with Alazar, these two issues were overcome. New firmware was placed on the FPGA, and the two acquisition channels shared one clock signal. The phase locked loop that was used for compensation was disabled to overcome the card attempting to correct for perceived jitter.

APPENDIX D RELATIVE INTENSITY NOISE

In the SS-PS-OCT system, we use a swept laser source that uses a tunable filter (grating and polygon mirror) to sweep a narrow 0.1nm FWHM line-width laser across the spectrum wavelengths. In this process the available longitudinal cavity modes compete with each other as the filter is tuned and give rise to mode-hopping, the principal source of relative intensity noise (RIN). Balanced detection reduces swept laser source RIN as well as the DC component of the signal, which preserves dynamic range.

All data presented in Chapter 5 used the laser prior to an upgrade that had substantially lower RIN making it possible to image without balanced detection. The upgraded laser exhibited greater intensity noise possibly because a different semiconductor optical amplifier (SOA) is driven with greater currents (figure D.1). The upgraded laser output provided a power that was 2.5 times that before the upgrade. Since the upgraded laser provides higher power, balanced detection becomes important to obtain sufficient SNR for recording accurate birefringence images.

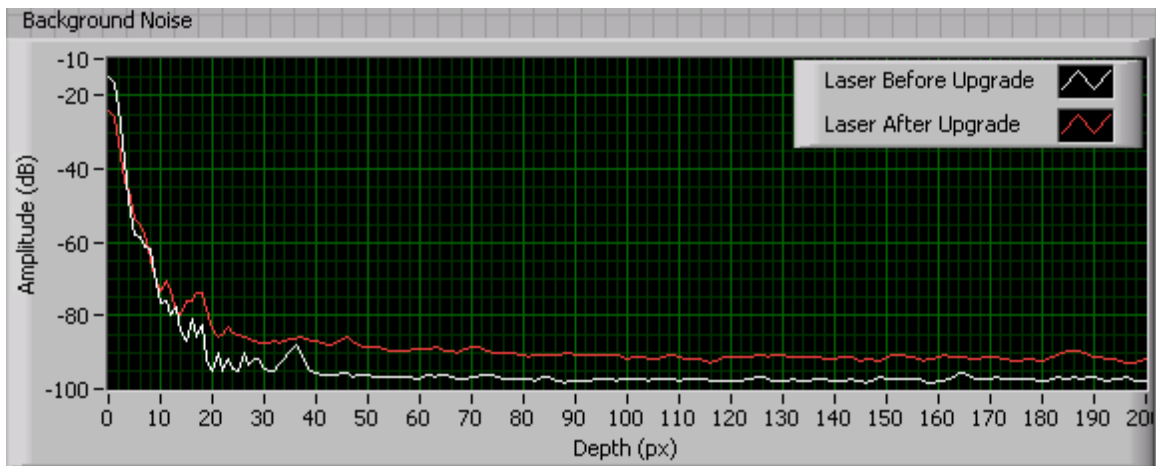


Figure D.1: Average background in the laser before the upgrade and after the upgrade. The laser upgrade has an average 6dB more noise that the laser before the upgrade at the same reference power.

The upgraded laser has about 5.2dB more noise (figure D.1), and about 10dB less in PSNR (figure D.2).

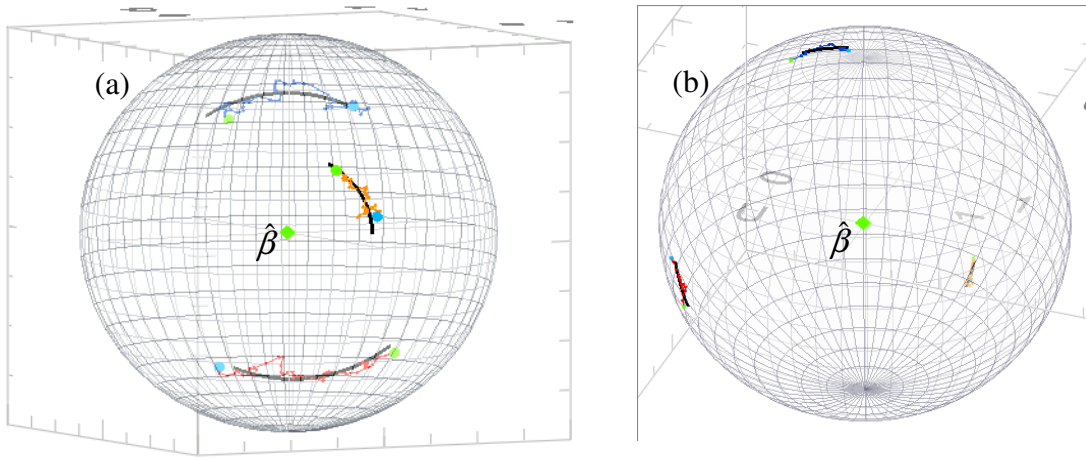


Figure D.2: Arcs and fits recorded from the left eye (OS) of a healthy patient. (a) Thick cluster from inferior quadrant. 100 A-scans per cluster, PSNR = 22.12 dB. (b) Thin cluster from nasal quadrant. 100 A-scans per cluster, PSNR = 12.76 dB. Using the laser prior to the upgrade on the same volunteer and at about the same location in the eye resulted in a 10 dB higher PSNR.

References

1. Huang, D., E.A. Swanson, and C.P. Lin, *JS Schuman, WG Stinson and W. Chang and MR Hee, T. Flotte and K. Gregory and CA Puliafito and JG Fujimoto,* "Optical coherence tomography," *Science*, 1991. **254**: p. 1178-1181.
2. Drexler, W., *Ultra-high-resolution optical coherence tomography.* *Journal of Biomedical Optics*, 2004. **9**: p. 47.
3. Cain, C.P. and A.J. Welch, *Measured and predicted laser-induced temperature rises in the rabbit fundus.* *Investigative Ophthalmology & Visual Science*, 1974. **13**(1): p. 60.
4. Welch, A.J., et al., *Experimental validation of thermal retinal models of damage from laser radiation.* 1979.
5. Brezinski, M.E., *Optical coherence tomography: principles and applications.* 2006: Academic Pr.
6. Sepideh, H., et al. *The broadest spectral bandwidth suitable for in-vivo UHROCT imaging of human and animal retina at 1060nm.* 2009: SPIE.
7. institute, A.N.S., *American National Standard for the Safe Use of Lasers ANSI Z136.1-2000.* 2000, New York: American National Standards Institute.
8. Povazay, B., et al., *Enhanced visualization of choroidal vessels using ultra-high resolution ophthalmic OCT at 1050 nm.* *Optics Express*, 2003. **11**(17): p. 1980-1986.
9. Unterhuber, A., et al., *In vivo retinal optical coherence tomography at 1040 nm-enhanced penetration into the choroid.* *Optics Express*, 2005. **13**(9): p. 3252-3258.
10. Bohren, C.F. and D.R. Huffman, *Absorption and scattering of light by small particles.* New York, 1983.
11. Fercher, A.F., et al., *Measurement of intraocular distances by backscattering spectral interferometry.* *Optics Communications*, 1995. **117**(1-2): p. 43-48.
12. Wojtkowski, M., et al., *Three-dimensional retinal imaging with high-speed ultra-high-resolution optical coherence tomography.* *Ophthalmology*, 2005. **112**(10): p. 1734-1746.
13. Chen, T.C., et al., *Spectral domain optical coherence tomography: ultra-high speed, ultra-high resolution ophthalmic imaging.* *Archives of Ophthalmology*, 2005. **123**(12): p. 1715.
14. Azzam, R.M.A. and N.M. Bashara, *Ellipsometry and Polarized Light.* 1977: North-Holland Publishing Company.
15. Saleh, B.E.A. and M.C. Teich, *Fundamental of Photonics.* Pure and Applied Optics, ed. i. John Wiley & Sons. 1991.

16. Yariv, A. and P. Yeh, *Optical Waves in Crystals*. Pure and Applied Optics. 2003: John Wiley and Sons, inc.
17. Kemp, N., *Enhanced Polarization-Sensitive Optical Coherence Tomography (EPS-OCT) for Characterization of Tissue Anisotropy*, in *Biomedical Engineering*. 2005, The University of Texas at Austin: Austin.
18. Choplin, N.T. and D.C. Lundy, *Atlas of glaucoma. 2*, illustrated ed. 2007: Informa Healthcare.
19. Huang, X.R. and R.W. Knighton, *Microtubules contribute to the birefringence of the retinal nerve fiber layer*. Investigative ophthalmology & visual science, 2005. **46**(12): p. 4588.
20. Zhou, Q. and R.W. Knighton, *Light scattering and form birefringence of parallel cylindrical arrays that represent cellular organelles of the retinal nerve fiber layer*. Applied optics, 1997. **36**(10): p. 2273-2285.
21. Fortune, B., G.A. Cull, and C.F. Burgoyne, *Relative course of retinal nerve fiber layer birefringence and thickness and retinal function changes after optic nerve transection*. Investigative Ophthalmology & Visual Science, 2008. **49**(10): p. 4444.
22. Häusler, G. and M.W. Lindner, *“Coherence Radar” and “Spectral Radar”—New Tools for Dermatological Diagnosis*. Journal of Biomedical Optics, 1998. **3**: p. 21.
23. Kemp, N., et al., *Form-biattenuance in fibrous tissues measured with polarization-sensitive optical coherence tomography (PS-OCT)*. Optics Express, 2005. **13**(12): p. 4611-4628.
24. Hee, M.R., et al., *Polarization-sensitive low-coherence reflectometer for birefringence characterization and ranging*. Journal of the Optical Society of America B, 1992. **9**(6): p. 903-908.
25. De Boer, J.F., et al., *Two-dimensional birefringence imaging in biological tissue by polarization-sensitive optical coherence tomography*. Optics Letters, 1997. **22**(12): p. 934-936.
26. Gordon, J.P. and H. Kogelnik, *PMD fundamentals: Polarization mode dispersion in optical fibers*. Proceedings of the National Academy of Sciences of the United States of America, 2000. **97**(9): p. 4541.
27. Saxer, C.E., et al., *High-speed fiber based polarization-sensitive optical coherence tomography of in vivo human skin*. Optics Letters, 2000. **25**(18): p. 1355-1357.
28. Roth, J.E., et al., *Simplified method for polarization-sensitive optical coherence tomography*. Optics Letters, 2001. **26**(14): p. 1069-1071.
29. Park, B.H., et al., *Jones matrix analysis for a polarization-sensitive optical coherence tomography system using fiber-optic components*. Optics letters, 2004. **29**(21): p. 2512.
30. Jiao, S., et al., *Optical-fiber-based Mueller optical coherence tomography*. Optics letters, 2003. **28**(14): p. 1206-1208.

31. Jiao, S., et al., *Fiber-based polarization-sensitive Mueller matrix optical coherence tomography with continuous source polarization modulation*. Applied optics, 2005. **44**(26): p. 5463-5467.
32. Yasuno, Y., et al., *Birefringence imaging of human skin by polarization-sensitive spectral interferometric optical coherence tomography*. Optics letters, 2002. **27**(20): p. 1803-1805.
33. Yasuno, Y., et al., *Polarization-sensitive complex Fourier domain optical coherence tomography for Jones matrix imaging of biological samples*. Applied Physics Letters, 2004. **85**: p. 3023.
34. Yamanari, M., et al., *Visualization of phase retardation of deep posterior eye by polarization-sensitive swept-source optical coherence tomography with 1- μ m probe*. Optics Express, 2009. **17**(15): p. 12385-12396.
35. Oh, W.Y., et al., *High-speed polarization sensitive optical frequency domain imaging with frequency multiplexing*. Optics express, 2008. **16**(2): p. 1096-1103.
36. Davé, D.P. and T.E. Milner, *Optical low-coherence reflectometer for differential phase measurement*. Optics Letters, 2000. **25**(4): p. 227-229.
37. Dave, D.P., et al., *Phase-sensitive frequency-multiplexed optical low-coherence reflectometry*. Optics Communications, 2001. **193**(1-6): p. 39-43.
38. Davé, D.P., T. Akkin, and T.E. Milner, *Polarization-maintaining fiber-based optical low-coherence reflectometer for characterization and ranging of birefringence*. Optics letters, 2003. **28**(19): p. 1775-1777.
39. Al-Qaisi, M.K. and T. Akkin, *Polarization-sensitive optical coherence tomography based on polarization-maintaining fibers and frequency multiplexing*. Optics Express, 2008. **16**(17): p. 13032-13041.
40. Wang, H., M.K. Al-Qaisi, and T. Akkin, *Polarization-maintaining fiber based polarization-sensitive optical coherence tomography in spectral domain*. Optics Letters, 2010. **35**(2): p. 154-156.
41. Ogden, T.E., *Nerve fiber layer of the primate retina: thickness and glial content*. Vision research, 1983. **23**(6): p. 581.
42. Cense, B., et al., *In vivo depth-resolved birefringence measurements of the human retinal nerve fiber layer by polarization-sensitive optical coherence tomography*. Optics letters, 2002. **27**(18): p. 1610-1612.
43. Pocock, G.M., et al., *The Relationship between Retinal Ganglion Cell Axon Constituents and Retinal Nerve Fiber Layer Birefringence in the Primate*. Investigative Ophthalmology & Visual Science, 2009.
44. Göttinger, E., et al., *Retinal nerve fiber layer birefringence evaluated with polarization sensitive spectral domain OCT and scanning laser polarimetry: A comparison*. Journal of Biophotonics, 2008. **1**(2).
45. Yamanari, M., et al., *Phase retardation measurement of retinal nerve fiber layer by polarization-sensitive spectral-domain optical coherence*

- tomography and scanning laser polarimetry*. Journal of biomedical optics, 2008. **13**: p. 014013.
46. Kemp, N., et al., *Depth-resolved optic axis orientation in multiple layered anisotropic tissues measured with enhanced polarization-sensitive optical coherence tomography (EPS-OCT)*. Optics Express, 2005. **13**(12): p. 4507-4518.
 47. Bouma, B.E. and G.J. Tearney, *Power-efficient nonreciprocal interferometer and linear-scanning fiber-optic catheter for optical coherence tomography*. Optics letters, 1999. **24**(8): p. 531-533.
 48. Sorin, W.V. and D.M. Baney, *A simple intensity noise reduction technique for optical low-coherence reflectometry*. IEEE Photonics Technology Letters, 1992. **4**(12): p. 1404-1406.
 49. Khosrofian, J.M. and B.A. Garetz, *Measurement of a Gaussian laser beam diameter through the direct inversion of knife-edge data*. Applied Optics, 1983. **22**(21): p. 3406-3410.
 50. Zhang, J., et al., *Full range polarization-sensitive Fourier domain optical coherence tomography*. Optics Express, 2004. **12**(24): p. 6033-6039.
 51. Chinn, S.R., E.A. Swanson, and J.G. Fujimoto, *Optical coherence tomography using a frequency-tunable optical source*. Optics letters, 1997. **22**(5): p. 340-342.
 52. Golubovic, B., et al., *Optical frequency-domain reflectometry using rapid wavelength tuning of a Cr⁴⁺: forsterite laser*. Optics letters, 1997. **22**(22): p. 1704-1706.
 53. Lexer, F., et al., *Wavelength-tuning interferometry of intraocular distances*. Applied Optics, 1997. **36**(25): p. 6548-6553.
 54. Haberland, U.H.P., V. Blazek, and H.J. Schmitt, *Chirp optical coherence tomography of layered scattering media*. Journal of Biomedical Optics, 1998. **3**(3): p. 259-266.
 55. Santhanam, K., *Clock System Design for quadrupling the frequency of Reference Clock for a Swept Source Spectral Domain Optical Coherence Tomography*. 2009, The University of Texas at Austin: Austin.
 56. Liou, H.L. and N.A. Brennan, *Anatomically accurate, finite model eye for optical modeling*. Journal of the Optical Society of America A, 1997. **14**(8): p. 1684-1695.
 57. Schmitt, J.M., S.H. Xiang, and K.M. Yung, *Speckle in optical coherence tomography*. Journal of Biomedical Optics, 1999. **4**: p. 95.
 58. Goodman, J.W., *Some fundamental properties of speckle*. Journal of the Optical Society of America, 1976. **66**(11): p. 1145-1150.
 59. Kemp, N.J., et al., *High-sensitivity determination of birefringence in turbid media with enhanced polarization-sensitive optical coherence tomography*. Journal of the Optical Society of America A, 2005. **22**(3): p. 552-560.

60. Brosseau, C., *Fundamentals of polarized light: A statistical optics approach*. 1998: John Wiley.
61. Goldstein, D.H. and E. Collett, *Polarized light*. 2003: CRC.
62. Park, J., *Polarimetric Analysis of Anisotropic Tissue using Polarization-Sensitive Optical Coherence Tomography (PS-OCT)* 2006, The University of Texas at Austin.
63. Press, W.H., et al., *Numerical recipes in C*. 1992: Cambridge Univ. Press Cambridge MA, USA:.
64. Park, B.H., et al., *In vivo burn depth determination by high-speed fiber-based polarization sensitive optical coherence tomography*. Journal of Biomedical Optics, 2001. **6**: p. 474.
65. Jiao, S. and L.V. Wang, *Jones-matrix imaging of biological tissues with quadruple-channel optical coherence tomography*. Journal of Biomedical Optics, 2002. **7**: p. 350.
66. Hitzenberger, C., et al., *Measurement and imaging of birefringence and optic axis orientation by phase resolved polarization sensitive optical coherence tomography*. Optics Express, 2001. **9**(13): p. 780-790.

Vita

Badr Elmaanaoui was born in Casablanca, Morocco on September 15, 1980, as the second son of Amina Hassar and Taibi Elmaanaoui. After completing his high school degree at Groupe Scolaire D'anfa, Casablanca, Morocco, in 1998, he moved to the U.S., where he received the degrees of Bachelor of Engineering and Master of Engineering in electrical engineering from the City College of New York, New York, in 2003 and 2005 respectively. In August 2005 he joined the Ph.D. program in electrical engineering at the University of Texas at Austin. His research was focused on optical coherence tomography for noninvasive diagnosis of biological tissue under the supervision of Dr. Thomas E. Milner and H. Grady Rylander, III.

Permanent address: Residence ennajd Immeuble 9 Apartment 89

Casablanca, Maroc

This dissertation was typed by the author.